POTENTIAL ENERGY CURVES OF HALOGEN MOLECULE ION-PAIR STATES

By

Philip John Wilson

DOCTOR OF PHILOSOPHY

EDINBURGH UNIVERSITY

1994

Declaration

I hereby declare that this thesis has been composed by myself, and except where due acknowledgement is given, the work described in it is my own and was carried out at the Universtiy of Edinburgh.

Acknowledgements

After four years studying at Edinburgh there are many people I would like to acknowledge. My greatest debt is, of course, to my two supervisors Dr K. P. Lawley, and Prof. Robert Donovan for their guidance and support over the years. I would also like to single out for special thanks Dr Trevor Ridley who not only produced all the excellent experimental work contained in this thesis but also provided many useful suggestions. Through my many discussions with K.P.L and T.R their skills in analysing and explaining complex problems, particularly in simple terms, has been of great value to me. Finally, I am grateful to the Science and Engineering Research Council for a postgraduate research studentship.

I would like to thank my parents, Janice and Michael, who throughout my education have provided a great deal enthusiastic encouragement and helpful advice, not forgetting the extra funding when the coffers were empty. To them I am most grateful.

Edinburgh has, and will continue to hold, a lot of very special memories for me. In particular, a very special mention goes to Fiona, thankyou for everything, particularly when I needed encouragement and a soothing drink.

Thanks also to Colin and Debbie for being great flatmates and to Anna, Sharon and Joni for being great workmates at Bookworld. Special thanks to the Bank of Danks for assisting and participating in many memorable sessions. Finally, I would like to thank the other research students, past and present in the laser group for their friendliness over the years and for providing such a stimulating drinking enviroment.

Abstract

The double resonance ionisation nozzle cooled spectroscopy (DRINCS) technique has been used to extend the existing vibrational constants for the lowest three ion-pair states of I_2 with 0_g^+ symmetry using the B state as the first resonant intermediate. The $E(^3P_2)$, $f(^3P_0)$ and $f'(^1D_2)$ states now cover the range v'=0–422, v'=0–228 and v'=0–166 respectively.

Potential energy curves beyond the previously existing RKR potentials have been generated using only the vibrational Dunham coefficients and the known asymptotic behaviour of the Coulombic branch of the potentials. These potentials have been used to simulate the DRINCS spectra and correctly reproduce the observed intensity minima in the envelope of the vibrational progression below 56000 cm^{-1}. Above this the band intensities are very irregular because of homogeneous interactions with Rydberg states.

The lifetime of the $f'(v'=0)$ state has been determined as 142± 6 ns. The reason for this unusually long lifetime is discussed in terms of the electronic structure of the $I^+(^1D_2)$ cation and the $B(^3\Pi_u\ 0_u^+)$ state. The electronic transition dipole moment function, $\mu_{f'\rightarrow B}(R)$, over the range 3.51–4.23 Å has also been determined by simulation of the dispersed fluorescence from the v'=11 level of the $f'(0_g^+)$ ion-pair state and shows a maximum at 4.05 Å.

A detailed investigation of the vibronic coupling between the $D'0_g^+$ ion-pair state and the $[^2\Pi_{3/2}]5d$: $2g$ Rydberg state of I_2 is carried out using jet-cooled REMPI linear time-of-flight techniques. Numerical modelling techniques correctly simulate the observed spectrum. The magnitude of H_{12}^{el} is calculated to be 450±100 cm^{-1} and is discussed in terms of the electronic configurations of the two interacting states.

Using the DRINCS technique, the observation of a new ion-pair state of ICl, the $f\,'0^+(^1D_2)$ state accessed via the $B0^+$ intermediate state is reported. Dunham coefficients valid up to v'=28 have been determined. In addition, the three lowest Ω=1 ion-pair states of ICl have been characterised in one series of DRINCS experiments via the $A1$ intermediate state. We report here the first observation of the third tier state, labelled $H'1(^1D_2)$ and present vibrational constants valid up to v'=18. Additionally, existing vibrational constants for the $G1(^3P_1)$ and $\beta 1(^3P_2)$ states have been extended to cover the range v'=0–63 and v'=0–137 respectively.

The potential energy surfaces of the T-shaped (C_{2v}) H_2...HF dimer, accessible in spin-allowed, vertical one and two-photon electronic transitions in the region above the global $^1A_1$ ground state minimum are explored using *ab initio* calculations. In particular, the low lying $^1B_1$, $^1B_2$ and $^1A_1$ Rydberg states and their corresponding cationic core states are investigated. In addition, a search for the T-shaped $^1A_1$ H_3^+...F^- ion-pair state(s) is carried out.

Contents

List of Tables

List of Figures

Glossary

T_e	Electronic term value
R_e	Equilibrium bond distance
D_e	Dissociation energy
B_v	Rotational constant
ω_e	Equilibrium vibrational frequency
$V(R)$	Potential energy as a funtion of bond length
e	Electronic charge
Z	Nuclear charge
C_n	Coefficients of the long-range multipole expansion terms
g, u	Gerade and ungerade symmetry for homonuclear molecules corresponding to molecule-fixed inversion of the coordinates of all electrons and nuclei through the centre of mass
l_i	Orbital angular momentum quantum number of electron i
s_i	Spin angular momentum quantum number of electron i
L	Total electronic orbital angular momentum
S	Total electron spin angular momentum
λ_i	Resultant orbital angular momentum of electron i about the internuclear axis
Λ	Total orbital angular momentum about the internuclear axis
Σ	Total spin angular momentum about the internuclear axis
Ω	Total electronic angular momentum
$\|\|...l_s m_s...\|\|$	Russell-Saunders microstate
δ	Quantum defect

Chapter 1

Introduction

Spectroscopy in the ultra-violet (UV) and vacuum-UV (VUV) regions are characterised by a high density of vibronic states. Special techniques are needed to unravel the extensive perturbations and to establish the potential energy curves in one of two descriptions, the diabatic or adiabatic basis. In this thesis, accurate diatomic halogen molecule potential curves are generated using data obtained in multiphoton spectroscopic studies of several ion-pair states of I_2 and these potentials are then used as a basis to discuss the perturbations observed in the spectra resulting from homogeneous interactions between Rydberg and ion-pair states. A detailed theoretical study of the vibronic coupling between an ion-pair and Rydberg state of I_2 is carried out, requiring the calculation of accurate potential energy curves in order to correctly simulate the observed spectrum. Adiabatic potential curves for the ground, Rydberg and ion-pair states of the H_2...HF cluster are calculated using *ab initio* methods providing several examples of strongly avoided crossings between states of the same symmetry.

In the following sections the characteristics and properties of halogen molecule ion-pair states are introduced and discussed in terms of their electronic configurations. Since Rydberg/ion-pair state interactions are an important part of this thesis, the nature of the former states are examined in detail before a theoretical discussion of their interaction with ion-pair states is given.

1.1 The Ion-Pair States

Although all molecules possess ion-pair states, the extent of their spectroscopic observation varies widely from molecule to molecule. In particular, the ion-pair states of polyatomic molecules (excluding cases where they constitute the ground electronic state) have largely eluded detection because of the high density of states accessed, typically via visible/VUV, one or two-photon vertical excitation allows very rapid internal conversion. In the vast majority of cases, the T_e values of the ion-pair states of molecules lie close to the lowest Rydberg states (although their R_e values differ significantly). In a few cases they represent the ground electronic state, e.g earth alkali group IIA halides, 1:1 adducts etc [1].

It was the development of multiphoton spectroscopic techniques which aided the study of ion-pair states by overcoming the restrictive one-photon selection rules and limited Franck-Condon (FC) windows associated with single-photon studies. Although only a very small proportion of the total number of diatomic ion-pair states have been observed, a few of these with suitable resonant intermediate states (with large R_e values) have been studied extensively, e.g group IIIA halides, halogens and interhalogens [2]. The ion-pair states of the latter two examples are probably the most studied and best understood of all molecules.

The simplest definition of an ion-pair state of a neutral diatomic molecule is one in which diabatic dissociation produces a pair of oppositely charged ions where the asymptotic form of the potential energy curve $V(R)$ is Coulombic (e^2/R). However, crossings of the asymptotic branches of the ion-pair and Rydberg states occur at large R and if these states are of the same symmetry, the adiabatic dissociation products of the ion-pair state no longer correlates with $A^+ + B^-$ but instead with $A + B^*$ where B^* is an excited neutral atom.

A consequence of this asymptotic behaviour and the large R_e values associated with ion-pair states are their unusual spectroscopic characteristics. These states

can support a high density of vibrational levels, have large dissociation energies and small B_v and ω_e values compared with conventional valence states. Although these characteristics make the observation and analysis of ion-pair states difficult, a variety of spectroscopic techniques have been employed in their search, with varying degrees of success, as discussed in section 1.4.

The search for ion-pair states is not restricted to experimental methods. The continuing development of more efficient computational techniques has greatly increased our knowledge of molecular electronic states using *ab initio* methods. However, the identification of ion-pair states using this method is not straightforward and cannot really be done by a calculation at a single R value. Self-consistent field (SCF) calculations at a single geometry, usually around $R_e^{i\text{-}p}$, would need to distinguish the prescence of strongly antibonding molecular orbitals (MOs) and some diffuse character associated with the anion. However, at the configuration interaction (CI) level, the prescence of more than one dominant MO configuration may confuse unambiguous assignment as was found in our search for ion-pair states in the H_2...HF complex discussed in chapter 6. Alternatively, large and expensive geometry scans could be carried out in order to identify the characteristic long range $1/R$ Coulomb potential but would require a large symmetry adapted function (SAF) configuration basis. Dipole moment calculations do not provide an unambiguous identification of an ion-pair state because many molecules with a centre of symmetry and which cannot therefore have a permanent dipole are rich in ion-pair states.

Since ion-pair states correlate with the atomic ions A^+B^-, their outer branches are essentially Coulombic and can be modelled at large R using an expansion of long range multipole interaction terms. The truncated Rittner potentials [3] of the form in equation 1.1 are the leading terms required to model the interaction in the halogens between a closed shell anion (X^- p^6) and open shell cation (X^+ p^4),

$$V(R) = T_\infty - C_1/R \pm C_3/R^3 - C_4/R^4 - C_6/R^6 \qquad (1.1)$$

where R is the interionic distance, T_∞ is the ion-pair dissociation limit, the C_1, C_3, C_4 and C_6 coefficients correspond to the charge-charge, charge-quadrupole, charge-polarisation and induced dipole-induced dipole interactions (dispersion forces) respectively. The C_1, C_4 and C_6 terms always provide attractive energy contributions to $V(R)$ but the sign of the C_3 coefficient depends on the electronic configuration of the quadrupole ion and is non-zero when J_+ or $J_- \geq 1$ and is generally negative when p_π occupancy is greater than p_σ in the p^4 microstate of the positive ion of the halogen ion-pair states. It is this interaction term and to a lesser extent the other higher order terms that are responsible for mixing J-states from different clusters as discussed in more detail in section 1.1.4. Although the asymptotic form of $V(R)$ is dominated by the C_1 term, in order to reproduce the observed ion-pair potentials it is necessary to include these higher-order multipole terms. Because the various C_n term values are known fairly accurately for the halogens and interhalogens, several examples exist where the outer branches have been successfully modelled, including work in chapters 3 and 5 of this thesis. The modelling of the outer branches at larger R assumes that overlap and consequent exchange effects are negligible. Tellinghuisen added an empirical exponential repulsion term, $Aexp(-\alpha R)$, to equation 1.1 allowing the form of the inner branch of the $D(0_u^+)$ ion-pair state potential to be estimated as well [4].

1.1.1 The Halogen and Interhalogen Ion-Pair States

Of all the halogen and interhalogen molecules, I_2 and ICl respectively, have been the most intensively studied [2, 5]. In both types of molecule there are 20 ion-pair and 23 valence states, where the former lie above the latter in energy. The lowest lying Rydberg states and the ion-pair states have similar T_e values and do cross one another at both large and small R.

The ion-pair diabatic dissociation products correlate with a closed shell ($^1S_0$) anion and with one or other of the positive cation states ($^3P_2$, $^3P_1$, $^3P_0$, $^1D_2$ and $^1S_0$). Since the halogen cation has several spectroscopic states, the potentials correlating with each ionic asymptote will run parallel to one another giving rise to clusters (or tiers) of ion-pair states and only the inner branches will differ significantly at small R as their differing MO configurations dominate. In I_2 and Br_2, because of the strong spin-orbit coupling in the cation, there is clear clustering of the T_e values at R_e into three groups with spacings similar to those between the corresponding cationic states. The two fourth tier ion-pair states correlating with the ($^1S_0$) cation state, having g or u symmetry, have not yet been observed. In contrast, for the gerade Cl_2 ion-pair states the T_e values at R_e only loosely follow the pattern of the cationic states because of the less strong spin-orbit coupling associated with Cl^+ [6].

Although the g/u parity symmetry is missing for the interhalogens there are still 20 ion-pair states because dissociation limits occur for X^-+Y^+ (10 states) as well as X^++Y^- (10 states) and similar clustering around the two possible asymptotes will occur. The lowest energy asymptotes will be those where the anion is the atom associated with the largest electron affinity. In ICl, the ionic asymptotes correlating with I^++Cl^- and I^-+Cl^+ are widely separated in energy by $\geq$ 20,000 cm^{-1} and as a consequence at $R \leq R_e$, overlap of the states correlating with the I^+ ($^1D_2$) cluster and with the Cl^+ ($^3P_2$) cluster occurs and mixing takes place if they have the same Ω-value [5].

1.1.2 The Ion-Pair States of I_2

13 of the 20 theoretically possible ion-pair states of I_2 have so far been observed and are shown in table 1.1. All have large R_e values ($\geq$3.5 Å) but are deeply bound ($\sim$ 30,000 cm^{-1}) as a result of their shallow Coulombic outer branches. Energetically, the third and fourth tier ion-pair states are experimentally difficult to access which reflects the small number of such states observed compared to

those in the first and second tiers. The first observation of a third-tier gerade ion-pair state around T_e is presented in chapter 2 of this thesis.

In the next section, the stacking of the ion-pair state clusters and the detailed energy ordering of members within a common cluster are discussed in terms of their electronic structure. Bearing in mind the large radial separations associated with the medium to high vibrational levels of the ion-pair states accessed in this thesis, their electronic structure can best be described using two complementary models, where the single MO description and the separated ion $(J_A M_A J_B M_B)$ schemes are appropriate at small and large $R(\geq R_e)$ respectively. Although the separated ion-model provides a good description of the ion-pair electronic states even down to R_e^{ip}, as R decreases further, exchange terms begin to dominate and a single MO description becomes rapidly more appropriate.

1.1.3 The Molecular Orbital Bonding Description

A total of ten valence electrons, five each from the two neutral p^5 iodine atoms can be distributed amongst the Mulliken MO configuration $\sigma_g^l \pi_u^m \pi_g^n \sigma_u^p$ or more succinctly [lmnp]. The σ and π MOs are formed from a linear combination of 5p-atomic orbitals, $[5p_\sigma^A \pm 5p_\sigma^B]$ and $[5p_\pi^A \pm 5p_\pi^B]$ respectively, where the σ_g and π_u MOs on the nuclear centres A and B are formed by in-phase bonding represented by the + sign. The g/u symmetry condition is absent in the heteronuclear halogens and because the atomic orbitals from each centre are no longer degenerate, they will contribute unequally to the MO.

State	T_e/cm^{-1}	ω_e/cm^{-1}	$R_e/\text{Å}$	Diss. Limits	Refs.
third cluster					
$F'0_u^+$	51706.2	131.0	3.48	$^1D_2+^1S_0$	[7, 8]
$f'0_g^+$	55409.6	97.0	3.825	$^1D_2+^1S_0$	[9, 10, 11]
second cluster					
$H1_u$	48280.3	107.7	3.63	$^3P_1+^1S_0$	[12]
$G1_g$	47559.1	106.6	3.53	$^3P_1+^1S_0$	[13]
$F0_u^+$	47217.4	96.3	3.60	$^3P_0+^1S_0$	[14]
$g0_g^-$	(47070)	(105.7)	(3.55)	$^3P_1+^1S_0$	[15]
$f0_g^+$	47025.9	104.2	3.57	$^3P_0+^1S_0$	[16, 9]
first cluster					
$\delta 2_u$	41689	100.2	(4.0)	$^3P_2+^1S_0$	[15, 17, 18]
$\gamma 1_u$	41621.3	95.0	3.67	$^3P_2+^1S_0$	[18]
$E0_g^+$	41411.8	101.4	3.65	$^3P_2+^1S_0$	[19, 11]
$D0_u^+$	41028.6	95.0	3.58	$^3P_2+^1S_0$	[20]
$\beta 1_g$	40821.0	105.0	3.61	$^3P_2+^1S_0$	[21]
$D'2_g$	40388.3	104.0	3.60	$^3P_2+^1S_0$	[22, 23]

Table 1.1. Principal spectroscopic constants for the ion-pair states of I_2.

A list of the single MO configurations for the 20 ion-pair states first derived by Mulliken [24] and later revised are shown in table 1.2, together with the Hund's case (a) and (c) assignments and their diabatic dissociation products. In the absence of any interactions, the relative energy ordering adopted by these MO ion-pair states as a function of R is determined by their spin state (singlet or triplet) and by the play off between their bonding and anti-bonding orbital occupancies. At large R, the $\sigma_{g,u}$ and $\pi_{g,u}$ MO pairs are degenerate but as R decreases and the overlap between the p_π atomic-orbitals on the two atoms increases, the energy of the p_{π_u} and p_{π_g} orbitals are lowered and raised respectively. The gerade p_σ MO falls and then rises in energy as the p_σ overlap on the two atoms passes through a maximum.

However, as R decreases and the energy separation between these states decreases, avoided crossings between states of the same symmetry can occur, where the description of the state as a single dominant MO is no longer valid but instead becomes an admixture of MO configurations. A detailed discussion on the types and strength of the various interactions between states is given in section 1.3.

MO Configuration $[\sigma_g^l \pi_u^m \pi_g^n \sigma_u^p]$	case (a)	case (c)	Correlation	JJ	Dissociation Products
0442	$^1\Sigma_g^+$	0_g^+		0_g^+	$I^+(^1S_0)+I^-(^1S_0)$
				0_u^+	
1342	$^1\Pi_u$	1_u		2_g	$I^+(^1D_2)+I^-(^1S_0)$
	$^3\Pi_u$	0_u^+		2_u	
		0_u^-		1_g	
		1_u		1_u	
		2_u		$0_g^+(f')$	
				$0_u^+(F')$	
2242	$^1\Sigma_g^+$	0_g^+		$0_g^-(g)$	$I^+(^3P_{1,0})+I^-(^1S_0)$
	$^1\Delta_g$	2_g		0_u^-	
	$^3\Sigma_g^-$	0_g^+		$1_g(G)$	
		1_g		$1_u(H)$	
				$0_g^+(f)$	
				$0_u^+(F)$	
1432	$^1\Pi_g$	1_g		$2_g(D')$	$I^+(^3P_2)+I^-(^1S_0)$
	$^3\Pi_g$	0_g^+		$2_u(\delta)$	
		0_g^-		$1_g(\beta)$	
		1_g		$1_u(\gamma)$	
		2_g		$0_g^+(E)$	
				$0_u^+(D)$	
2332	$^1\Sigma_u^+$	0_u^+		1_u	$I(^2P_{1/2})+I(^2P_{1/2})$
	$^1\Delta_u$	2_u		0_u^-	
	$^3\Sigma_u^-$	0_u^+		0_g^+	
		1_u			
	$^3\Sigma_u^+$	0_u^-		2_g	$I(^2P_{3/2})+I(^2P_{1/2})$
		1_u		$2_u(b')$	
	$^3\Delta_u$	1_u		1_g	
		2_u		$1_g(c)$	
		3_u		1_u	
	$^1\Sigma_u^-$	0_u^-		1_u	
				0_g^-	
				0_u^-	
				0_g^+	
				$0_u^+(B)$	
1441	$^1\Sigma_u^+$	0_u^+		3_u	$I(^2P_{3/2})+I(^2P_{3/2})$
	$^3\Sigma_u^+$	0_u^-		$2_u(A')$	
		1_u		$1_u(B'')$	
				$1_u(A)$	
2422	$^1\Sigma_g^+$	0_g^+		2_g	
	$^1\Delta_g$	2_g		$1_g(a)$	
	$^3\Sigma_g^-$	0_g^+		0_u^-	
		1_g		$0_u^-(B')$	
				$0_g^+(a')$	
2341	$^1\Pi_g$	1_g		$0_g^+(X)$	
	$^3\Pi_g$	0_g^+			
		0_g^-			
		1_g			
		2_g			
2431	$^1\Pi_u$	1_u			
	$^3\Pi_u$	0_u^+			
		0_u^-			
		1_u			
		2_u			
2140	$^1\Sigma_g^+$	0_g^+			

Table 1.2. Adiabatic Correlation Scheme for the States of I_2.

The very limited number of vertical i.p⟵X transitions seen in the homonuclear halogens have been explained in terms of a single or combination of Mulliken MO configurations, the latter a result of spin-orbit coupling or electron correlation. For example, a single MO description provides the explanation as to why, in single photon-transitions from the ground state of the homonuclear halogens only one ion-pair state is observed, the $D^1\Sigma_u^+$ [1441] state, which is the only MO configuration that can be accessed in a one-electron dipole allowed transition from the $X^1\Sigma_g^+$[2440] ground state [25].

However, the inability of the Mulliken MO description to adequately explain the observed fluorescence from ion-pair states at $R \geq R_e$ and indeed the clustering pattern of the ion-pair states whose spacings are similar to those of the separated ions means a more suitable description at $R \geq R_e$ is required.

1.1.4 The Separated-Ion Model

The most appropriate description of the electronic structure of the ion-pair states of I_2 at $R \geq R_e^{i\text{-}p}$ is the separated ion or $(J_A M_A J_B M_B)$ scheme. In this model, separate, strong spin-orbit coupling at each centre is assumed where coupling between L_i and S_i, the orbital and spin angular momentum respectively of electron i is strong relative to coupling between L_i and the internuclear axis. Only as a final step are the two ionic centre configurations coupled to give the diatomic wavefunctions of the form:

$$|\Omega\rangle_{u,g}^{+/-} = (1/\sqrt{2})N.A\left\{|JM\rangle_A|00\rangle_B \pm |00\rangle_A|JM\rangle_B\right\}, \qquad (1.2)$$

where A is the partial antisymmetriser for electron exchange between the two centres, N is the normalisation coefficient, the u/g subscript represents the parity of the state arising from inversion of space coordinates through the centre of symmetry of the molecule where gerade states are given by a + sign. The $+/-$ superscript is the parity defined for Ω=0 states representing reflection of the space-spin coordinates through the nuclear plane.

At zeroth order, the ionic configurations in equation 1.2 are best described using the pure Russell-Saunders (RS) basis [26]. In RS coupling, Coulomb interaction between electrons is strong, the orbital angular momentum and the electron spins couple separately to form the resultant L and S respectively. The weak spin-orbit operator then couples L and S to give the total angular momentum J=L+S. The relative energy ordering of the pure RS states, designated by $^{2S+1}L_J$, is dominated by the inter-electron repulsion terms. As a result, the singlet and triplet states separate in energy, the former lying higher in energy so that in order of increasing energy the p^4 I^+ states are ^3P_J, $^1D_2$ and $^1S_0$.

However, the RS scheme has so far neglected spin-orbit coupling at the cationic centre. Diagonal elements of the spin-orbit operator, H_{SO}, lift the J degeneracy of a multiplet but because the RS state still dominates the configuration the energy ordering is still dominated by the 2S+1 inter-electron repulsion term. The off-diagonal elements of the spin-orbit operator mix RS states with different L and S but the same J value (j-j coupling) where the anomalous energy ordering of the $^3P_0$ and $^3P_1$ states of I^+ arises due to $^3P_2 - ^1D_2$ and $^3P_0 - ^1S_0$ mixing.

The degree of spin-orbit coupling between two configurations is a sum of the spin-orbit interactions between the one-electron spin-orbitals of the particular p^4 microstate of I^+. For example, the strength of the interaction coupling the $^3P_2$ and $^1D_2$ configurations, $\langle||1^+1^-0^+\underline{1}^+||\,|H_{SO}|\,||1^+1^-0^+0^-||\rangle$, is $1/\sqrt{2}\zeta_{5p}$ with the ladder operator l_-s_+ acting on the $||0^-||$ orbital, where $\zeta_{5p} = \langle 5p|\Im(r)|5p\rangle$ is the effective one-electron spin-orbit coupling constant for an electron in a $5p$ orbital [27]. In order of increasing energy, the five RS I^+ cation states are $^3P_2$, $^3P_0$, $^3P_1$, $^1D_2$ and $^1S_0$ and in the separated ion-model it is these states which predominantly determine the ordering of the ion-pair clusters.

The splitting of states within a cluster is the result of intramolecular coupling. The separated ion-model treats the coupling of the two centres separately where the electrostatic field is assumed to be spherically symmetric and the three p-orbitals remain degenerate, but as the two centres approach one another a cylin-

drical field symmetry forms and this degeneracy is lifted. Since the ion-pair states are strongly bound and because the separated ion-model is valid for $R \geq R_e$, there must be some long range centre-centre interaction well beyond where orbital overlap is significant. Although Coulomb attraction between the oppositely charged ions provides most of the bonding strength ($\geq$95%) in ion-pair states it does not mix RS configurations at the cationic centre unlike the interaction between the anionic field gradient and the cationic quadrupole. This effect is dependent on the axial component of J, M_J, and is responsible for separating the different Ω components of a particular ion-pair cluster associated with a common I^+ configuration.

The charge-quadrupole interaction can couple RS states of the same M_J and spin multiplicity where the matrix elements are given by [28]

$$\langle JM|\frac{1}{2}\Theta_{zz}F'_{zz}|JM\rangle = \frac{e^2\langle\rho^2\rangle_+}{4\pi\epsilon_0 r_{AB}^3}\langle {}^{2S+1}L_{J_1M}|\sum P_{20}(\theta_i)|{}^{2S+1}L_{J_2M}\rangle, \qquad (1.3)$$

where r_{AB} is the interionic separation between charge-centres treated as point charges, F'_{zz} the field gradient, $\langle\rho^2\rangle_+$ is the mean square electron radius of a cationic valence orbital and P_{20} is the Legendre polynomial $(3\cos^2\theta - 1)$. Like the spin-orbit coupling discussed earlier, the degree of charge-quadrupole interaction depends on the particular p^4 I^+ microstate under consideration. Diagonal matrix elements are different for different M_J states and the off-diagonal elements arise when a microstate is common to more than one RS configuration. The contribution of each p_π and p_σ electron to the angular integrals are $\langle Y_{11}|P_{20}(\theta)|Y_{11}\rangle = -1/5$ and $\langle Y_{10}|P_{20}(\theta)|Y_{10}\rangle = 2/5$ respectively [27]. For example, the diagonal matrix element for the ${}^3P_{22}$ Russell-Saunders configuration, $||1^+1^-0^+\underline{1}^+||$, is $-1/5$ Q where $Q = e^2\langle\rho^2\rangle_+/4\pi\epsilon_0 r_{AB}^3$.

The charge-quadrupole interaction favours p_π occupancy over p_σ though this stabilisation will be balanced by the increased inter-electron repulsion in some microstates with low p_σ occupancy, for example $||1^+1^-\underline{1}^+\underline{1}^-||$.

Finally, the u/g states of an Ω-pair within the same cluster are split, one up and one down from the Ω-dependent energy as a result of the electron exchange integral whose strength and sign depends on the particular ion-pair configuration [10]. At

$R \leq R_e^{i,p}$ each u/g pair is associated with a different single MO configuration which explains their different R_e values.

1.2 The Rydberg States

From previous studies [2 and references therein] and from the work presented in this thesis, it has been shown that OODR techniques give ready access to the manifold of ion-pair states of the halogens and interhalogens where the resonant intermediates are the B or A states that have large R_e values. DRINCS studies have so far failed to observe any Rydberg states directly and the reason for this still remains a mystery. Observation of the Rydberg states is only possible indirectly when they mix with the ion-pair states producing perturbations in the observed spectra, i.e irregular band intensities and displacements in term values, etc. Therefore, although we do not directly observe Rydberg states, their prescence has important implications on the observed DRINCS spectra. A possible explanation may be the fact that the ionisation step is more efficient from an ion-pair state. In chapter 5, vibronic coupling between a Rydberg and ion-pair state is investigated using jet-cooled REMPI techniques where in contrast to DRINCS, the Rydberg states of I_2 dominate the spectrum and the ion-pair systems are weak.

For these reasons, a discussion on the theoretical aspects and the spectroscopic observation of Rydberg states now follows, paying particular attention to examples of Rydberg/ion-pair mixing.

Atomic Rydberg states provide a good basis for discussing the behaviour of molecular Rydberg states fixed at any one nuclear configuration [29, 30]. Such states involve the promotion of an electron, usually of non-bonding or weakly antibonding/bonding character in molecular systems, to orbitals of higher principal quantum number, n. Excitation of the electron to progressively larger n constitutes a Rydberg series and as $n \rightarrow \infty$ the series converges to the limit of the atomic/molecular ion core, corresponding to the complete removal of the Rydberg

electron. The radial expectation value of a Rydberg orbital is generally much greater than the internuclear distance of the molecular core and therefore, to a first approximation, the Rydberg electron experiences an isotropic Coulomb attraction and is largely unaffected by the rotational and vibrational motion of the molecular ion core. A brief discussion on the nature of atomic Rydberg states now follows to provide a basis for considering the more complex molecular Rydberg systems.

1.2.1 Atomic Rydberg States

Some of the earliest spectroscopic studies were concerned with the the H-atom which is the simplest Rydberg system of all, consisting of a single electron and proton. Initial studies by Paschen [31], Lymman [32] and later confirmed by Bracket [33] and Pfund [34] showed that the position of a series of convergent spectral lines could be represented by mathematical expressions. In reality, these expressions are only specific examples of a more general formula of the form in equation 1.4 applicable to multi-electron systems derived by Rydberg some 20 years earlier whilst characterising the spectral lines of alkali metal atoms [35].

The diffuse nature of Rydberg electrons means we can expect the spectra of multi-electron atoms to resemble the spectrum of atomic hydrogen but deviations from H-atom behaviour in all multi-electron atoms arise because of the presence of electrons associated with the core and the higher nuclear charge. Atomic Rydberg series can be described using the H-atom formula where a correction term δ is added:

$$E_{nl} = IP[core^{+}] - R/[n - \delta(l)]^2 \tag{1.4}$$

where $IP[core^{+}]$ is the energy of the ion core which the Rydberg series converges to, n is the principal quantum number of the Rydberg electron, R is the Rydberg constant (109737.1 cm^{-1}) and δ is the quantum defect associated with a particular Rydberg electron.

The latter is required because the presence of core electrons means the Rydberg electron experiences a shielded Coulomb potential that falls off more rapidly with distance than the pure Coulomb potential, therefore the energy of the Rydberg electron is not independent of l, the angular momentum quantum number. Because the nl_{Ryd} radial wavefunctions penetrate into the core region, n in the H-atom expression now becomes a non-integer effective quantum number, $(n - \delta)$, where the magnitude of the correction factor δ is mainly dependent on how penetrative the Rydberg electron is as a function of nl. For a given n, δ for different l values increases in the order s>p>d>f where s-orbital radial wavefunctions have a non-zero amplitude at the nucleus and therefore penetrate more into the core than the other orbitals which have nodes there. The centrifugal effect associated with electrons which have $l > 0$ also increases in the order given, resulting in less penetration.

The amount of penetration is not only determined by the properties of the Rydberg electron but also by those of the core, namely the orbital symmetries contained within the core. A core which contains occupied (real precursor) or unoccupied (virtual precursor) orbitals of the same symmetry as the Rydberg orbital results in a much more effectively penetrating Rydberg electron. In general δ is relatively large and positive for all Rydberg atomic orbitals which have precursors in the core where $\delta_{real\,prec} > \delta_{vir\,prec}$. For example, the Rydberg states of atomic iodine, with configurations of the form $(5s^25p^4)_c nl$ have δ values of $\sim$ 4.1, 3.6 and 2.5 for 6s(l=0), 6p(l=1) and 5d(l=2) respectively [36]. In comparison, in Cl where there is no precursor for the 3d-orbital the corresponding δ values are 2.2, 1.8 and 0.5 for the 4s, 4p and 4d orbitals respectively.

The effects of spin correlation are also important in determining the magnitude of δ. For example, in even electron Rydberg states such as iodine, the Rydberg electron can be either spin parallel or antiparallel with respect to the unpaired electron in the core where the latter constitutes an overall singlet state (δ is negative) which is higher in energy than the triplet (δ is positive) state.

Finally, deviations from H-atom behaviour as a result of increasing Z, the nuclear charge, which produces a strong increase (as $\sim Z^4$) in spin-orbit coupling manifests itself as fine structure in the spectrum. As n increases, this non-degeneracy of terms arising from a particular configuration decreases due to decreased penetration and the spectrum becomes more H-atom like.

The coupling scheme used for I_2 to describe the coupling between the Rydberg electron and the molecular core is Hund's case (c) as a result of the separate strong spin-orbit coupling at each atom center. For this reason a brief discussion of the coupling scheme most appropriate for atomic iodine will follow. Minnhagen [37] and Racah [38] have suggested that the Rydberg states of atomic iodine are best described in $J_c l$ coupling where the total angular momentum of the I^+ ion core, J_c, is coupled to the orbital angular momentum, l, of the Rydberg electron to give the resultant K. The spin of the Rydberg electron, S, is then coupled to K to give the total angular momentum, J, and the states are then labelled, for example, $(^3P_J)_c nl[K]_J$. One of the premises of $J_c l$ coupling is that the splitting caused by the spin of the Rydberg electron for a given value of K is small with respect to the splitting between different K values.

1.2.2 Molecular Rydberg States

The same general principles discussed for atomic Rydberg states also apply to molecular systems. Equation 1.4 is valid for molecules whose nuclear coordinates are fixed at any one configuration where $IP[core^+]$ now represents the energy of the molecular ion core which the Rydberg series converges to. It has been shown for many molecules, that δ is generally very similar in a molecular core as when associated with an atomic one, unless there are specific perturbations of the Rydberg state.

For low n, molecular Rydberg orbitals retain the symmetry properties of those in the core. For example, in diatomic molecules, the Hund's case (a) coupling scheme can be used to characterise the Rydberg electron where only the total or-

bital angular momentum, L, and total spin angular momentum, S, are well defined along the internuclear axis with components Λ and Σ respectively. The total angular momentum is directed along the internuclear axis, $\Omega = \Lambda + \Sigma$. All $np(l = 1)$ Rydberg states are split into a doubly degenerate Π (λ=$\pm$1) component and a non-degenerate Σ component (λ=0) where the energy spacing for these increases in the order $\Delta n > \Delta l > \Delta\lambda$. Because the kinetic and potential energies of a Rydberg electron in low n levels is generally much greater than the vibrational and rotational energies of the nuclei, the Born-Oppenheimer (BO) approximation [39] is valid, the electron's momentum is coupled strongly to the internuclear axis and λ is a good quantum number. However, as n increases, the BO approximation breaks down as the l component of the Rydberg electron becomes less strongly coupled to the internuclear axis and the electron begins to experience an increasingly isotropic Coulomb attraction by the molecular core. Therefore the Rydberg electron becomes more H-atom like as the orbitals with different λ become strongly mixed.

An important new feature in molecular Rydberg systems is how these states behave as a function of their internuclear coordinates and in particular how the MOs and their energies vary with R in diatomic molecules. In chapter 6 the effect of varing several coordinates of the H_2...HF molecule in various Rydberg states is discussed.

The potential energy surfaces of Rydberg states determined from experiment are generally not well studied, many are thought to be predissociated, as is the case for the halogens. In general, around R_e^{Ryd}, the form of diatomic Rydberg state potential curves are similar to those of the ground X_2^+ state but the diabatic dissociation products of the former correlate with one ground state and one excited state atom. The asymptotic form of both these states are dominated by interatomic interactions whose leading term is the quadrupole-quadrupole interaction which has a $1/R^5$ dependence [40], in contrast to the shallow attractive branches resulting from the dominant long-range $1/R$ interactions characteristic of ion-pair states. The diffuse nature of Rydberg orbitals means they are essentially non-

bonding in character and therefore the form of the potential around R_e is largely determined by the bonding characteristics of the Rydberg electron's origin in the ground state configuration. In general, the lowest lying molecular Rydberg states are formed from the promotion of a non-bonding or weakly antibonding/bonding electron to orbitals of higher n resulting in potential energy curves very similar in form to those of the X_2^+ ground state and to a first approximation, as n increases, the molecular bond remains unchanged for any member of a particular Rydberg series.

In the independent particle approximation (IPA) an electronic state can be specified by a single electronic configuration where a simple SCF MO description is usually a good one at R_e. However, the definition of a valence or Rydberg state depending on the size of the excited orbital is not always unambiguous since in diatomic molecules the classification of an excited MO may change from valence $\leftrightarrow$ Rydberg with changing R. For example, in the $V\ ^1\Sigma_u^+$ $(1\sigma_g^1 1\sigma_u^1)$ state of H_2 the $1\sigma_u$ MO at large R transforms to $1s_A$–$1s_B$, as R$\rightarrow$0 it becomes $2p\sigma$ which is a true Rydberg orbital [30], a process called Rydbergisation [41]. The description of the lowest energy Rydberg states of many small molecules, e.g H_2O, CH_3OH, CH_3NH_2, NH_3, PH_3 and CH_4 provides difficulties since in each case, the lowest energy excited singlet state results from electron promotion to an orbital that is recognizably Rydberg at small R, but as these molecules distort along their respective dissociation coordinates the nature of these Rydberg orbitals changes, evolving smoothly into an antibonding valence orbital of the corresponding symmetry species [42].

In Rydberg states of even-electron diatomic molecules, the ion core is usually in a doublet spin state resulting in two Rydberg series, one triplet and the other singlet as is the case for the Rydberg states of I_2 with Λ_c=1. At $R \leq R_e$, the even electron Rydberg wavefunction, $\Psi_{Tot}^{Ryd} = \Psi_{core} \cdot \Psi_{Ryd}$ remains essentially a product of a cationic function times a Rydberg MO and as R$\rightarrow$0 the Rydberg MO transforms into a united atom orbital (UAO) usually without radical change in form, but sometimes with radical change due to an avoided crossing of MO curves at

small R. On dissociation Ψ_{Tot}^{Ryd} will undergo significant configuration mixing with simultaneous changes in the core and Rydberg MOs and therefore the product function Ψ_{Tot}^{Ryd} is no longer valid.

1.2.3 The Rydberg States of I_2

The lowest Rydberg states of I_2 lie about 6 eV (48,000 cm^{-1}) above the ground state where the energy at dissociation of the valence, Rydberg and ion-pair states increases in the order given. Diabatic dissociation of I_2 Rydberg states correlates with one ground state and one excited state atom:I $5p^5(^2P_{3/2,1/2})$ + I^+ $5p^4(^3P, ^1D, ^1S)$nl and it is the energy differences in the I^+ ionic states which largely determine the position of the neutral iodine $5p^4nl$ term values because splittings among the substates formed by coupling a Rydberg electron to the $5p^4$ ion core, in most cases, is much smaller than the splittings in the ionic states as discussed previously in the case of the $J_c l$ coupling scheme of Minnhagen [37] for atomic iodine.

The large well depth ($\sim$ 30,000 cm^{-1}) characteristic of ion-pair states pulls their T_e values below or level with that of the lowest energy Rydberg states giving rise to avoided crossings at large R. The lowest energy Rydberg state, $[^2\Pi_{3/2}]6s : 2_g$, has an electronic origin at $\sim$48,000 cm^{-1} and a dissociation limit at $\sim$ 67,000 cm^{-1} correlating with $I(^2P_{3/2})$+$I^*(^4P_{5/2})$ [43]. Assuming the same general asymptotic form as the ground state, this limb crosses the first three tier ion-pair state attractive branches correlating with $^3P_2$,$^3P_{1,0}$ and $^1D_2$ of I^+ at $\sim$ 20, 10 and 6 Å respectively. Consequently, if the ion-pair and Rydberg states are of the same symmetry, avoided crossings will take place and the Rydberg states will correlate adiabatically with $I^+ + I^-$. This has had little impact on the observed DRINCS spectra presented in chapter 2 because ion-pair states up to $\sim$ 62,000 cm^{-1} from the first three tiers have been accessed, some 5000 cm^{-1} below the asymptotic limit of the lowest Rydberg state. As a result of the large R_e values characteristic of the ion-pair states resulting from their high antibonding orbital occupancies, their inner branches will eventually cross the outer branch of the Rydberg states

which has had an impact on our studies and is discussed in detail in chapters 2 and 5.

Numerous spectroscopic studies of the Rydberg states of I_2 show that these states dominate the spectra obtained by absorption and REMPI techniques [2] where those with lowest energy have the gerade core configuration [2430] resulting from the promotion of an electron from a gerade antibonding π-orbital to a Rydberg orbital. The resulting increased bonding character in the molecular ion core reduces R_e slightly as confirmed by the single-photon VUV absorption studies of Venkateswarlu in which all low lying Ryberg states have violet degraded vibrational resonances following absorption from the ground state [44]. Such odd number photon transitions from the ground state are to p or f Rydberg levels resulting in an overall ungerade state, whilst promotion to s or d Rydberg orbitals maintains an overall gerade symmetry state which are only accessible in an even number photon transition (usually two) from the ground state as shown for example by Donovan et al. in their (2+1) REMPI experiments [36].

The assignment of the particular $nl\lambda$ Rydberg orbital accessed is based on the effective quantum number $n - \delta$ of the electronic origin calculated from equation 1.4 using the ionisation potentials of I_2^+ given by Higginson et al. [45] and by Kvaran et al. [46] for the $[^2\Pi_{3/2g}]$ and $[^2\Pi_{1/2g}]$ spin-orbit states of 75093 and 80271 cm^{-1} respectively.

In I_2 because the spin-orbit coupling is strong at each atom centre the most appropriate coupling scheme is Hund's case (c) where the coupling of the Rydberg electron to the core is jj-coupling. Only Ω, where $\Omega = \omega_c \pm \omega_{Ryd}$, is a good quantum number, ω_c and ω_{Ryd} being the total angular momentum of the molecular ion core and the Rydberg electron respectively. However, coupling between the core and Rydberg electron through electron exchange is fairly small compared to the spin-orbit coupling within the core and providing the electrostatic interaction between the quadrupole moment of the core and the Rydberg electron is small, ω_c, ω_{Ryd} and l_{Ryd} are each good quantum numbers. In the case of s-series, there is no spin-orbit

coupling available to the Rydberg electron and even if $l > 0$, this perturbation will remain small. The electrostatic interaction is second order for an s-electron but leads to first order splitting in the p and d series [47].

The s and d-series Rydberg states with overall gerade symmetry, based on the two spin-orbit components of the ground electronic state of the positive ion core, are primarily responsible for the observed perturbations in the DRINCS spectra discussed in chapter 2. In the case of s-series Rydberg states where $\omega_{Ryd}=\pm 1/2$ we have the following Rydberg states: 0_g, $1_g(^2\Pi_{1/2g})ns\sigma_g$ and 2_g, $1_g(^2\Pi_{3/2g})ns\sigma_g$ and for the d-series Rydberg states, the d-orbital has three types of symmetry, σ, π, δ. With $\omega_{Ryd}=5/2$ or $3/2$, the possible Rydberg states adopting the notation of Wu et al. [48] are: 3_g, $2_g^{5/2}$, $2_g^{3/2}$, $1_g(^2\Pi_{1/2g})nd\sigma_g, \Pi_g, \delta_g$ and 4_g, $3_g^{5/2}$, $2_g^{5/2}$, $1_g^{5/2}$, $3_g^{3/2}$, $2_g^{3/2}$, $1_g^{3/2}$, $0_g(^2\Pi_{3/2g})nd\sigma_g, \Pi_g, \delta_g$, where the superscript refers to ω_{Ryd}. Transitions to these states from the $X0_g^+$ ground state are governed by the two photon selection rules: $\Delta J = 0, \pm 1, \pm 2, \Delta\Lambda = 0, \pm 1, \pm 2$ in hund's case (a) and $\Delta\Omega = 0, \pm 1, \pm 2$ and $0^+ \leftrightarrow 0^+$ where 0 refers to the value of Ω in Hund's case (c) [49].

The splitting of states with different couplings of ω_c to identical cores is not large in the j-j coupling case of I_2 and decreases with increasing n. For the n=6, 7 and 8 s-series Rydberg states with ω=1/2 cores, the splitting between the Ω=0 and 1 states are 556, 281, and 130 cm^{-1} respectively. In the lower series Rydberg states the spin of the Rydberg electron is still more strongly coupled to that of the unpaired electron in the core rather than to ω_c. The core/Rydberg exchange energy couples the two Ω=1 states in each $n\Omega$ cluster, the lower and upper partners assuming triplet and singlet character respectively, which in turn results in the Ω=2 and Ω=1 levels moving closer together and the Ω=0 and Ω=1 interval increasing.

In the next section, the spectroscopic study of the halogens and interhalogens using multiphoton methods is discussed, with particular reference to the observation of ion-pair and Rydberg states of I_2 using REMPI and OODR techniques respectively. The addition of jet-cooling and ionisation detection to the latter

facilitates the DRINCS technique which will be discussed in some detail as it provides the main method in this thesis for probing the ion-pair states of I_2 and their interaction with Rydberg states. With this in mind, various examples of such interactions are given in the experimental methodology. To begin with, a brief theoretical introduction of the coupling between states is given based on the various descriptions of the electronic structure of the ion-pair and Rydberg states presented in the previous sections.

1.3 Homogeneous Interactions

If the two diabatic electronic states of a diatomic molecule labelled Y(R) (in this case a Rydberg state) and Z(R) (in this case an ion-pair state) and indicated by the full lines in figure 1.1, which cross each other at R_C, have the same symmetry then a homogeneous interaction takes place leading to an avoided crossing at R_c indicated by the adiabatic curves represented by dotted lines. As a result, the vibrational levels in the region of the avoided crossing deviate from their expected positions. For a homonuclear diatomic molecule, such an interaction is allowed only when the Ω, inversion and reflection symmetry properties of the two states remain good quantum numbers and satisfy the following selection rules: $\Delta\Omega$=0, g$\longleftrightarrow$g, u$\longleftrightarrow$u, g$\leftarrow/\rightarrow$u, $0^+\longleftrightarrow 0^+$, $0^-\longleftrightarrow 0^-$, $0^+\leftarrow/\rightarrow 0^-$ where 0 refers to the value of Ω, in Hund's case (c) coupling and + and − refers to the total spin and spatial wavefunction. Although the ΔS=0 selection rule is broken down by spin-orbit interaction in I_2 it is still a useful indicator of the magnitude of the interaction.

If the two states differ by $\Delta\Omega = \pm 1$, then irregular rotational structure in the crossing region results from a heterogeneous interaction, where no avoided crossing takes place.

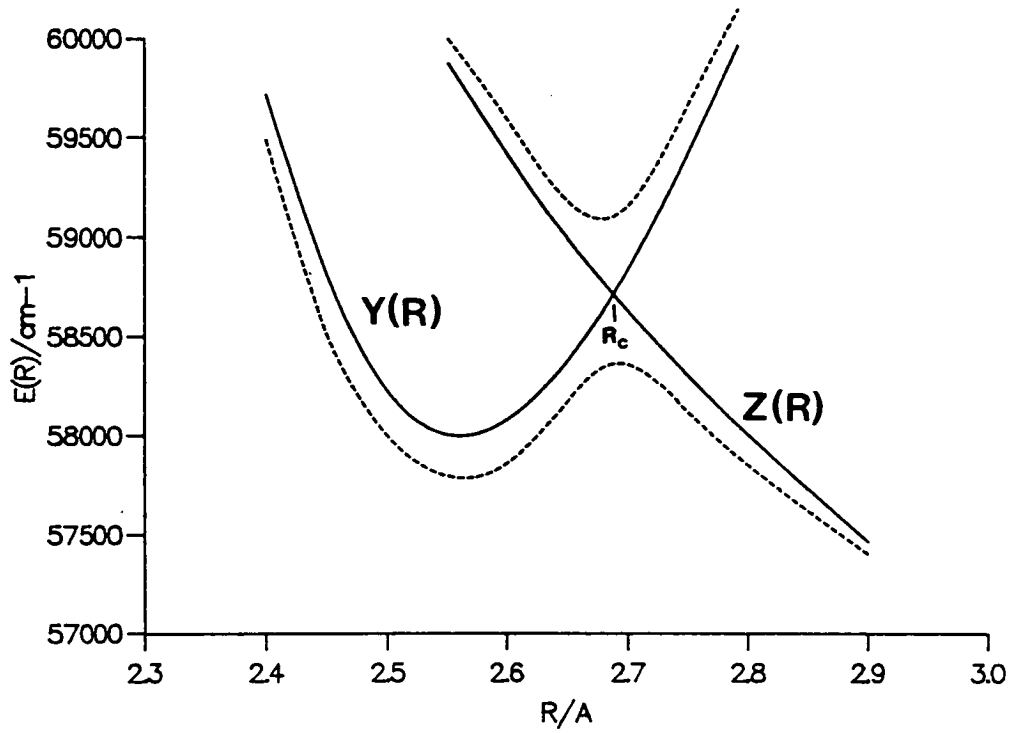

Figure 1.1. The adiabatic potential curves resulting from the homogeneous interaction between two diabatic states, Y(R) and Z(R).

Losses in fluorescence intensity from most, if not all, of the lower Rydberg states of the halogens is most probably due to predissociation, where a homogeneous or heterogeneous interaction with a repulsive (unbound) state takes place. As a result, diffuse or if the interaction is strong enough, complete loss of rovibronic structure occurs above the crossing energy. The inadequacy of these various two-state interaction schemes to explain any observed spectral perturbations may be overcome by using a combination of them, i.e. a three-state coupling mechanism where one state borrows intensity from another state already predissociated.

In general, the magnitude of the various perturbations observed in the spectra depends upon three main factors, the vertical energy separation between the two

interacting states, $\Delta E(R)$, the Franck-Condon (FC) factor between the two perturbing levels, $\langle v'_Y | v'_Z \rangle$, and the off-diagonal electronic matrix element, $\langle Y | H_{YZ} | Z \rangle$, which determines the extent to which the homogeneous crossings are avoided. The factors which govern the magnitude of H_{YZ} will be discussed using the Mulliken MO description which is the most appropriate at $R \leq R_e^{i,p}$ of the halogens in the region where the ion-pair and Rydberg states cross.

In homogeneous interactions, the largest H_{YZ} matrix elements arising from the $1/r_{12}$ Coulomb electronic term, will occur for states which have the same spin multiplicity and differ in orbital occupancy by either one or two electrons. For a two electron transfer, H_{YZ} is largest for two parallel transitions and smallest for two perpencicular ones, i.e $\sigma \longleftrightarrow \sigma > \pi \longleftrightarrow \pi > \sigma \longleftrightarrow \pi$ and the strongest avoided crossing results when the two electrons originate from the same orbital of the ion-pair state rather than originating from different orbitals. When considering interactions involving Rydberg states, for a fixed principal quantum number n, H_{AB} decreases in the order ns, np, nd reflecting the decreasing core penetration of the Rydberg electron as l_{Ryd} increases.

Finally, in the heavier diatomic halogens containing Br and I, the $l_{z_i} s_{z_i}$ component of the spin-orbit operator can convert configurations differing by a single perpendicular electron shift, $\pi_{g,u} \longleftrightarrow \sigma_{u,g}$ ($\Delta\lambda = \pm 1$) and spin multiplicity ($\Delta\Sigma = \mp 1$) [2]. This interaction is generally weaker than the homogeneous $1/r_{12}$ electronic term.

1.4 Experimental Methodology

Before the advent of high intensity tunable dye lasers operating in the visible and near-U.V regions, the observation of molecular Rydberg states was dominated by conventional single photon absorption studies, a technique with many limitations. It was operationally expensive and complicated because O_2 absorption at wave-

lengths below 190 nm required efficiently evacuated beam paths and the use of LiF or MgF_2 optics.

The electric dipole selection rules severely restricted the number of excited states that could be accessed in a one-photon transition from the ground state and because multiple absorption cross-sections are small, typically $\sim 10^{-51} cm^4$ for coherent two-photon transitions [50] the probability of multiphoton absorption occuring was very small using conventional photon sources. Simultaneous absorption of photons occurs if the second photon is incident on the molecule within a sufficiently short period of time, $\sim 10^{-15}$ s where the transition probability (W_n) of an n-photon process is given by $W_n = \sigma_n \cdot I^n$ where σ_n is the cross-section and I^n is the photon flux [51].

In the early 1960s, newly developed tunable dye lasers greatly reduced these limitations, the population of excited states through the multiple absorption of photons of known energy became possible because of the very high photon fluxes associated with these lasers. In particular, tunable dye lasers operating in the visible and near-U.V regions provided spectroscopists studying electronically excited molecular states with more favourable wavelength regimes and overcame the restrictive one-photon selection rules allowing n-photon transitions in homonuclear diatomics using Hund's case (c) notation, Ω=0, $\pm$1, ..., $\pm$n, and g$\rightarrow$g or g$\rightarrow$u for an even or odd n-photon transition from the ground state respectively.

Fluorescence detection provided the most sensitive method of monitoring the excited state in early multiphoton studies but because most Rydberg states lie sufficiently close to the first ionisation potential, so that molecular ion formation requires absorption of just one additional photon, such ions can be detected relatively easily and with a high collection efficiency.

Multiphoton Ionisation (MPI) techniques which were first applied to the halogens in the late 1970s [5] and in particular Resonance Enhanced MPI (REMPI) have dominated the observation of the Rydberg states of these molecules because they are generally strongly predissociated resulting in very low fluorescence detec-

tion quantum yields. In non-resonant MPI, virtual states (which are not eigenstates of the molecule) are populated in a vertical, multi-photon absorption, then a final photon ionises the molecule. A greater enhancement of the ionisation signal is achieved in (m+n) REMPI, where non-resonant absorption of m-photons to an initial intermediate state (which is an eigenstate of the molecule) takes place before n-photons ionises the molecule. REMPI allows the population of specific rovibronic levels to be achieved at each intermediate state and gives access to more excited states of different symmetry. Consequently, the REMPI technique has been successfully applied in several areas including the detection of transient species, the production of state selected ions, trace analysis when coupled to mass spectroscopy and laser desorption and the ionisation of involatile and fragile molecules. Further advances in REMPI have occured using supersonic jet-cooling which considerably reduces the congestion in the spectrum [52].

The first high resolution, single-photon VUV absorption studies for I_2 [44], Br_2 [53] and ICl [54] were carried out by Venkateswarlu who observed several np and nf Rydberg series converging on the $^2\Pi_{3/2}$ and $^2\Pi_{1/2}$ molecular ion core states. The ionisation potentials he obtained have since been improved upon by Higginson [45] and confirmed by Kvaran [46]. Lower energy VUV absorption studies by Donovan et al. on I_2, Br_2, ICl and IBr all show a long, single ion-pair progression corresponding to the $D(0_u^+) \longleftarrow X(0_g^+)$ transition with a sharp Rydberg progression superimposed on it. Towards higher energies, as the intensity of the ion-pair progression reaches a maximum, it abruptly falls off as a result of a strong homogeneous interaction with the [2430]6p:0_u^+ Rydberg state which is probably strongly predissociated.

It is the strong predissociation of many of these Rydberg states of I_2 which results in their fluorescence quantum yields being much smaller than those of the ion-pair states. Small dips in the fluorescence excitation spectra of the $D(0_u^+)$ are observed between 175–179 nm resulting from the heterogeneous perturbation of the ion-pair state by the [243 $^2\Pi_{3/2g}$]6s:1_g Rydberg state [25]. Even more pronounced predissociation is seen in ICl resulting from the heterogeneous interaction of the

$E(0^+)$ ion-pair state and the $[243\ ^2\Pi_{3/2g}]6s{:}1_g$ Rydberg state but Lipson et al. have obtained vibrationally resolved, jet-cooled fluorescence excitation spectra for I_2, Br_2, ICl and IBr [55–57].

The application of the (2+1) REMPI technique to I_2 by Dalby et al. in 1977 provided the first coherent two-photon transitions to gerade Rydberg states [58]. From the vibrational spacings, polarisation data and rotational contour analysis the Rydberg state accessed was assigned $[^2\Pi_{1/2}]6s\sigma_g{:}1_g$ with an origin at 53,560 cm^{-1}. Henceforth, a large number of gerade Rydberg states of I_2 have been observed using this technique by various workers. In 1978, Lehmann et al. [59] observed a Rydberg state with an origin at 48,400 cm^{-1} and assigned it as the other spin-orbit partner of the Dalby system, $[^2\Pi_{3/2g}]6s\sigma_g{:}2_g$. Recently, Dasari et al. have reassigned it as the $[^2\Pi_{3/2g}]6s\sigma_g{:}1_g$ state based on rotational contour analysis [60]. The observation and assignment of the $[^2\Pi_{1/2g}]6s\sigma_g{:}0_g^+$ Rydberg state was reported by Miller et al. in 1987 using mass-selective (2+1) REMPI [61]. Wu et al. [48] employed the same technique over the energy ranges 62,000–64,500 and 67,600–70,000 cm^{-1} and observed four nd Rydberg series. However, these assignments, based on United Atom theory were shown to be incorrect by Donovan et al. [36] as were the observed effective quantum numbers which were in disagreement with the assignments.

Systematic studies of the Rydberg states of I_2 and Br_2 using (2+1) REMPI in the 48,000–85,000 cm^{-1} energy region have been carried out by Donovan et al. [36]. They assigned the $[^2\Pi_{3/2g}]$ns and $[^2\Pi_{1/2g}]$ns Rydberg states up to n=11 and n=8 respectively, together with three 5d states based on each core from quantum defects, rotational band contour analysis and polarisation ratios. In these room temperature studies strong Rydberg transitions dominated the spectra. However, jet-cooled REMPI studies presented in chapter 5 have resolved a mixed Rydberg/ion-pair system above ~58000 cm^{-1}. A detailed study of the vibronic coupling between these states is given in chapter 5.

In a J-selected (1+2) photon double resonance experiment Williamson et al.

observed a small part of an 0_u^+ Rydberg state near 62,000 cm^{-1} [62]. This work was closely followed by another three-photon experiment in which Hoy et al. probed a Rydberg state of I_2 (T_e=61,660 cm^{-1} in a (1+2+1) REMPI scheme via the $B(^3\Pi_{0_u^+})$ valence state [63]. This state which is missing in ordinary one-photon absorption was assigned as the $R0_u^+$ $[^2\Pi_{1/2g}]6p{:}0_u^+$ state and was found to be perturbed by the neighbouring $F0_u^+$ [2332] ion-pair state. In the crossing region local constants were calculated for both states corresponding to v'=220–250 for the ion-pair state. As a result, the spectra is composed of a series of Rydberg levels superimposed on a relatively dense grid of ion-pair levels and because the two states cannot be connected by a spin allowed two-electron shift a weak homogeneous interaction (H_{12}=107 cm^{-1}) takes place when the inner branch of the ion-pair state passes through R_e^{Ryd} and continues up along the centre of the $R0_u^+$ state. As a consequence, the overlap integral, $\langle v'_F|v'_R\rangle$, is large for v'_R=0, 2, 4... and small for v'_R=1, 3, 5... resulting in a perturbation of the even numbered vibrational levels.

1.4.1 The OODR and DRINCS Techniques

In contrast to the coherent REMPI studies discussed previously, the optical-optical double resonance (OODR) technique provides ready access to the ion-pair states of the halogens. In particular, this technique has been used to determine Dunham parameters, lifetimes and transition dipole functions from fluorescence excitation and dispersed fluorescence experiments as well as investigating the hyperfine structure, Ω-doubling and other coupling interactions providing a great deal of information on the detailed electronic structure of the ion-pair states of I_2 [27].

Although technically more complex than REMPI, the OODR technique allows the probing of excited states to take place in a stepwise process via an intermediate resonant state that provides a greater FC window. In a typical two-colour OODR experiment, the first (pump) laser populates a single rovibronic level (v, J) of a bound intermediate state with a wide enough vibrational amplitude to open up a

1.5 References

1. U. Wolf and E. Tiemann, *Chem. Phys.* **119**(1988)407.

2. K. P. Lawley and R. J. Donovan, *J. Chem. Soc. Farad. Trans.* **89**(1993)1885.

3. E. S. Rittner, *J. Chem. Phys.* **19**(1951)1030.

4. J. Tellinghuisen, *Can. J. Phys.* **62**(1984)1933.

5. J. C. D. Brand and A. R. Hoy, *Appl. Spec. Rev.* **23**(1987)285.

6. T. Ishiwata, J-H. Si and K. Obi, *J. Chem. Phys.* **96**(1992)5678.

7. T. Ishiwata, A. Tokunaga, T. Shinzawa and I. Tanaka, *J. Mol. Spec.* **117**(1986)89.

8. G. W. King and T. D. Mclean, *J. Mol. Spec.* **135**(1989)207.

9. T. Ishiwata, J. Yamada and K. Obi, *J. Mol. Spec.* **158**(1993)237.

10. R. J. Donovan, T. Ridley, K. P. Lawley and P. J. Wilson, *Chem. Phys. Lett.* **196**(1992)173.

11. R. J. Donovan, T. Ridley, K. P. Lawley and P. J. Wilson, *Chem. Phys.* **182**(1994)325

12. P. J. Jewsbury, T. Ridley, K. P. Lawley and R. J. Donovan,
J. Mol. Spec. **157**(1993)33

13. K. S. Viswanathan, A. Sur and J. Tellinghuisen,
J. Mol. Spec. **86**(1981)393.

14. T. Ishiwata, T. Kusayanagi, T. Hara and I. Tanaka,
J. Mol. Spec., **119**(1986)337.

15. V. S. Viswanathan and J. Tellinghuisen, *J. Mol. Spec.*, **101**(1983)285.

16. J. P. Perrot, A. J. Bouvier, A. Bouvier, B. Femelat and J.Chevaleyre,
J. Mol. Spec. **114**(1985)60.

17. K. P. Lawley, P.J. Jewsbury, T. Ridley, P. R. R. Langridge-Smith
and R. J. Donovan, *Mol. Phys.* **75**(1992)811.

18. G. W. King, I. M. Littlewood and J. R. Robins,
Chem. Phys. **56**(1981)145.

19. J. C. D. Brand and A. R. Hoy, A. K. Kalkar and A. B. Yamashita,
J. Mol. Spec. **205**(1993)129.

20. T. Ishiwata and I. Tanaka, *Laser Chem.*, **7**(1987)79.

21. J. P. Perrot, B. Femelat, M. Broyer and J. Chevaleyre,
Mol. Phys., **61**(1987)97.

22. J. Tellinghuisen, *J. Mol. Spec.*, **94**(1982)231.

23. J. Tellinghuisen, S. Fei, X. Zheng and M. C. Heaven,
Chem. Phys. Lett., **176**(1991)373.

24. R. S. Mulliken, *J. Chem. Phys.* **55**(1971)228.

25. A. Hiraya, K. Shobatake, R. J. Donovan and A. Hopkirk, *J. Chem. Phys.* **88**(1988)52.

26. H. N. Russell and F. A. Saunders, *J. Astrophys.* **61**(1925)38.

27. P. J. Jewsbury, Ph.D. Thesis Edinburgh 1991.

28. A. D. Buckingham, *Quarterly Reviews*, **13**(1959)183.

29. A. Duncan, *Rydberg Series in Atoms and Molecules.* Academic Press, New York, 1971.

30. R. S. Mulliken, *J. Amer. Chem. Soc.* **86**(1964)3183.

R. S. Mulliken, *J. Amer. Chem. Soc.* **88**(1966)1849.

31. F. Paschen, *Ann. Phys, Lpz.* **27**(1908)565.

32. T. Lymman, *Phys. Rev.* **3**(1914)504.

33. F. S. Bracket, *Nature*, **109**(1922)209.

34. A. F. Pfund, *J. Opt. Soc. Amer.* **16**(1924)193.

35. J. R. Rydberg, *K. Svenska Vetensk Akad. Handl.* **23**(1889).

36. R. J. Donovan, R. V. Flood, K. P. Lawley, A. J. Yencha and T.Ridley, *Chem. Phys.* **164**(1992)439.

37. L. Minnhagen, *Ark. Phys.* **21**(1962)415.

38. G. Racah, *Phys. Rev.* **61**(1942)537.

39. M. Born and J. R. Oppenheimer, *Ann. Phys.* **84**(1927)457.

40. T. Y. Chang, *Rev. Mod. Phys.* **39**(1967)911.

41. R. S. Mulliken, *Acc. Chem. Res.* **9**(1976)7.

42. M. N. R. Ashfold, *Mol. Phys.* **58**(1986)1.

43. C. E. Moore, *Atomic Energy Levels* Vol. III Natl. Bur. Std. 1971.

44. P. Venkateswarlu, *Can. J. Phys.* **48**(1970)1055.

45. B. R. Higginson, D. R. Lloyd and P. J. Roberts, *Chem. Phys. Lett.* **19**(1973)480.

46. A. Kvaran, A. J. Yencha, D. K. Kela, R. J. Donovan and A. Hopkirk, *Chem. Phys. Lett.* **179**(1991)263.

47. K. P. Lawley, R. J. Donovan, T. Ridley, A. J. Yencha and T.Ichimura, *Chem. Phys. Lett.* **168**(1990)168.

48. M. Wu and P. M. Johnson, *J. Chem. Phys.* **90**(1989)74.

49. J. M. Hollas, *High Resolution Spectroscopy.* Butterworth 1982.

50. P. Lambropoulos, *Appl. Opt.* **19**(1976)87.

51. R. V. Flood, M.Phil Edinburgh 1993.

52. R. H. Lipson and A. R. Hoy, *J. Chem. Phys.* **90**(1989)6821.

53. P. Venkateswarlu, *Can. J. Phys.* **47**(1969)2525.

54. P. Venkateswarlu, *Can. J. Phys.* **53**(1975)812.

55. A. R. Hoy and R. H. Lipson, *Chem. Phys.* **140**(1990)187.

56. R. H. Lipson, A. R. Hoy and M. J. Flood,
Chem. Phys. Lett. **149**(1988)155.

57. R. H. Lipson and A. R. Hoy, *Mol. Phys.* **68**(1989)1311.

58. F. W. Dalby, M. H. L. Pryce, G. Petty-Sil and C. Tai, *Can. J. Phys.* **55**(1977)1033.

59. K. K. Lehmann, J. Smolarek and L. Goodman,
J. Chem. Phys. **69**(1978)1569.

60. R. R. Desari and F. W. Dalby, *J. Chem. Phys.* **92**(1990)3984.

61. J. C. Miller, *J. Phys. Chem.* **91**(1987)2589.

62. A. D. Williamson and R. N. Compton, *Chem. Phys. Lett.* **62**(1979)295.

63. A. R. Hoy, S. M Jaywant and J. C. D. Brand, *Mol. Phys.* 60(1987)749.

64. M. D. Danyluk and G. W. King, *Chem. Phys.* **22**(1977)59.

65. M. Broyer, J. Vigue and J. C. Lehmann, *J. Phys.* **39**(1978)591.

66. D. L. Rousseau and P. F. Williams, *Phys. Rev. Lett.* **33**(1974)1368.

67. H. P. Grieneisen and R. E. Francke, *Chem. Phys. Lett.* **88**(1982)585.

U. Heemann, H. Knockel and E. Tiemann, *Chem. Phys. Lett.* 90(1982)17.

J. C. D. Brand and A. R. Hoy, *Can. J. Phys.* **60**(1982)1209.

J. C. D. Brand and A. R. Hoy, *J. Mol. Spec.* **97**(1983)379.

68. A. R. Hoy and A. W. Taylor, *J. Mol. Spec.* **126**(1987)484.

69. R. J. Donovan, T. Ridley, K. P. Lawley and P. J. Wilson, *Chem. Phys. Lett.* **205**(1993)129.

70. R. J. Donovan, T. Ridley, K. P. Lawley and P. J. Wilson, *Chem. Phys. Lett.* **207**(1993)129.

71. R. J. Donovan, J. G. Goode, K. P. Lawley, T. Ridley and A. J. Yencha, *J. Phys. Chem* **98**(1994)2236.

Chapter 2

DRINCS Studies of the E, f and f', 0_g^+ Ion-Pair States of I_2

2.1 Introduction

The observation and identification of ion-pair states is in general quite difficult due to the large change in molecular geometry which accompanies the change in electronic structure on excitation. Franck-Condon factors are generally low and spectra are spread over a wide frequency range.

In contrast to the limited usefulness of coherent two-photon excitation, by using the combination of three techniques, two-colour double resonance, resonance ionisation and jet-cooling, access to the ion-pair manifold can be readily achieved using the DRINCS technique. The ability of this technique to simplify the study of electronic spectra in congested regions, particularly in the study of ion-pair states of halogens which support a high density of rovibronic levels as a result of their very long range ($1/R$) attractive limbs, is demonstrated in this chapter.

In this chapter, we report the first observation of the lower vibrational levels and the location of the origin of a third tier gerade ion-pair state of I_2, the $f'0_g^+(^1D_2)$ state. A brief report on the high vibrational levels of this state have been reported by Hoy et al. [1] but the origin was not located. In addition, medium-high vibrational levels of the three lowest energy 0_g^+ ion-pair states of I_2 have also been characterised via the resonant intermediate B state. At higher

energies ($\geq$55400 cm^{-1}) the vibrational levels of the three ion-pair states overlap and the spectrum is further complicated by mixing between the ion-pair and Rydberg states producing very irregular band intensities, though, as we will see, with relatively small displacements of the term values.

The form of the electronic transition dipole function provides an insight into the change in electronic configuration of both upper and lower states with the atomic separation. In the case of the $f' \rightarrow B$ transition, determining the radial dependence of $\mu_{f' \rightarrow B}(R)$ is relatively straightforward because both potentials are well known in the radial region covered by the dispersed fluorescence. In this region the red extremum in the fluorescent intensity arises from a maximum in the Mulliken difference potential. The dispersed fluorescence data is combined with the measured lifetime of the $f'(v'=0)$ level to produce the absolute transition dipole function whose behaviour is discussed in terms of the changing electronic configurations using the molecular orbital and $J_A M_A J_B M_B$ bonding descriptions. The Einstein A-coefficients and $\mu_{12}(R)$ values for five first-cluster and three second-cluster ion-pair states of I_2 at their respective R_e values have been reported in a previous paper [2]. Only the $f \rightarrow B$ and $F \rightarrow X$ transition dipole functions have been reported in the literature [3,4].

2.2 Experimental Techniques

2.2.1 DRINCS Technique

All the experimental work and assignment of spectra in this thesis was performed by Dr Trevor Ridley. Assistance in the assignment of the DRINCS spectra was provided by myself particularly in the congested and perturbed spectral regions. The DRINCS experimental arrangement is a simple one. DRINCS spectra were recorded using a free jet-expansion where the jet system was of conventional design and employed a pulsed valve, with a nozzle diameter of 250 μm. The molecular

beam was then expanded through the pulsed nozzle into a vacuum chamber. The chamber was pumped by a 1500 ls^{-1} oil diffusion pump fitted with a liquid nitrogen trap; the pressure in the chamber, under load from the pulsed nozzle, was typically $\leq 5\times10^{-5}$ Torr. The ion-current was detected by parallel plate electrodes positioned either side of the jet (separated by 2 cm), amplified, processed by a boxcar and stored on a PC.

A double-resonance excitation scheme is employed to access the ion-pair vibrational levels. A pump laser was locked on to the band head of the particular transition which selectively excites single rovibronic levels of the intermediate state, $v, J = J'' \pm 1$, from v''=0, J'' of the ground state. The probe laser was scanned over the rquired wavelength range. The UV radiation was generated by a Lambda Physik FL3002E dye laser pumped by a Lambda Physik EMG201MSC excimer laser operating at 308 nm on the XeCl line. The two counterpropagating dye laser beams were overlapped ~5 mm downstream from the nozzle. The probe laser was focussed by a 4 cm focal length lens. Wavelength calibration of the probe laser was achieved using the I_2 atlas for $\lambda \geq$500 nm and an optogalvanic signal for $\lambda \leq$500 nm.

2.2.2 Dispersed Fluorescence and Fluorescence Lifetime Techniques

Dispersed fluorescence was recorded at room temperature using a static gas cell as it was not physically possible to observe fluorescence using the present jet-cooled system. The double-resonance excitation scheme was achieved using the laser system described above. Fluorescence was collected at right angles to the laser paths and imaged on to the entrance slit of a monochromator (Jobin-Yvon HRS2; f/7, 0.6 m); dispersed fluorescence at the exit slit was monitored by a photomultiplier (Hamamatsu R928: rise time 2.2 ns) whose transient output was fed into an Stanford Research Systems SR250 gated integrator (gate width less than 2 ns) and interfaced to a PC. The boxcar gate was scanned across the fluorescence decay profile collected at the wavelength of the strongest transition.

2.2.3 The Jet-Cooled REMPI Linear Time-of-Flight (TOF) technique

The REMPI spectra were recorded using the free-jet and laser systems described previously. The laser radiation was focussed by a 4 cm focal length lens to a point about 2 cm downstream from the nozzle tip which lay in the ionisation region of a linear TOF mass spectrometer.

Since theory predicts a power squared dependence for a coherent two-photon absorption via a virtual intermediate state all spectra were normalised to the square of the laser power. While the power dependence of the ion signal has not been determined this is assumed to be a reasonable approximation in a region where, energetically, a third photon can always ionise the molecule.

2.3 DRINCS Studies of the f'0_g^+ State

In this section we report the first observation of the lower vibrational levels and the location of the origin of a third-tier gerade ion-pair state of I_2.

2.3.1 Experimental

The DRINCS experimental arrangement is discussed in the previous section. The The $f'0_g^+(^1D_2)$ state of I_2 was accessed using the following excitation scheme.

$$f'0_g^+(^1D_2), v' = 0-45 \longleftarrow B0_u^+, v = 14 or 22 \longleftarrow X0_g^+, v'' = 0$$

The pump laser (ν_1) was locked on the (14,0) or (22,0) band head of the B⟵X transition and the probe laser (ν_2) was scanned over the wavelength range 300–221 nm (two-photon energy=51000–63000 cm^{-1}). Typical nozzle backing pressures of 0.5 atms were used with a gas mixture of ≈ 0.2-1.0 % halogen in argon. The dyes

used were R6G or C153 and frequency-doubled R6G, C153, C307, C102 or C47 in the pump and probe lasers, respectively.

2.4 Results and Discussion

Observations on states in the third ion-pair tier of the halogens (correlating with $X^+(^1D_2)$ + $X^-(^1S_0)$ are relatively sparse. Six states in total are expected (0_g^+, 0_u^+, 1_g, 1_u, 2_g and 2_u) but of these only the the F' $0_u^+(^1D_2)$ and $f'0_g^+(^1D_2)$ have been reported, the latter using a four-photon transition [1]. Furthermore, only high vibrational levels (v' >100) of the $f'0_g^+(^1D_2)$ state have been observed to date and reliable molecular constants are thus not available.

The observed spectra are very sharp and simple in structure, as shown in figure 2.1). Transitions are also observed to two other lower energy ion-pair states, the $E0_g^+(^3P_2)$ and the $f0_g^+(^3P_0)$ states, which lie in the first and second ion-pair tiers, respectively. Both these states are readily identified from previous spectroscopic studies, although the vibrational levels observed in this work have not been previously reported. Higher vibrational levels of these states were observed in later experiments and are discussed in the next section.

A full list of the vibrational levels observed here for the $f'0_g^+(^1D_2)$ state is given in table 2.1. The vibrational numbering in the $f'0_g^+(^1D_2)$ state was established by observing the nodal structure of the dispersed fluorescence from the v'=2 and 3 levels using the technique discussed in section 2.2.2. **(see appendix A)**

The first 19 vibrational levels, making up the data set of highest accuracy ($\pm$0.4 cm^{-1}). The calculated ratio $x_e(= w_e x_e / w_e)$ is -0.002, lying in the range from -1.7×10^{-3} to -3×10^{-3} characteristic of ion-pair states, but much smaller than the values characteristic of valence or Rydberg states. Another 17 levels of lower precision ($\pm$1 cm^{-1}) were then added with half the weight, bringing the highest quantum number to 45 and this combined data set was added to the higher lying levels observed in the next section to give polynomial cofficients shown in

table 2.5. Measurements in the separations have been made between J=68 and 70 for v'=2 to 18 from OODR fluorescence excitation in a static gas cell using the v=17, J=69 rotational level of the B state as intermediate. These gave the B_v=0.0176±0.0011 cm^{-1}, which, within our precision does not appear to change over the range $0 \leq v' \leq 18$. This indicates a rather small value of α_e no greater than 6×10^{-5} cm^{-1}. Hoy and Taylor give the value B_v=0.0146 cm^{-1}, which we now know refers to v values around 116 and to connect these two values of B_v requires $\alpha_e = 2.6 \times 10^{-5}$ cm^{-1}. Taking this value for α_e, we obtain the value R_e=3.88±0.03 Å.

Figure 2.1. DRINCS spectrum of I_2 via the $B(v{=}14)$ level, in the region of the origin of the f' state.

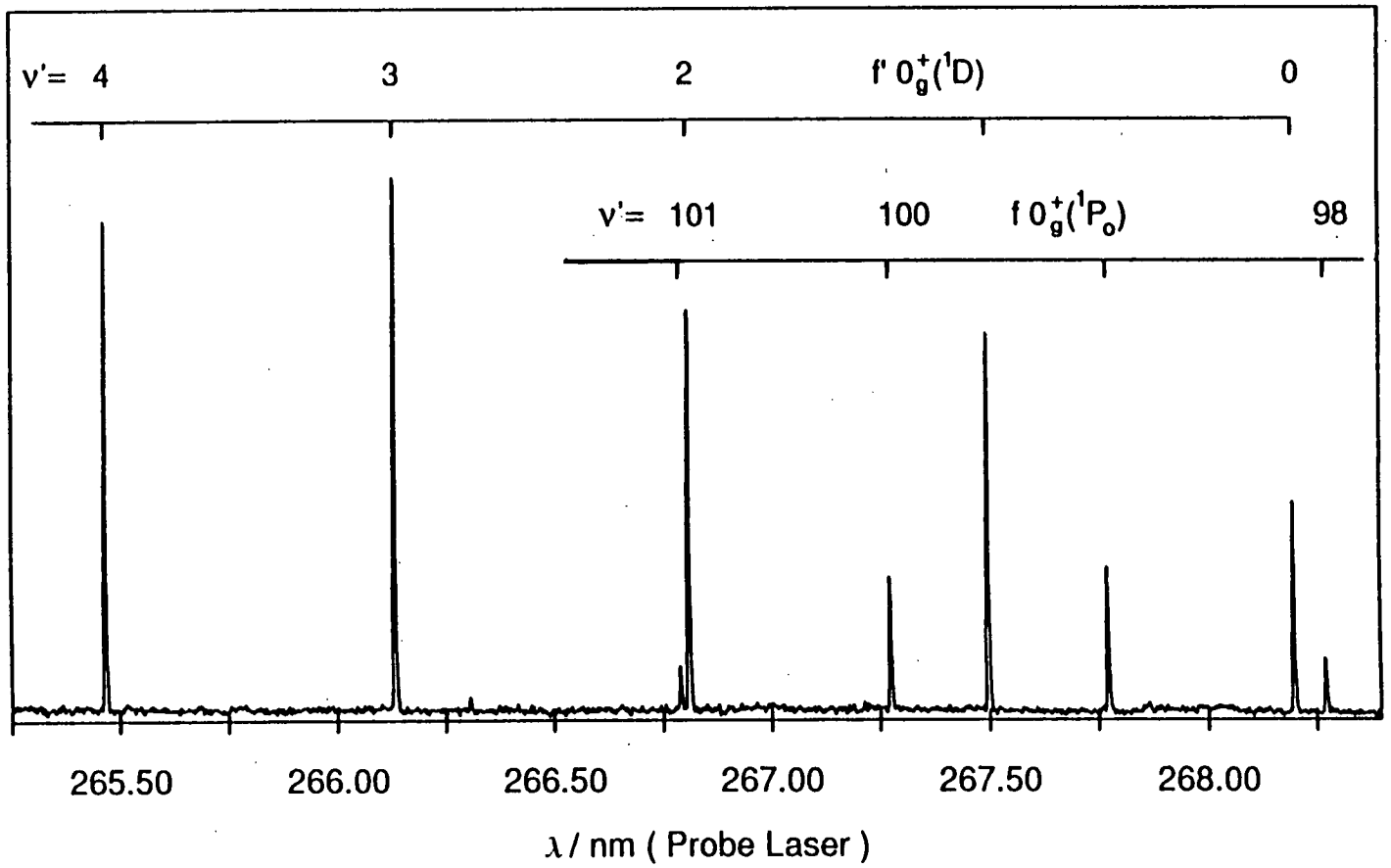

v'	$\tilde{\nu}$ (cm^{-1})	$\tilde{\nu}_{obs-calc}$ (cm^{-1})	v'	$\tilde{\nu}$ (cm^{-1})	$\tilde{\nu}_{obs-calc}$ (cm^{-1})
0	55457.9	–0.2	24	57676	–0.5
1	55554.7	0.0	25	–	–
2	55651.0	0.0	26	57852	0.0
3	55747.0	–0.1	27	57939	0.0
4	55842.5	–0.1	28	58026	0.0
5	55937.6	0.0	29	57114	+1.0
6	56032.4	0.0	30	–	–
7	56126.8	0.0	31	–	–
8	56220.8	0.0	32	58371	+0.5
9	56314.5	0.0	33	58456	–0.5
10	56407.9	+0.1	34	–	–
11	56500.9	+0.1	35	58625	0.0
12	56593.4	0.0	36	58708	+1.0
13	56685.6	0.0	37	58793	0.0
14	56777.4	+0.1	38	58877	–0.5
15	56868.8	–0.1	39	58959	–0.5
16	56960.0	–0.1	40	–	–
17	57050.8	+0.1	41	–	–
18	57141.3	0.0	42	–	–
19	–	–	43	59289	0.0
20	–	–	44	59371	–0.5
21	–	–	45	59452	0.0
22	57500	+0.5			
23	57588	0.0			

Table 2.1. Term values for vibrational levels of the $f'0_g^+(^1D)$ state of I_2.

2.5 DRINCS Studies of the E, f and f' States

In this section, the medium-high vibrational levels of the three lowest energy 0_g^+ ion-pair states of I_2 are characterised. At higher energies ($\geq$55400 cm^{-1}) the vibrational levels of these three states overlap and the spectrum is further complicated by mixing between the ion-pair and Rydberg states. The ability of the DRINCS technique to simplify the study of such spectra in congested regions is powerfully demonstrated.

2.5.1 Experimental

The DRINCS experimental arrangement is described in section 2.2.1. The double-resonance excitation scheme employed to access the vibrational manifolds of the three 0_g^+ ion-pair states was as follows,

$$E, f, f'(0_g^+)v' \xleftarrow{\nu_2} B(0_u^+), v = 14 \xleftarrow{\nu_1} X(0_g^+), v'' = 0$$

The pump laser (ν_1) was locked on the (14,0) band head of the B$\longleftarrow$X transition and the probe laser (ν_2) was scanned over the wavelength range 300–221 nm (two-photon energy=51000–63000 cm^{-1}). Typical nozzle backing pressures of 0.5 atms were used with a gas mixture of $\approx$ 0.2–1.0 % halogen in argon. The dyes used were R6G or C153 and frequency-doubled R6G, C153, C307, C102 or C47 in the pump and probe lasers, respectively.

The fluorescence lifetime of v'=0, $J' \leq 10$ of the f' state was determined using a different excitation scheme where the first step involves excitation into the head of the (22,0) band, i.e

$$f'(0_g^+)(v = 0) \longleftarrow B(0_u^+)(v = 22) \longleftarrow X(0_g^+)(v = 0)$$

The experimental configuration is described in section 2.2.2. In both experiments C153 and frequency-doubled C307 were used in the pump and probe lasers respectively. In view of the large fluorescence lifetime observed no pulse shortening of the normal probe laser output (~13 ns) was necessary. Fluorescence was collected at 270 nm.

2.6 Results

2.6.1 The DRINCS Spectra

The DRINCS spectrum in the two-photon energy region 51000–62500 cm^{-1} is shown in figure 2.2. The spectrum is a composite of over 20 shorter scans. In view of the unavoidable small variations in the jet conditions and the laser beam overlap from scan to scan the spectra were not normalised to the power of the probe laser. Thus although the intensity of a band at, say, 62000 cm^{-1} cannot be compared directly with another 10000 cm^{-1} away, the relative intensities of a local series of bands over a range of a few hundred wavenumbers should be accurate to ±10%. Three ion-pair state vibrational progressions are readily identified from previous studies [5, 6, 7]. The E, f and f' 0_g^+ states lie in the first, second and third ion-pair tiers respectively and have markedly different vibrational spacings at a given ν_2. The low energy region of the spectrum is quite regular with what appear to be periodic Franck-Condon (FC) lobes of intensity. The intensities of the bands in the high energy region are very irregular suggesting some interactions of the ion-pair states with other electronic, probably Rydberg, states. Despite these intensity irregularities we have been able to follow all three progressions up to ~62000 cm^{-1} even through energy regions where the spectra become congested or where interactions occur. A full list of the term values of the three states are presented in tables 2.2, 2.3 and 2.4. Term values of the E state from v'=0–95 were regenerated from the published constants of Brand et al. [6] and combined with our levels which were initially assigned quantum numbers v=n, n+1,... n+299. Levels

up to n+137 made up the set with highest accuracy($\pm$0.4 cm^{-1}). The remaining levels of lower precision ($\pm$1 cm^{-1}) were then added with half the weight of the lower set. The combined data set was fitted to a ninth-order polynomial in $(v+\frac{1}{2})$ and n was adjusted to give a minimum standard deviation, resulting in n=123. From an analysis of how the standard deviation changes as n is varied, this absolute numbering would seem unambiguous because $n\pm1$ results in a ten-fold increase in the standard deviation using a ninth-order fit. The Dunham coefficients from the ninth-order fit are given in table 2.5.

A similar procedure was used to fit the vibrational levels v'=40–228 of the $f(0_g^+)$ state. Our data overlaps with a lower set of levels, generated from the constants of Ishiwata et al. which were valid between v'=0–101 [7]. The overlapping levels agree to within $\pm$0.2 cm^{-1}. The seventh order Dunham coefficients shown in table 2.4 were generated by combining the previous data for v'=0–101 with the present data for v'=102–228 where levels beyond v'=109 were added with half the weight.

v'	$\tilde{\nu}$ (cm^{-1})	$\tilde{\nu}_{obs-calc}$ (cm^{-1})	v'	$\tilde{\nu}$ (cm^{-1})	$\tilde{\nu}_{obs-calc}$ (cm^{-1})	v'	$\tilde{\nu}$ (cm^{-1})	$\tilde{\nu}_{obs-calc}$ (cm^{-1})
123	51214.4	− 0.4	165	53526.2	+ 0.5	207	-	-
124	51274.6	− 0.2	166	53576.3	+ 0.5	208	55501.4	− 0.4
125	51334.4	− 0.2	167	53626.0	+ 0.3	209	55543.4	− 0.3
126	51393.9	− 0.3	168	53675.7	+ 0.3	210	-	-
127	51453.0	− 0.4	169	53725.2	+ 0.3	.	.	.
128	51512.1	− 0.3	170	53774.5	+ 0.3	.	.	.
129	51571.0	− 0.2	171	53823.6	+ 0.4	.	.	.
130	51629.5	− 0.2	172	53872.2	+ 0.1	230	-	-
131	51687.7	− 0.2	173	53921.0	+ 0.3	231	56425.2	+ 0.7
132	51745.5	− 0.4	174	53969.5	+ 0.4	232	56463.3	+ 0.6
133	51803.5	− 0.1	175	54017.9	+ 0.5	233	-	-
134	51860.9	− 0.2	176	54065.5	+ 0.1	.	.	.
135	51918.2	− 0.2	177	54113.7	+ 0.4	.	.	.
136	51975.2	− 0.2	178	54161.1	+ 0.2	.	.	.
137	52032.0	− 0.1	179	54208.8	+ 0.5	246	-	-
138	52088.3	− 0.3	180	54255.9	− 0.3	247	57018.8	+ 0.1
139	52145.0	+ 0.1	181	-	-	248	57054.7	+ 0.1
140	52200.8	− 0.1	182	-	-	249	-	-
141	52256.8	+ 0.1	183	-	-	250	57125.8	− 0.3
142	52312.1	− 0.1	184	-	-	251	57161.0	− 0.6
143	52367.5	+ 0.0	185	54489.2	+ 0.4	252	-	-
144	52422.7	+ 0.2	186	54535.2	+ 0.3	253	57231.1	− 1.1
145	52477.6	+ 0.2	187	54581.0	+ 0.3	254	-	-
146	52532.1	+ 0.2	188	54626.6	− 0.4	.	.	.
147	-	-	189	54671.8	− 0.1	.	.	.
148	-	-	190	54717.0	− 0.2	.	.	.
149	52694.3	+ 0.0	191	-	-	259	-	-
150	52747.9	+ 0.0	192	54807.0	− 0.3	260	57476.0	+ 0.9
151	52801.4	+ 0.1	193	54851.9	− 0.2	261	57510.6	+ 1.3
152	52854.5	+ 0.0	194	54896.4	− 0.2	262	57545.0	+ 1.6
153	52907.4	− 0.1	195	54940.8	− 0.2	263	57577.7	+ 0.4
154	52960.5	+ 0.3	196	54984.9	− 0.3	264	57609.9	− 1.2
155	53013.0	+ 0.2	197	55028.7	− 0.5	265	-	-
156	53065.0	+ 0.0	198	55072.7	− 0.4	266	57677.9	− 0.2
157	53117.4	+ 0.3	199	55116.2	− 0.5	267	57711.0	− 0.7
158	53169.1	+ 0.2	200	55159.7	− 0.5	268	-	-
159	53220.7	+ 0.1	201	55203.0	− 0.5	.	.	.
160	53272.2	+ 0.2	202	-	-	.	.	.
161	53323.5	+ 0.3	203	55289.2	− 0.4	.	.	.
162	53374.4	+ 0.3	204	55331.7	+ 0.7	272	-	-
163	53425.1	+ 0.2	205	55374.0	− 1.0	273	57908.9	− 0.7
164	53475.6	+ 0.2	206	55416.2	− 1.2	274	57942.0	− 0.1

Table 2.2a. Term values for the vibrational levels of the $E0_g^+(^3P_2)$ state of I_2.

v'	$\tilde{\nu}$ (cm^{-1})	$\tilde{\nu}_{obs-calc}$ (cm^{-1})	v'	$\tilde{\nu}$ (cm^{-1})	$\tilde{\nu}_{obs-calc}$ (cm^{-1})	v'	$\tilde{\nu}$ (cm^{-1})	$\tilde{\nu}_{obs-calc}$ (cm^{-1})
275	57974.7	+ 0.2	325	59455.1	+ 0.3	374	60679.7	+ 0.7
276	58007.3	+ 0.4	326	-	-	375	60702.3	+ 0.3
277	58038.7	- 0.3	327	-	-	376	60725.0	+ 0.1
278	-	-	328	59535.8	+ 0.2	377	-	-
279	58105.0	+ 1.9	329	59562.0	- 0.4	378	60769.0†	- 1.6
280	58136.5	+ 1.6	330	59588.3	- 0.8	379	60788.9†	- 4.4
281	58168.2	+ 1.6	331	59614.1	- 1.5	380	-	-
282	58199.3	+ 1.1	332	59641.1	- 1.0	381	-	-
283	58229.2	- 0.5	333	59667.6	- 0.9	382	60862.9	+ 1.9
284	-	-	334	59693.6	- 1.2	383	60883.8	+ 0.3
285	-	-	335	59720.9	- 0.1	384	60905.7	- 0.1
286	58324.1	+ 0.6	336	59747.1	- 0.1	385	60928.6	+ 0.5
287	58354.9	+ 0.4	337	59772.7	- 0.5	386	60951.6	+ 1.2
288	58385.2	- 0.2	338	59798.2	- 0.9	387	60973.4	+ 0.9
289	58415.8	- 0.4	339	59825.5	+ 0.5	388	60994.8	+ 0.2
290	58447.6	+ 0.7	340	59850.3	- 0.5	389	61016.8	+ 0.2
291	-	-	341	-	-	390	61038.8	+ 0.3
.	.	.	342	-	-	391	61062.0	+ 1.6
.	.	.	343	59927.9	+ 0.3	392	61082.4	+ 0.2
.	.	.	344	59952.6	- 0.5	393	61102.9	- 1.0
298	-	-	345	59977.6	- 0.8	394	61124.7	- 0.9
299	58717.9	- 0.2	346	60003.2	- 0.5	395	61146.6	- 0.6
300	58747.4	- 0.3	347	60027.9	- 1.0	396	61167.3	- 1.4
301	58777.3	+ 0.1	348	-	-	397	61188.9	- 1.3
302	58806.7	+ 0.1	349	60080.2	+ 1.2	398	61209.5	- 2.0
303	58837.0	+ 1.1	350	60104.8	+ 0.9	399	61231.0	- 1.9
304	-	-	351	60128.6	- 0.2	400	-	-
305	-	-	352	60152.6	- 1.0	401	61276.6	+ 1.3
306	58924.4	+ 1.2	353	60177.1	- 1.2	402	61298.1	+ 1.7
307	58952.6	+ 0.6	354	60202.0	- 0.9	403	-	-
308	58981.1	+ 0.3	355	60226.2	- 1.2	.	.	.
309	59008.7	- 0.8	356	60249.1†	- 2.8	.	.	.
310	59036.9	- 1.1	357	-	-	.	.	.
311	-	-	358	-	-	408	-	-
312	59091.7†	- 3.2	359	60326.4	+ 1.6	409	61440.5	- 1.7
313	59120.8†	- 2.3	360	60349.4	+ 0.5	410	61461.3	- 1.4
314	59149.9	- 1.4	361	60373.3	+ 0.3	411	-	-
315	59178.3	- 1.1	362	60397.0	+ 0.0	.	.	.
316	59207.2	- 0.2	363	60420.1	- 0.8	.	.	.
317	-	-	364	-	-	.	.	.
318	-	-	.	.	.	416	-	-
319	-	-	368	60549.5†	+ 10.2	417	61604.4	- 0.2
320	59319.6	+ 1.3	369	60568.8†	+ 6.0	418	61623.8	- 0.8
321	-	-	370	60589.2†	+ 3.0	419	61645.4	+ 0.9
322	59374.1	+ 0.9	371	60610.8	+ 1.3	420	61664.8	+ 0.4
323	59401.6	+ 1.1	372	60634.3	+ 1.6	421	61684.6	+ 0.5
324	59428.1	+ 0.4	373	60657.5	+ 1.6	422	61704.8	+ 1.0

† indicates this level has been removed from the fit.

Table 2.2b. Term values for the vibrational levels of the $E0_g^+(^3P_2)$ state of I_2.

v'	$\tilde{\nu}$ (cm^{-1})	$\tilde{\nu}_{obs-calc}$ (cm^{-1})	v'	$\tilde{\nu}$ (cm^{-1})	$\tilde{\nu}_{obs-calc}$ (cm^{-1})	v'	$\tilde{\nu}$ (cm^{-1})	$\tilde{\nu}_{obs-calc}$ (cm^{-1})
40	50912.2	+ 0.2	82	54305.7	+ 0.2	138	57989.0	- 0.1
41	50999.6	- 0.4	83	54379.5	+ 0.3	139	-	-
42	51087.2	- 0.3	84	54453.0	+ 0.4	140	-	-
43	51175.0	+ 0.3	85	54525.9	+ 0.2	141	58166.1†	+ 3.2
44	51261.2	- 0.4	86	-	-	142	58221.6	+ 1.2
45	51348.2	+ 0.1	87	54671.8†	+ 0.9	143	58279.0	+ 1.4
46	51434.0	- 0.2	88	54743.2	+ 0.1	144	58335.5	+ 1.0
47	51520.0	+ 0.1	89	54815.1	+ 0.1	145	58391.3	+ 0.0
48	-	-	90	54886.7	+ 0.2	146	-	-
49	51690.5	+ 0.1	91	54958.0	+ 0.2	147	-	-
50	51774.8	- 0.3	92	55028.7	- 0.1	148	-	-
51	51859.4	+ 0.0	93	55099.2	- 0.2	149	-	-
52	51943.3	- 0.1	94	55169.6	- 0.2	150	-	-
53	52026.9	- 0.1	95	55239.9	+ 0.0	151	58727.0	+ 0.3
54	52110.3	+ 0.0	96	55309.7	+ 0.1	152	58782.3	+ 0.6
55	52193.4	+ 0.2	97	55379.1	+ 0.0	153	-	-
56	52275.8	+ 0.0	98	55448.5	+ 0.2	154	-	-
57	52358.2	+ 0.2	99	55517.2	+ 0.0	155	-	-
58	52439.8	- 0.1	100	55585.9	+ 0.1	156	-	-
59	52521.5	+ 0.0	101	55654.1	+ 0.0	157	-	-
60	52602.7	+ 0.0	102	55721.9	- 0.3	158	-	-
61	52683.6	+ 0.1	103	55789.4	- 0.5	159	59160.0	- 0.9
62	52764.3	+ 0.2	104	55856.7	- 0.7	160	-	-
63	52844.4	+ 0.1	105	55924.1	- 0.4	161	-	-
64	52924.4	+ 0.3	106	55990.9	- 0.5	162	59319.6	- 0.4
65	53003.7	+ 0.1	107	56057.7	- 0.3	163	59372.7	+ 0.1
66	53082.7	- 0.1	108	56124.1	- 0.2	164	-	-
67	53161.9	+ 0.2	109	56189.1	- 1.3	165	-	-
68	53240.4	+ 0.2	110	-	-	166	-	-
69	53318.6	+ 0.2	.	.	.	167	-	-
70	53396.8	+ 0.6	.	.	.	168	-	-
71	-	-	.	.	.	169	-	-
72	53551.2	+ 0.2	125	-	-	170	59735.9	+ 1.2
73	53628.1	+ 0.2	126	57271.0	- 0.4	171	59785.4	- 0.2
74	53704.7	+ 0.3	127	-	-	172	59837.0	+ 0.7
75	53781.0	+ 0.3	.	.	.	173	-	-
76	53856.8	+ 0.2	.	.	.	174	59937.2	+ 0.2
77	53932.4	+ 0.2	.	.	.	175	59986.6	- 0.4
78	54008.0	+ 0.5	134	-	-	176	60036.8	+ 0.0
79	54082.9	+ 0.5	135	57813.5	+ 0.4	177	-	-
80	54157.3	+ 0.2	136	57872.6	+ 0.6	178	60135.8	- 0.1
81	54231.9	+ 0.5	137	57930.5	- 0.2	179	60185.2	+ 0.1

Table 2.3a. Term values for the vibrational levels of the $f0_g^+(^3P_0)$ state of I_2.

v'	$\tilde{\nu}$ (cm^{-1})	$\tilde{\nu}_{obs-calc}$ (cm^{-1})	v'	$\tilde{\nu}$ (cm^{-1})	$\tilde{\nu}_{obs-calc}$ (cm^{-1})	v'	$\tilde{\nu}$ (cm^{-1})	$\tilde{\nu}_{obs-calc}$ (cm^{-1})
180	60233.5	− 0.6	197	61036.9	− 0.1	214	61787.9	+ 1.9
181	-	-	198	61082.4	− 0.1	215	61829.7	+ 1.3
182	60331.6	+ 0.1	199	61127.6	− 0.2	216	61870.0	− 0.8
183	60380.0	+ 0.1	200	61172.5	− 0.5	217	-	-
184	60428.1	+ 0.0	201	61218.9	+ 1.0	218	61956.2	+ 1.4
185	60476.1	+ 0.0	202	-	-	219	61996.0	− 0.6
186	60523.0	− 0.9	203	61308.6	+ 1.3	220	62038.8	+ 0.6
187	60571.1	− 0.4	204	61352.3	+ 0.6	221	62079.5	− 0.2
188	60617.3	− 1.6	205	-	-	222	62121.2	+ 0.2
189	-	-	206	61439.5	− 0.5	223	62161.9	− 0.2
190	60713.0	− 0.2	207	61482.9	− 0.9	224	62201.8	+ 1.3
191	60760.7	+ 0.7	208	-	-	225	62243.7	− 0.2
192	60807.3	+ 0.7	209	-	-	226	-	-
193	-	-	210	61614.7	+ 0.3	227	62325.4	+ 0.5
194	60897.0†	− 2.3	211	61657.1	− 0.4	228	62364.8	− 0.4
195	60944.8	− 0.6	212	61699.9	− 0.6			
196	60989.7	− 1.6	213	-	-			

† indicates this level has been removed from the fit.

Table 2.3b. Term values for the vibrational levels of the $f0_g^+(^3P_0)$ state of I_2.

v'	$\tilde{\nu}$ (cm^{-1})	$\tilde{\nu}_{obs-calc}$ (cm^{-1})	v'	$\tilde{\nu}$ (cm^{-1})	$\tilde{\nu}_{obs-calc}$ (cm^{-1})
44	59370.5	− 0.4	64	60935.5	− 0.4
45	59452.2	+ 0.1	65	-	-
46	59532.6	− 0.5	66	61084.4	− 1.2
47	59612.2	− 1.5	67	61158.5	− 1.5
48	59693.6	− 0.3	68	-	-
49	59772.7	− 1.2	69	-	-
50	59853.8	+ 0.3	70	-	-
51	-	-	71	-	-
52	60012.1	+ 0.2	72	-	-
53	60091.1	+ 0.5	73	-	-
54	60168.8	− 0.2	74	-	-
55	60246.5	− 0.5	75	61745.3	+ 0.4
56	60324.1	− 0.7	76	-	-
57	60402.5	+ 0.3	77	-	-
58	60479.1	− 0.3	78	-	-
59	60556.2	+ 0.0	79	62032.4	+ 2.0
60	-	-	80	62103.6	+ 2.5
61	-	-	81	62173.5	+ 2.0
62	-	-	82	62243.7	+ 2.1
63	-	-			

Table 2.4. Term values for the vibrational levels of the $f'0_g^+(^1D_2)$ state of I_2.

In the previous section, vibrational levels of the f' 0_g^+ state were observed using the DRINCS technique valid between v'=0–45. We now report additional vibrational levels between v'=46–82 as shown in table 2.4, with a precision of ± 1 cm^{-1}. Combining the DRINCS data valid between v'=0–82 with levels from v'=116–166 regenerated from local vibrational constants obtained from a 1+2+1 triple resonance experiment [1] produce fifth-order Dunham coefficients valid up to v'=166 which are displayed in table 2.5.

Dunham coefficients	E state/cm^{-1}(a)	f state/cm^{-1}(b)	f' state/cm^{-1}(c)
$Y_{0,0}$	41411.8	47026.2	55409.9
$Y_{1,0}$	101.3628	104.1447	96.980
$Y_{2,0}$	-1.97930×10^{-1}	-2.11335×10^{-1}	-1.865×10^{-1}
$Y_{3,0}$	1.42008×10^{-4}	2.0787×10^{-4}	1.4570×10^{-4}
$Y_{4,0}$	4.2509×10^{-8}	3.994×10^{-7}	5.859×10^{-7}
$Y_{5,0}$	2.006652×10^{-9}	-3.2408×10^{-9}	-2.245×10^{-9}
$Y_{6,0}$	-1.176028×10^{-11}	9.9970×10^{-12}	
$Y_{7,0}$	2.698456×10^{-14}	-1.2204×10^{-14}	
$Y_{8,0}$	-2.86383×10^{-17}		
$Y_{9,0}$	1.12822×10^{-20}		

Table 2.5. Vibrational Dunham coefficients for the E, f and f' states of I_2.

(a) valid up to v'=422

(b) valid up to v'=228

(c) valid up to v'=166

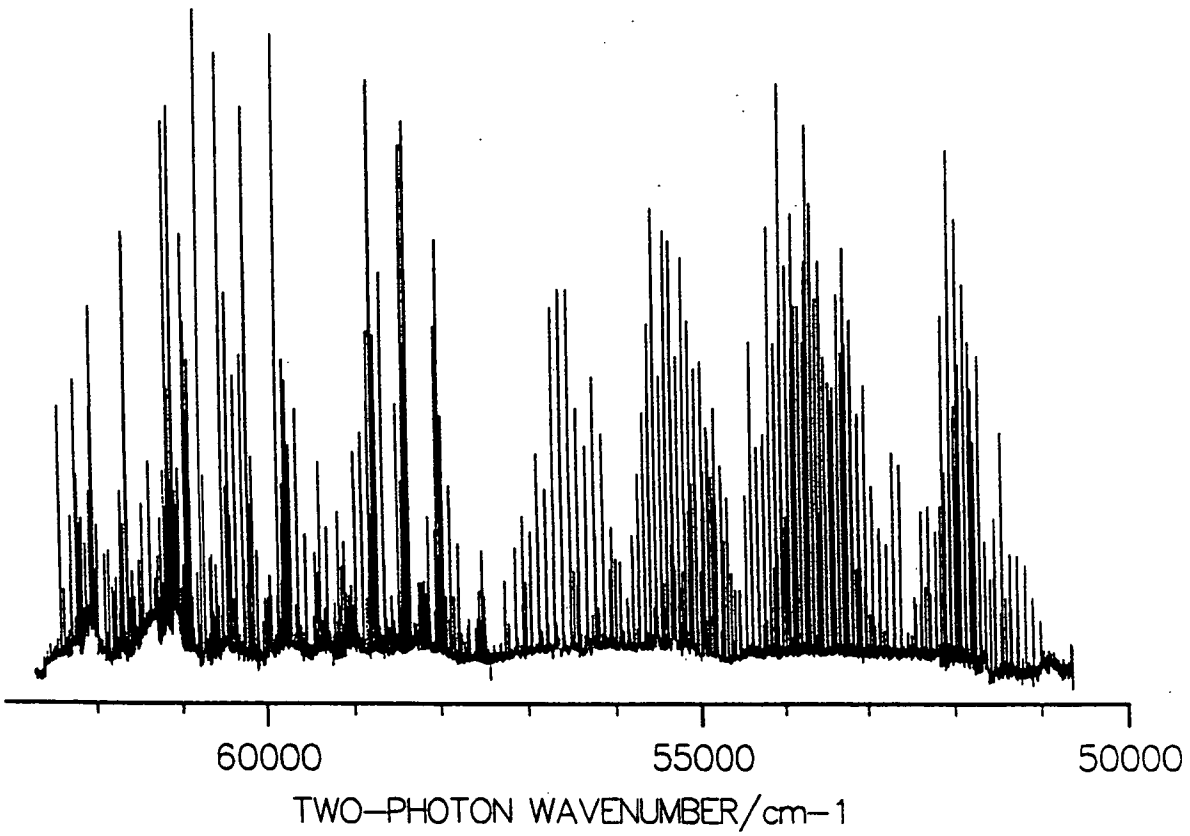

Figure 2.2. DRINCS spectrum of I_2, via $B(v = 14)$ showing the vibrational progressions of the E, f and f' ion-pair states.

2.6.2 Simulation of DRINCS Spectra

Simulation of the DRINCS spectra corresponding to the transition:

$$E, f, f'(0_g^+), v', J' = 0 \leftarrow B(0_u^+), v = 14, J = 0$$

will allow us to determine the FC factor for each transition and hence the position of the intensity minima in the ion-pair vibrational progressions. The number of minima should equal the number of nodes in the B state vibrational wavefunction.

In addition, the simulated positions of these minima are sensitive to the form of the generated upper state potential curves. For example, a lateral shift of only $\sim +0.0015$ Å of the whole E state potential is required to change the intensity minima position from v'=180 to 181. Such simulations help to determine whether a band is absent because of vibronic state coupling or because the FC factor is small. The E, f and f' potential functions generated in the next chapter are used in these simulations together with the well known $B(0_u^+)$ state produced using the RKR turning points of Martin et al. [8].

The simulations were carried out using a constant transition dipole function. The positions of the minima in the FC envelope are very insensitive to $\mu_{12}(R)$ and an unrealistically steeply varying function is required to shift their positions by even ± 1. It can be seen from figure 2.2 that below 56000 cm^{-1} the intensities of the E and f ion-pair states appear to exhibit regular FC envelopes, but that beyond this there is a dramatic change in the regular appearance of the spectrum. An expansion of the region 52000–56000 cm^{-1} is shown in figure 2.4 and the positions of the experimental and simulated vibrational intensity minima are summarised in table 2.6. There is good agreement between the values for both the E and f states. Indeed the correct predictions of the positions of the minima 12 and 13 confirm the E state potential in a region not covered by RKR data.

However, in all three vibrational progressions there are additional missing levels beyond 56,000 cm^{-1} and very irregular band intensities. These result from the homogeneous interaction of these ion-pair states with Rydberg states. The lowest energy 0_g^+ Rydberg state is the $[^2\Pi_{1/2}]6s$ whose first five levels have been observed directly in a 2+1 multiphoton ionisation experiment [9]. This is illustrated in figure 2.3 and can be seen to cross the E state at 55000 cm^{-1}. The resultant interaction is weak as manifested by the unexpectedly low intensities of v'=191, 196, 202 and 207 of the E state which are almost degenerate with v_{Ryd}=7, 8, 9 and 10. The same Rydberg state crosses the f state around 56200 cm^{-1} corresponding to $\sim v_{Ry}$=14. This energy marks the onset of the irregular part of the spectrum, suggesting a stronger interaction between the f and the Rydberg state resulting

in a three-state mixing with the E state as well. Assuming a Morse potential for the Rydberg state, the inner wall of the f' state crosses the $[\frac{1}{2}]_c 6s; \Omega = 0$ state at around 60,000 cm^{-1}. There are gaps of four or five levels in the f' DRINCS spectrum beginning at around 60,500 cm^{-1}, indicating a fairly strong homogeneous interaction with the singlet component of the Rydberg state. The next 0_g^+ Rydberg states are the $[^2\Pi_{3/2}]5d$ group. These have not been observed directly but their origins can be predicted to lie around 59000 cm^{-1} ± 1000 cm^{-1} and one such state is included in figure 2.3. The E and f states are predicted to cross the $5d$ manifold at around 60,000 cm^{-1}, close to the potential minima of the Rydberg states with consequently more favourable FC factors for ion-pair/Rydberg vibronic interaction. New perturbations in the ion-pair vibrational progressions are indeed observed here, but a detailed study of this region will not be attempted.

minima	E state		f state		f' state	
count	obs. v'	calc. v'	obs. v'	calc. v'	obs. v'	calc. v'
1		6		3	19–21	20
2		13		7	30–31	30
3		19		12	40–42	40
4		27		18	51	50
5	35†	35		24		61
6	43–44†	44		31		72
7	55†	55		39		84
8		68	48	48		98
9		82	58–59	59		113
10		99	71	71		129
11		121	86–87	86		150
12	147–148	148	105	105		·
13	181–184	182	·	127		·
14	·	229	·	157		·

Table 2.6. Observed and simulated DRINCS intensity minima for the E, f and f' states of I_2 from v_B=14. † additional data not discussed here.

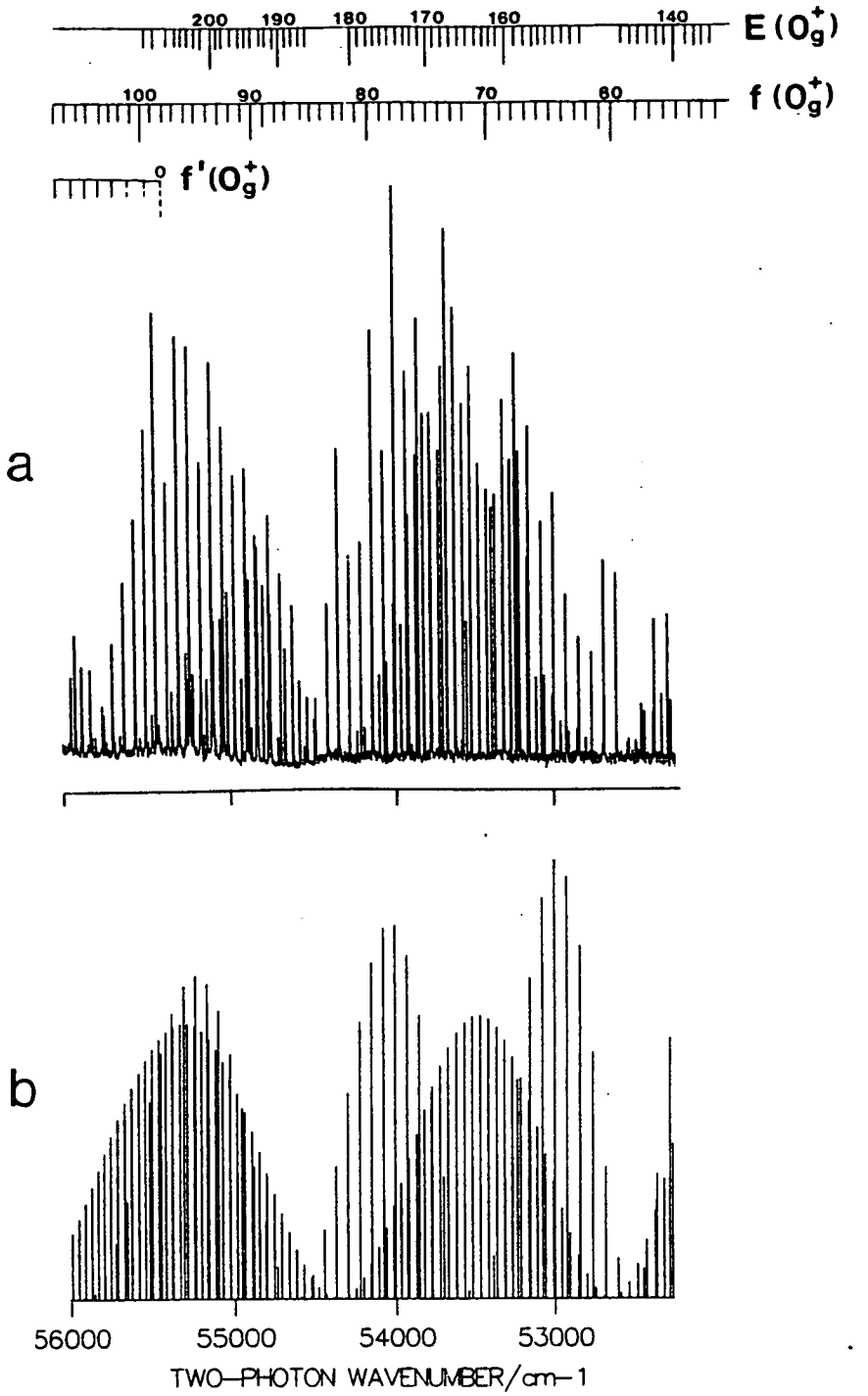

Figure 2.4. (a) An expanded portion of the DRINCS spectrum between 52000–56000 cm^{-1}, (b) the calculated Franck-Condon envelopes of the E and f ion-pair progressions. A comparison shows the rapid fall-off in the observed E-state signal above $\sim$ 55,000 cm^{-1} and the agreement in the positions of the minima in envelopes of the E and f progressions.

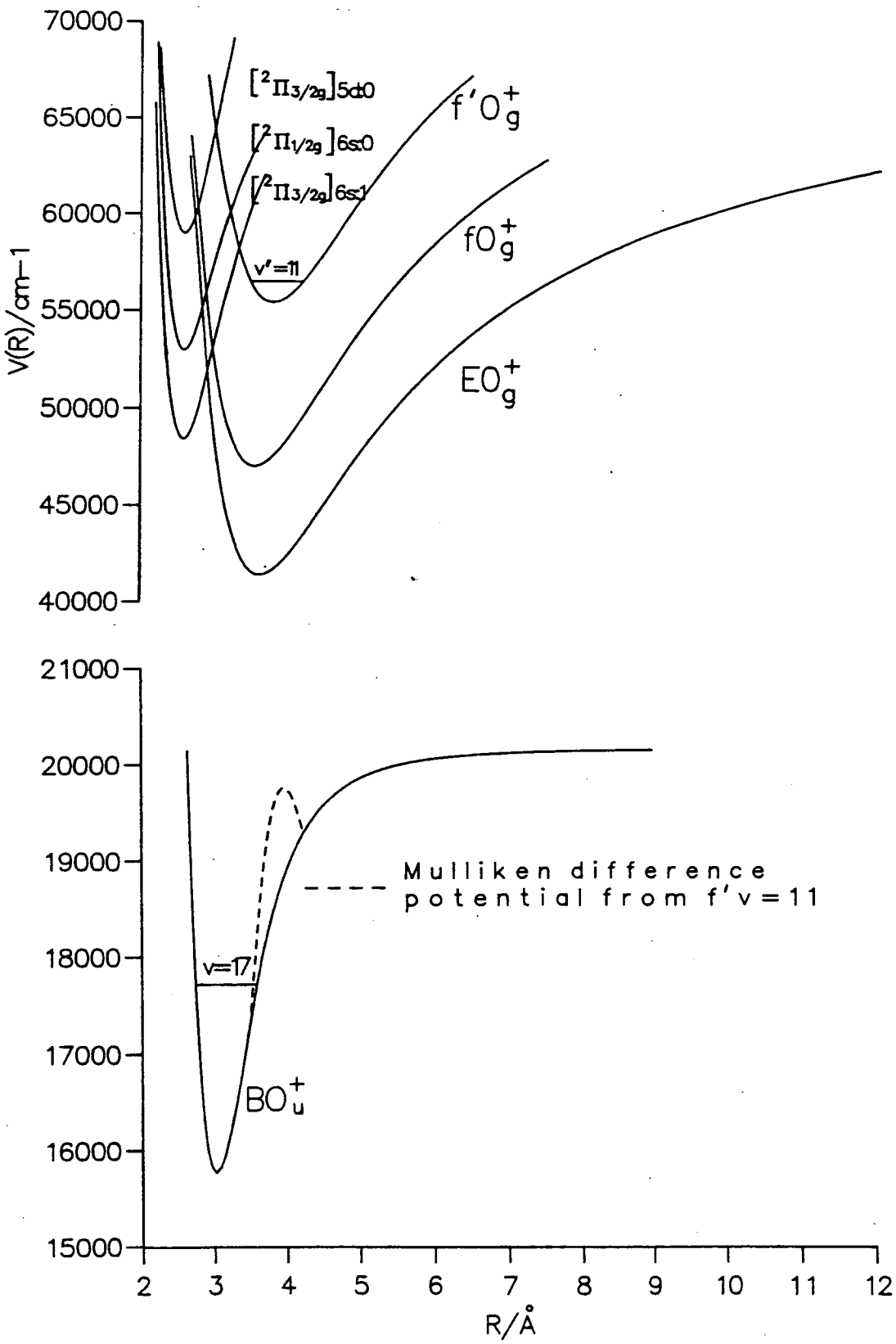

Figure 2.3. The extended potential energy curves of the E, f and f' ion-pair states and some of the lowest energy $[^2\Pi_g]$ Rydberg states and the valence B state.

2.6.3 Simulation of Dispersed Fluorescence

Simulation of the dispersed fluorescence for the transition

$$f'(0_g^+), v' = 11, 70 \xrightarrow{R} B(0_u^+), v, J = 69, 71$$

which enables us to determine the shape of the electronic transition dipole function, $\mu_{f' \rightarrow B}(R)$, over the range of R spanned by the vibrational amplitude of the v'=11 level. In general, the form of $\mu_{f' \rightarrow B}(R)$ determines the relative intensity of the red and blue extrema and modifies the relative peak intensities of the fluorescence when two interfering branches of the difference potential are operative.

The spectroscopic constants of Ishiwata et al. [7], valid up to v'=20 were used to generate the RKR potential for the $f'(0_g^+)$ state. The minimum and maximum turning points for the v'=11 level ($G_{v'}$=56501.4 cm^{-1}) are 3.508 and 4.231 Å respectively. The B state was constructed as in the DRINCS simulations using the RKR points of Martin et al. [8], valid up to v=75, within 0.2% of D_e. The inner repulsive branch was extended using knot points described in a previous paper by Holmes et al. [3].

The simulation program incorporates a combined monochromator/PM tube correction in the form of a polynomial approximation, $F(\nu)$. The corrected fluorescence $S(\nu)$ is related to the Einstein A coefficient by

$$S(\nu) = F(\nu)\nu^3 A(\nu) \tag{2.1}$$

The bound-bound f'(v'=11) $\longrightarrow$ B fluorescence between 254–275 nm is shown in figure 2.5a. The spectrum, which is entirely bound $\longrightarrow$ bound shows both high and low frequency modulation of the envelope, typical of fluorescence in a frequency domain where the Mulliken difference potential exhibits a maximum [10].

A simulation of the $f' \longrightarrow$ B dispersed fluorescence with a constant transition dipole function is shown in figure 2.5b. A comparison between this and the observed fluorescence shows that they are very similar and differ only in their relative

intensities at the red and blue extrema of the spectrum where the intensity ratio I_{red}/I_{blue} in the simulation is too low. By varying the gradient of a simple linear μ_{12} increasing towards larger R, the correct intensity ratio (I_{red}/I_{blue}) is achieved but the relative peak intensities in the interference region between 268–275 nm are incorrect. The optimised μ_{12} is shown in figure 2.6 and displays a maximum at 4.05 Å (c.f $R_e^{f\prime}$=3.8250 Å). The resulting simulated fluorescence spectrum is shown in figure 2.5c. The decrease of μ_{12} to smaller R is clear.

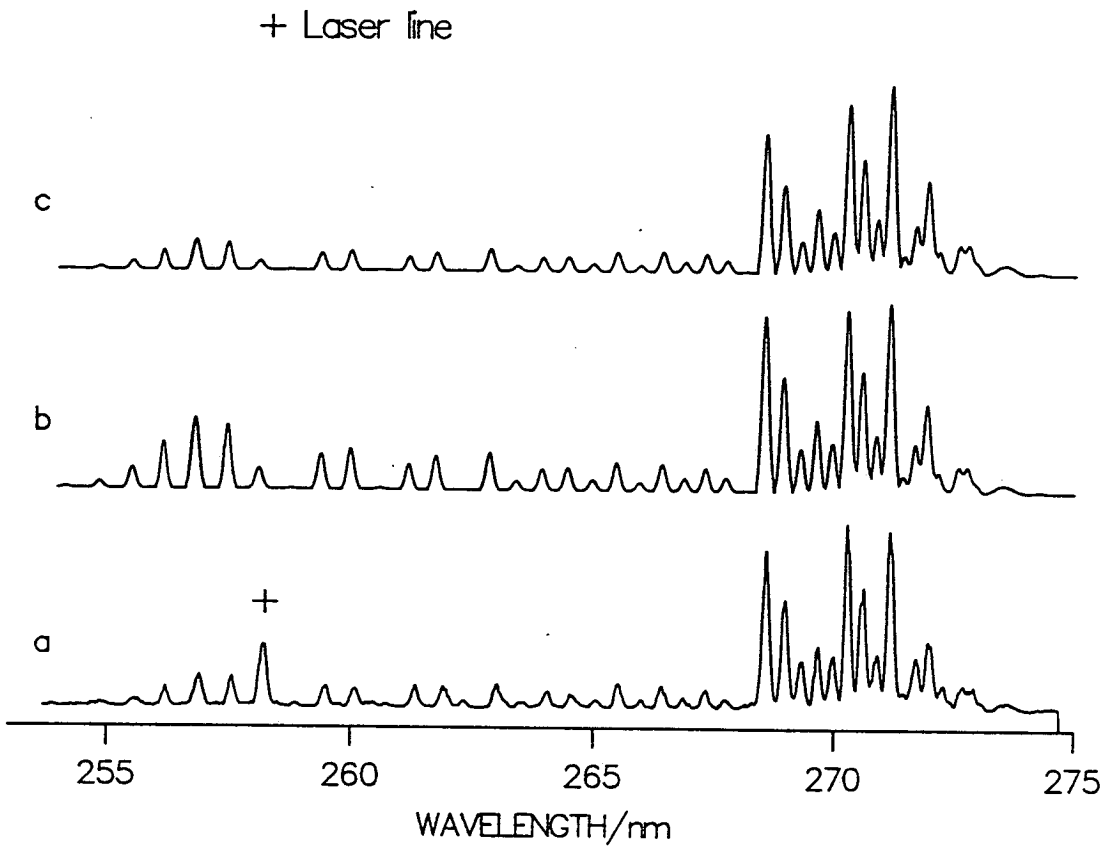

Figure 2.5. The observed dispersed fluorescence spectrum (a) for the $f'(0_g^+)$ $(v' = 11, J' = 70) \longrightarrow B(0_u^+)$ transition with quantum simulations using a constant μ_{12} (b) and the optimised μ_{12} (c).

2.6.4 Lifetime of $f'(0_g^+)$, v'=0 and the Absolute Transition Dipole for $f' \longrightarrow B$

Radiative lifetime measurements of the $f'(0_g^+)$ state were determined over a small range of experimental pressures (0.02–0.04 Torr) by monitoring the time decay of fluorescence for the transition, $f'(0_g^+)$, $v' = 0 \longrightarrow B(0_u^+)$. There was no significant variation in the lifetimes recorded in this pressure range.

The complete fluorescence signal was simulated by convoluting the excitation pulse, $P(t)$, with a single exponential decay to give a best-fit lifetime, τ:

$$I_{fl}^{conv}(t) = A\int P(t')exp(t'-t)/\tau \; dt' \tag{2.2}$$

where t is the pulse arrival time and A the pre-exponential factor.

An initial estimate of the lifetime was obtained either by the method of moments [11], or by a simple fit of the exponential tail of the fluorescence signal after the excitation pulse is over. A steepest-descent parameter search is employed to minimise the standard deviation between simulation and signal. The lifetimes determined in this way showed little dependence on either the initial τ estimate used to start the fitting or the number of lifetimes included in the fit. Our final estimate of τ is 142± 6ns, with the data over 3 lifetimes included.**(see appendix B).**

The dispersed fluorescence simulation gives $\mu_{f'\rightarrow B}(R)$,only to within an arbitrary scaling factor. In order to determine the absolute μ_{12} we need to know the Einstein A coefficient measured for the $f'(v'$=11) vibronic level. This requires the measurements of the radiative lifetime and the relative intensity of fluorescence in each decay channel,

$$\tau_{f'v'} = 1/\sum_{n''v''} A_{f'v'n''v''}, \tag{2.3}$$

$$\sum_{v''} A_{f'v'-Bv''} = (64\pi^4/3hc^3)\sum_{v''} \langle v'|\mu_{f'-B}(R)|v''\rangle^2 \cdot \nu^3_{f'v'Bv''}, \tag{2.4}$$

where n and v are the electronic and vibrational states respectively.

Dispersed fluorescence studies in this spectral region show that fluorescence is

R/Å	$\mu(R)_{f'\rightarrow B}$/D
3.4	0.396
3.5	0.426
3.6	0.495
3.7	0.595
3.8	0.661
3.9	0.690
4.0	0.697
4.1	0.668
4.2	0.606
4.3	0.551
4.4	0.503

Table 2.7. The knot points used to generate $\mu(R)_{f'\rightarrow B}$ between 3.51–4.23 Å.

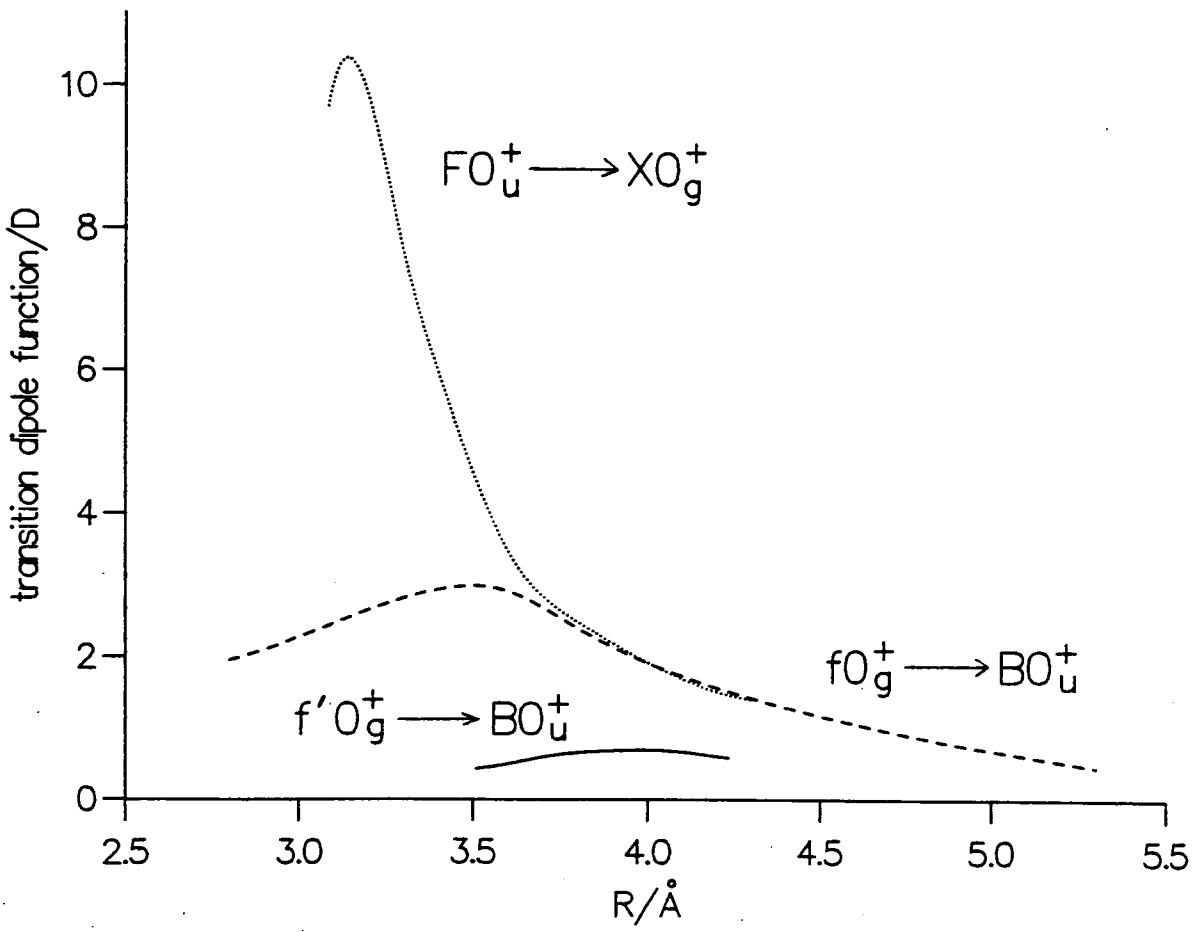

Figure 2.6. The $F(0_u^+)\longrightarrow X(0_g^+)$, $f(0_g^+)\longrightarrow B(0_u^+)$ and $f'(0_g^+)\longrightarrow B(0_u^+)$ dipole functions.

partitioned between the $B(0_u^+)$ and $A(1_u)$ states in the ratio 0.98:0.02. The vibrationally averaged transition dipole at $R_e^{f'}$ is 0.672 D. The absolute transition dipole function generated from the knot points in table 2.7 is shown in figure 2.6.

2.7 Discussion

Three aspects of the spectroscopy of I_2 that have emerged from the experimental results will be discussed; the very long lifetime of the f' state, the form of the transition dipole function $\mu_{f'\rightarrow B}(R)$, the different extent of vibronic coupling of the E and f states to the Rydberg 6s states. All are consequences of the electronic structure of the states involved and are of interest in that they illustrate once again the changing configuration of ion-pair states in passing from small R to 10 Å and beyond. At separations around R_e of the ground state, a single Mulliken configuration [12] $\sigma_g^l\pi_u^m\pi_g^n\sigma_u^p$ for each state is generally assumed to be dominant. These are; $E[2242]^3\Sigma_g$, $f[1432]^3\Pi_{0_g^+}$ and $f'[2242]^1\Sigma_g$. The B state, to a good approximation, retains the configuration $[2431]^3\Pi_{0_u^+}$ over a wide range of R, with a small admixture of the ion-pair configuration $[1441]^1\Sigma_u$ at small separations and an increasing component $[1342]^3\Pi_{0_u^+}$ as $R \rightarrow \infty$ that is needed to dissociate correctly to atoms. It is important to remember that the B state is the only 0_u^+ valence state, and therefore any configurations that the [2431] configuration mixes with must be ion-pair ones in Mulliken's classification. The 6s Rydberg state of 0_g^+ symmetry is $[[2430];^2\Pi_{1/2}]6s$ near its equilibrium separation and so is a relatively pure $^3\Pi_0$ state.

However, these single configurations cannot be the whole picture of the electronic structure, even in the restricted range of separations between 2.8 Å and 4.5 Å. If they were, only the $f(0_g^+)^3\Pi_g$ state could fluoresce to the B state, whereas strong $E \rightarrow B$ fluorescence and weak $f' \rightarrow B$ fluorescence is also seen. Furthermore, only the f state could strongly interact with the 0_g^+ Rydberg state by a

simple two-electron transposition, whereas the E state vibrational levels that are in near resonance with Rydberg vibrational levels are found to be predissociated through vibronic coupling. A more complete description comes from considering the evolution of the single ion-pair configurations from the separated ion description valid at large R, where the three 0_g^+ states are

$$\begin{aligned} E &= \sqrt{2}[2242]^3\Sigma_g^- + [1432]^3\Pi_g \\ f &= [2242]^3\Sigma_g^- - \sqrt{2}[1432]^3\Pi_g \\ f' &= [2242]^1\Sigma_g^+ + \sqrt{2}[0442]^1\Sigma_g^+ \\ 0_g^+(^1S_0) &= \sqrt{2}[2242]^1\Sigma_g^+ - [0442]^1\Sigma_g^+, \quad \text{(undiscovered } 4^{th} \text{ tier state)} \end{aligned}$$

using Russell-Saunders coupling for the p^4 configuration of I^+ and omitting the complementary valence configurations necessary for proper dissociation. As R decreases from around R_e of the ion-pair state, the triplet [2242] and [1432] configurations progressively separate out, as do the singlet [2242] and [0442], forced by the divergence of σ and π orbital energies that are degenerate at large R. It is clear from the observation of weak vibronic coupling between the E and $[1/2]6s, \Omega = 0$ states that there is still some residual [1432] configuration present, but that this configuration belongs dominantly to the f state at around $R \approx 3$ Å . The f state is indeed strongly mixed with the Rydberg state when their potentials cross at this separation, E $\approx$ 56,000 cm^{-1}, see figure 2.3 and the f state vibrational progression stops at this energy. However, the admixture of some $[0442]^1\Sigma_g$ character into the f' state does not open a dipole allowed path to the B state and one more factor must be taken into account when discussing the lifetime of this state.

2.7.1 The Lifetime of the $f'(0_g^+)$ state

The lifetime of the $f'(0_g^+)$ state, 142 ns, contrasts sharply with those of the other ion-pair states, which range between 4 ns and 40 ns. Furthermore, the transition dipole function decreases when $R < 3.8$ Å, in a region where other $i.p. \rightarrow$ valence transition dipoles are still rising. We have already pointed out that with

either the single Mulliken configuration $[2242]^1\Sigma_g$, or with the mixed configuration describing the $^1D_2 \otimes {}^1S_0$ Russell-Saunders product ion state at $R \sim R_e$, the transition to the purely triplet B state remains completely dipole forbidden and a much longer lifetime than that oberved would be expected. The clue lies in the detailed structure of the $^1D_2$ state of I^+. The strength of the transition dipole $\langle f'0_g^+|\mu_z|B0_u^+\rangle$ will be given by the projection of the C-T part of the state vectors $|J^+M_J^+\rangle|J^-M_J^-\rangle$ on to the orthogonal valence state eigenfunctions $|JM_J\rangle|J'M_{J'}\rangle$, determined by the occupancy of the p_σ and p_π orbitals in the two states.

The $I^+(^1D_{2,0})$ RS state can be written as a linear combination of $\|\ldots M_l M_s \ldots\|p^4$ microstates:

$$|0_g^+\rangle_{RS} = (1/2)\{|^1D_{2,0}\rangle_A|^1S_{0,0}\rangle_B \pm |^1S_{0.0}\rangle_A|^1D_{2,0}\rangle_B\} \tag{2.5}$$

The cationic configuration is

$$|^1D_{20}\rangle_{RS} = (1/\sqrt{6})[\|1^-0^+0^-\underline{1}^+\| - \|1^+0^+0^-\underline{1}^-\| + 2\|1^+1^-\underline{1}^+\underline{1}^-\|] \tag{2.6}$$

and the anionic is

$$|^1S_{00}\rangle_{RS} = \|1^+1^-0^+0^-\underline{1}^+\underline{1}^-\| \tag{2.7}$$

The $B0_u^+$ state which is the single valence configuration 2431 $^3\Pi_{0_u^+}$ can be described in a similar manner using a linear combination of $J_A J_B$ wavefunctions:

$$|0_u^+\rangle_{RS} = 1/2\{|3/2,1/2\rangle_A|1/2,-1/2\rangle_B + |1/2,-1/2\rangle_A|3/2,1/2\rangle_B$$

$$+ |3/2,-1/2\rangle_A|1/2,1/2\rangle_B + |1/2,1/2\rangle_A|3/2,-1/2\rangle_B\} \tag{2.8}$$

where the p^5 microstates [13] are given by:

$$|3/2,1/2\rangle = 1/\sqrt{3}[\|1^+1^-0^+0^-\underline{1}^-\| - \sqrt{2}\|1^+1^-0^+1^+\underline{1}^-\|] \tag{2.9}$$

$$|1/2,-1/2\rangle = 1/\sqrt{3}[\sqrt{2}\|1^+0^+0^-\underline{1}^+\underline{1}^-\| + \|1^+1^-0^-\underline{1}^+\underline{1}^-\|] \tag{2.10}$$

$$|3/2,-1/2\rangle = 1/\sqrt{3}[\sqrt{2}\|1^+0^+0^-\underline{1}^+\underline{1}^-\| - \sqrt{2}\|1^+1^-0^-\underline{1}^+\underline{1}^-\| \quad (2.11)$$

$$|1/2,1/2\rangle = 1/\sqrt{3}[\sqrt{2}\|1^+1^-0^+0^-\underline{1}^-\| + \|1^+1^-0^+\underline{1}^+\underline{1}^-\|] \quad (2.12)$$

The $\|1^+1^-0^+\underline{1}^+\underline{1}^-\| \cdot \|1^+1^-0^-1^+\underline{1}^-\|$ product microstates on the top line of the atom-pair (a.p) wavefunction in equation 2.9 can be generated by applying a parallel electron transfer of either the 0^+ or 0^- electron from the p^6 anion microstate to the $\|1^+1^-\underline{1}^+\underline{1}^-\|$ p^4 microstate of the i.p wavefunction in equation 2.7. A similar procedure produces the corresponding p^5 product a.p microstates on the bottom line of equation 2.9 but with opposite phase to those of the top line and hence the sum of these one-electron transitions exactly cancel to zero.

The $\|1^+1^-0^+0^-\underline{1}^-\| \cdot \|1^+0^+0^-\underline{1}^+\underline{1}^-\|$ product microstates on the top line of equation 2.9 are formed from the transfer of a $\underline{1}^+$ electron on the anion to the $\|1^+0^+0^-\underline{1}^-\|$ p^4 microstate in equation 2.7. Once again, the corresponding p^5 microstates on the bottom line of the a.p wavefunction are formed with opposite phase resulting in the sum of these one-electron shifts exactly cancelling to zero.

The $\|1^-0^+0^-\underline{1}^+\|$ p^4 microstate in equation 2.7 cannot form any of the p^5 a.p microstates via a single electron transfer from the p^6 microstate. Overall the $\langle {}^1D_{20}|\mu_z|B0_u^+\rangle$ transition dipole is exactly zero, as indeed would be expected from a singlet↔triplet transition. The reason why fluorescence is observed experimentally is because we have thus far neglected the effect of spin-orbit coupling in the RS description, where the off-diagonal elements of the spin-orbit operator, $\hat{H}_{SO}$, mix in other RS states with the same J value. Within the free I^+ ion, partial jj coupling results between the ${}^3P_2$ and ${}^1D_2$ states given by, $\langle\|1^+1^-0^+\underline{1}^+\|\,|\hat{H}_{SO}|\,\|1^+1^-0^+0^-\|\rangle$, with the ladder operators l_-s_+ acting on the $\|0^-\|$ orbital. From the observed term values of I^+ we have estimated [13]

$$|{}^1D_2\rangle_{jj} = 0.312|{}^3P_2\rangle_{RS} + 0.950|{}^1D_2\rangle_{RS}$$

$$|{}^3P_2\rangle_{jj} = 0.950|{}^3P_2\rangle_{RS} - 0.312|{}^1D_2\rangle_{RS}$$

Some $(1432)^3\Pi$ character is thereby introduced into the molecular wave function and the route is open for weak fluorescence to the B state which itself requires

some $^1\Sigma_{0_u^+}$[1441] character at small R. These same I^+ wave functions would predict that the transition dipole for $E \rightarrow B$ should be $\approx 0.950/0.312 \times \mu_{f' \rightarrow B}$, giving a value of 2 D at $R = 3.8$ Å. This is consistent with the value of 3.01 D found for the E state at 3.65 Å [14].

2.7.2 The Form of the $f' \rightarrow B$ Dipole Function

The radial dependence of the $\mu_{f' \rightarrow B}$ function in figure 3.5 passes though a maximum at around 4 Å. All ion-pair $\rightarrow$ valence transition dipole functions are expected to exhibit a maximum, due to the opposing tendencies of any transition dipole to increase linearly with R and the exponential decrease of anion-cation orbital overlap with increasing separation. The early decay of the $f' \rightarrow B$ transition dipole to smaller R can be attributed to the rapid purging of the triplet [1432] character from the wave function around R_e.

2.8 Conclusion

Using the DRINCS technique we have observed transitions to three ion-pair states of 0_g^+ symmetry. Vibrational Dunham coefficients for the E, f, and f' states, each belonging to a different ion-pair tier (correlating with the $^3P_2$, $^3P_0$ and $^1D_2$ states of I^+ respectively), have been extended and now cover the range v'=0–422, v'=0–228 and v'=0–166 respectively.

Using the new E state potential to simulate the DRINCS spectrum, we correctly reproduce the the positions of the observed intensity minima below 56000 cm^{-1} in the Franck-Condon envelope. This turns out to be a sensitive test of the lateral position of the potential energy curve. From these extended potentials it is clear that the repulsive walls of the E and f states appear to be slowly converging as R decreases. Above 56000 cm^{-1} the spectra are complicated by moderately strong homogeneous interactions between the ion-pair states and some Rydberg

states, particularly between the f (0_g^+) and $[^2\Pi_{1/2}]_c$6s Ω=0 states, but this interaction is also shared by the E state. The potential energy curves constructed for the ion-pair states intersect the known Rydberg state potentials at the energies at which interruption of the ion-pair vibrational progression is observed.

The lifetime of the f' state was measured to be 142± 6 ns. Combined with the radial dependence of the transition dipole, $\mu_{f'\rightarrow B}(R)$ needed to fit the dispersed fluorescence from v'=11, the absolute value of $\mu_{f'\rightarrow B}(R)$ at R_e of the f' state was found to be 0.67 D. The long lifetime is essentially due to the fact that the B state is the only 0_u^+ state in the valence manifold and the $f'\rightarrow B$ transition is spin forbidden. Using the separated-ion model of the ion-pair state, this transition only becomes allowed if partial jj coupling introduces some triplet character into the $I^+(^1D_2)$ ion.

2.9 References

1. A. R. Hoy and A. W. Taylor, *J. Mol. Spec.* **126**(1987)484.

2. K. P. Lawley, P. J. Jewsbury, T. Ridley, P. R. R.Langridge-Smith and R. J. Donovan, *Mol. Phys.* **75**(1992)811.

3. A. J. Holmes, K. P. Lawley, T. Ridley, R. J. Donovan and P. R. R. Langridge-Smith, *J. Chem. Soc. Farad. Trans.* **87**(1991)15.

4. P. J. Jewsbury, K. P. Lawley, T. Ridley and R. J. Donovan, *J. Chem. Soc. Farad. Trans.* **88**(1992)1599.

5. R. J. Donovan, T. Ridley, K. P. Lawley and P. J. Wilson, *Chem. Phys. Lett.* **196**(1992)173.

6. J. C. D. Brand, A. R. Hoy, A. K. Kalkar and A. B. Yamashita, *J. Mol. Spec.* **95**(1982)350.

7. T. Ishiwata, J. Yamada and K. Obi, *J. Mol. Spec.* **158**(1993)237.

8. F. Martin, R. Bacis, S. Churassy and J. Vergès, *J. Mol. Spec.* **116**(1986)71.

9. J. C. Miller, *J. Phys. Chem.* **91**(1987)2589.

10. J. Tellinghuisen, *J. Mol. Spec.* **103**(1984)455.

11. *Data Reduction and Error Analysis for Physical Sciences.* ed. P. R. Bevington (McGraw-Hill, 1969.) p245.

12. R. S. Mulliken, *J. Chem. Phys.* **55**(1971)288.

13. P. J. Jewsbury and K. P. Lawley, *Chem. Phys.* **141**(1990)225.

14. J. P. Perrot, B. Femelat, J. L. Subtil, M. Broyer and J. Chevaleyre, *Mol. Phys.* **61**(1987)85.

Chapter 3

The E, f and f' Potential Energy Curves

3.1 Introduction

Accurate diatomic potential energy curves, $V(R)$, extending over a large internuclear separation are extremely important in the understanding of a variety of molecular phenomenon including ionic collisions, radiation transfer, electron-molecule collisions, predissociations and interstate perturbations, etc.

Over the energy range for which reliable rotational and vibrational experimental data is available, $V(R)$ can be readily constructed using the Rydberg-Klein-Rees (RKR) method [1] which is based on the semi-classical quantization condition:

$$\int_{R_-(E)}^{R_+(E)} [E - V_J(R)]^{-\frac{1}{2}} \, dR = (v + \frac{1}{2})\pi \tag{3.1}$$

where $E - V_J(R)$ is the kinetic energy and $R_\pm(E)$ are the classical turning points where the total energy, E, is equal to the potential energy, $V(R)$.

Accurate and efficient RKR programs are widely available and differ mainly in the way they treat the singularity which occurs at the upper limit of integration. The resulting computed RKR potential curve, $V^{RKR}(R)$, differs from the true Born-Oppenheimer potential, $V^{BO}(R)$ by only $\sim$0.1 cm^{-1}.

The RKR method is used to calculate $V(R)$ from a set of unperturbed energy levels, $E_{v,J}$, represented by a simple, rapidly convergent polynomial function of the

rotational and vibrational quantum numbers J and v, in the form of the Dunham expansion:

$$E_{v,J} = \sum_{l,m} Y_{l,m}(v + \frac{1}{2})^l [J(J+1)]^m \tag{3.2}$$

where any isolated perturbed energy levels are removed from the data set.

RKR calculations using higher vibrational levels of a particular electronic state for which no rotational analysis has been performed usually produce unrealistic potential energy curves which at smaller R may either 'double-back' on itself or have a point of inflection due to the inaccuracies in extrapolating B_v values. However, a knowledge of $G(v)$ which is sufficient to determine $R_+(E) - R_-(E)$, coupled with our knowledge of the behaviour of the Coulombic branches of the halogen ion-pair potentials have allowed these states to be generated beyond the previously existing RKR potentials.

As discused in the previous chapter, these potentials have been used to simulate the DRINCS spectra and correctly reproduce the observed intensity minima in the envelope of the vibrational progression below 56,000 cm^{-1}. Above this, the band intensities are very irregular because of homogeneous interactions with Rydberg states.

In general, only the lowest lying vibrational levels of the halogen and interhalogen Rydberg states are significantly unpredissociated. As a consequence, insufficient spectroscopic information is available to generate accurate potential energy curves of these states beyond the region around their minima using numerical calculations such as the RKR method. However, these perturbations in the DRINCS spectra discussed in the previous chapter arising from Rydberg/ion-pair interactions have been qualitatively explained by adopting a Morse potential [2], $V^{Morse}(R)$, for the Rydberg states which displays the qualitative features of the real potential, $V^{BO}(R)$, especially around its minimum and are more realistic than harmonic potentials, $V^{harmonic}(R)$, especially at dissociation and small R. From equation 3.3 it can be seen that in order to construct V^{Morse} three independent constants must be determined, R_e, ω_e and D_e, where the latter can be calculated

from a knowledge of the ground and excited atomic state dissociation limits and T_e^{Ryd} (or from the relationship, $D_e = \omega_e^2/4\omega_e x_e$).

$$V^{Morse}(R)/hc = D_e\{1 - exp[-\beta(R - R_e)]\}^2 \ cm^{-1} \tag{3.3}$$

where

$$\beta = (8\pi^2 c\mu\omega_e x_e/h)^{\frac{1}{2}} = 2.435576 \times 10^{-1}(\mu\omega_e x_e)^{\frac{1}{2}} \ \mathring{A}^{-1} \tag{3.4}$$

or

$$\beta = (2\pi^2 c\mu\omega_e^2/D_e h)^{\frac{1}{2}} = 1.2177881 \times 10^{-1}(\mu\omega_e^2/D_e)^{\frac{1}{2}} \ \mathring{A}^{-1} \tag{3.5}$$

In general, deficiencies in the form of $V^{Morse}(R)$ at both small and large R can occur. At small R, the repulsive limb usually does not rise steeply enough which can be overcome by the addition of a short-range AR^{-12} term. At large R, although $V^{Morse}(R)$ goes assymptotically to the dissociation limit, its R-dependence is at variance with the required power law interaction of separated atoms [3]. A modified long-range tail of the form $D_e - C_n R^n$ which correctly models interactions between neutral atoms can be generated in a simlar way to the attractive limbs of the ion-pair states described in the next section. These additions on to $V^{Morse}(R)$ must be such that dV/dR and higher derivatives remain continuous and is best achieved using splining techniques.

3.2 Generation of the E, f and f' Potential Energy Curves

Brand et al. [4] and Ishiwata et al. [5] have generated vibrational and rotational Dunham coefficients for the E, f and f' states to calculate RKR turning points valid up to v'=95, 101 and 20 respectively. In RKR theory, using Y_{n0} only, the relative distance between the inner and outer turning points at each $G_{v'}$ energy is known, but not their absolute positions which are determined by the Y_{nm} rotational constants. Since ion-pair states of I_2 correlate with the atomic ions $I^-(^1S)$ +

$I^+(^3P,^1D,^1S)$, their outer-branch potentials are essentially Coulombic and have been successfully modelled [6] at large R using truncated Rittner functions valid for $R \geq 6.0$ Å, of the form:

$$V(R) = T_\infty - C_1/R \pm C_3/R^3 - C_4/R^4 - C_6/R^6 \tag{3.6}$$

The sign of the C_3 coefficient depends on the electronic configuration of the p^4 cationic microstate being considered in the charge-quadrupole interaction. The C_3 term is generally negative when p_π occupancy is greater than p_σ. The ion-pair dissociation limit, T_∞, was determined relative to the potential minimum of the ground state using the atomic excitation scheme, $I(^2P_{\frac{3}{2}})+I(^2P_{\frac{3}{2}}) \longrightarrow I^-(^1S)+I^+$ $(^3P,^1D,^1S)$. An accurate value for the electron affinity of atomic iodine has been determined as 24673 ±3 cm^{-1} [7]. The ionisation limits of the Rydberg series of atomic iodine which converge on $I^+(^3P_2, ^3P_1$ and $^3P_0)$ are known to be 84295.1, 91382.1 and 90743.0 ($\pm 0.3 cm^{-1}$) respectively [8] and the $^1D_2$ ionisation limit is 85900.2 cm^{-1} [9]. The ground state dissociation energy is 12547.2 cm^{-1}. Table 3.1 summarises the Rittner coefficients used for the E, f and f' states in the current studies. Using these it should be possible to locate the absolute positions of the turning points of these states beyond energies where valid rotational data is available by shifting the purely vibrational RKR turning points on to these well defined attractive ion-pair branches.

3.2.1 The E State

Anticipating our results, the extended E state potential shown in figure 2.3 supports vibrational levels at $v' \sim 400$ with very large vibrational amplitudes (~10 Å) at 62000 cm^{-1}, a characteristic of such ion-pair states. The uncertainty in the C_4 term given in table 3.1 comes from the uncertainty of the polarisability of I^+, 2 $Å^3 \leq \alpha_{I^+} \leq 4$ $Å^3$. The actual lateral displacement between these two possible

attractive branches is only ~0.008 Å at 62000 cm^{-1}, or a vertical energy displacement of ~8 cm^{-1} at 11 Å. The contributions to the energy of the attractive branch from the C_3, C_4 and C_6 coefficients are 32, –46 and –0.5 cm^{-1} respectively at R=11 Å. The ratio of the gradient of the repulsive branch of the potential at this energy to that of the attractive branch is ~ –32. Any lateral shift in the shallow attractive branches at high v' must be matched by an equivalent shift in the repulsive branch in order to conserve the correct distance between turning points for that energy, but the latter shift results in a much larger vertical displacement of $V(R)$ because of the large difference in gradients. In fact, this provides a constraint on the values of C_3, C_4 and C_6, which must not allow the inner branch of the potential to "fall over", i.e cause $V(R)$ to become double valued at small R. This same effect is often noticed in a full RKR analysis if rotational Dunham coefficients are used beyond the range of v' from which they were derived. The final constraint is that both branches of $V(R)$ must smoothly join on to the lower RKR points obtained with rotational data.

The vibrational constants up to v'=422 produced from these DRINCS studies were combined with the rotational constants of Brand et al. [4], valid up to v'=95 only ($G_{v'}$=49422.3 cm^{-1}) to produce RKR turning points. Beyond 6.0 Å the outer turning points were shifted onto the calculated attractive branch whilst conserving the RKR R_{min}–R_{max} distance at each vibrational level. However, the shifted inner turning points do not join smoothly on to the lower RKR points because they are shifted to lower than expected R values, resulting in a discontinuity when splined to the valid RKR potential of Brand et al.[4]. Hence, a small lateral displacement of the attractive branch towards larger R of ~0.07 Å at v'=180 decreasing gradually to a zero shift at v'=422, is required in order to smoothly spline with the turning points of Brand. The purely vibrational RKR turning points are then moved onto this reconstructed outer branch, resulting in correctly shifted inner turning points. This change cannot quite be accommodated by a permissible change in C_3 or C_6 and probably indicates an exponentially decaying anion-cation overlap term in $V(R)$. The final curve generated by splining these points together with Brand's

RKR potential valid up to v'=95 reproduce the experimental eigenvalues to within ± 1 cm^{-1}. Finally, although we have constrained the final potential such that both branches of $V(R)$ smoothly join onto the lower RKR points, this potential does not represent a unique fit for the E state. In reality, the repulsive branch of the E state may well have a slight inflection, perhaps as a result of an avoided crossing with the f state (see section 3.3), but only a full RKR analysis will determine this. Therefore, although vibrational RKR data accurately determines the R_{min}–R_{max} distance, the absolute positions of these branches remains less constrained.

3.2.2 The f State

A similar procedure was employed for the f state potential where the rotational constants of Ishiwata [5] are valid only up to v'=101, some 7000 cm^{-1} below the v'=228 level at the limit of our data. The resulting RKR R_{max} points beyond 6.0 Å were shifted to smaller R on to the calculated attractive branch produced using the same C_4 and C_6 values used for the E state. At R=6 Å , the contributions from the C_3, C_4 and C_6 coefficients to the attractive limb energy are 0, –519 and –21 cm^{-1} respectively. Once again, the second constraint was the continuity of the shifted inner branch of the potential with the full RKR curve. A lateral displacement of the attractive branch towards larger R of ~0.06 Å at v'=130 and decreasing gradually to a zero shift at v'=228, is required in order to smoothly spline with the turning points of Ishiwata before shifting the purely vibrational RKR turning points on to it, resulting in correctly shifted inner turning points. The final curve shown in figure 2.3 was produced by splining between the two sets of data points.

3.2.3 The f' State

The rotational constants of Ishiwata, valid up to v'=20 of the f' state, were used to extend the RKR curve up to v'=166. The generated R_{max} points followed the

attractive branch very closely and hence no shift was required. The knot points for these extended potentials are shown in table 3.2 and plotted in figure 2.3.

State	I^+ config.	T_∞ (cm^{-1})	$C_1^{(a)}$ (cm^{-1})	$C_3^{(b)}$ (cm^{-1})	$C_4^{(a,c)}$ (cm^{-1})	$C_6^{(a)}$ (cm^{-1})
E	$^3P_{20}$	72169	1.16141×10^5	$+4.34\times10^4$	6.74 to 5.57×10^5	10^6[9]
f	$^3P_{00}$	78617	"	0	"	"
f'	$^1D_{20}$	85900	"	-8.69×10^4	"	"

Table 3.1. Rittner coefficients used to generate the attractive limbs of the E, f and f' ion-pair states of I_2.

(a) The C_1, C_4 and C_6 coefficients corresponding to charge-charge, charge-polarisation and induced dipole-induced dipole interactions respectively, are assumed to have the same values for the three ion-pair states.

(b) $\langle r^2\rangle_+$=1.87 Å^2.

(c) The uncertainty in C_4 reflects the two limits between which the polarisability of I^+ is known. A reasonable estimate would be 2 Å^3 $\leq \alpha_{I^+} \leq$ 4 Å^3. An accurate value of α_{I^-} is known to be 7.6 Å^3 [9].

E state				f state		f' state	
R/Å	V/cm^{-1}	R/Å	V/cm^{-1}	R/Å	V/cm^{-1}	R/Å	V/cm^{-1}
2.654	63000.0	5.868	51629.8	2.670	64050.0	2.871	68409.9
2.674	62000.0	6.020	52201.0	2.690	63343.7	2.887	67909.9
2.699	61239.8	6.173	52748.0	2.700	63000.0	2.900	67543.9
2.710	60725.0	6.328	53272.1	2.730	61931.5	2.911	67200.6
2.750	59000.0	6.483	53774.2	2.750	61200.0	2.920	66921.3
2.800	56850.0	6.644	54255.6	2.780	60182.2	2.941	66282.9
2.852	54717.3	6.805	54717.3	2.800	59500.0	2.975	65304.4
2.863	54255.6	7.095	55495.0	2.830	58392.7	2.988	64949.4
2.875	53774.2	7.301	55992.8	2.850	57650.0	3.016	64218.7
2.887	53272.1	7.641	56762.6	2.880	56605.4	3.064	63062.7
2.900	52748.0	7.990	57475.7	2.900	55929.9	3.082	62657.2
2.914	52201.0	8.346	58134.1	2.930	54913.0	3.121	61825.7
2.929	51629.8	8.711	58747.1	2.950	54279.9	3.143	61383.3
2.945	51033.2	9.084	59318.1	3.000	52863.2	3.191	60481.0
2.960	50395.4	9.470	59850.5	3.050	51655.8	3.284	58965.8
2.979	49748.4	9.857	60348.5	3.100	50632.5	3.361	57934.9
3.000	49068.4	10.252	60815.8	3.200	49061.2	3.407	57412.5
3.023	48369.4	11.000	61597.0	3.300	48016.4	3.534	56314.7
3.049	47634.1	11.500	62059.6	3.400	47388.1	3.641	55748.6
3.079	46855.4	12.000	62483.1	3.500	47085.4	3.825	55409.9
3.114	46036.0			3.570	47026.3	4.035	55746.1
3.154	45209.3			3.600	47033.1	4.189	56313.3
3.204	44326.1			3.700	47171.2	4.308	56868.6
3.268	43412.1			3.800	47452.9	4.600	58455.6
3.361	42451.4			3.900	47840.6	4.773	59450.1
3.577	41463.0			4.000	48304.4	4.940	60402.9
3.647	41411.7			4.250	49660.4	5.103	61306.8
3.722	41462.0			4.500	51126.0	5.266	62174.2
4.036	42455.7			4.750	52578.5	5.592	63779.6
4.227	43405.2			5.000	53958.6	5.758	64526.7
4.394	44323.2			5.250	55240.9	5.927	65238.1
4.549	45201.2			5.500	56424.8	6.101	65918.5
4.698	46043.2			5.750	57516.7	6.280	66563.8
4.844	46851.4			6.000	58508.9	6.372	66873.9
4.989	47628.6			6.250	59415.8	6.481	67222.6
5.133	48370.1			6.500	60249.5	6.600	67580.0
5.277	49078.8			6.750	61013.3		
5.422	49758.2			7.000	61710.8		
5.569	50412.1			7.250	62346.5		
5.719	51033.2			7.500	62913.1		

Table 3.2. The knot points used to generate the extended E, f and f' state potential curves.

3.3 An Apparent Avoided crossing Between the E and f States

Judging from the potential energy curves in figure 2.3, the inner walls of the E and f states appear to be converging. The difference in their T_e values at around 3.6 Å is 5600 cm^{-1}, and this separation has decreased to $\approx$ 2700 cm^{-1} at 2.8 Å. Since both are 0_g^+ states, a crossing will be avoided but, it would seem, not strongly. Around R_e, the $E(^3P_2)$ state separated ion-pair configuration is richer in the apparently lower $[2242]^3\Sigma_g$ MO configuration and one might expect their energies to diverge at smaller separations. However, as R decreases, the overlap of the p_π orbitals on the two atoms continues to increase, leading to continued lowering of energy of the π_u orbitals (and raising of the π_g orbitals). The p_σ overlap, however, passes through a maximum and the molecular $p\sigma_g$ orbital then starts to rise in energy. Remembering that the Mulliken confiurations are $E[2242]$ and $f[1432]$, the latter configuration will eventually become the lower in energy as R decreases. We suggest that the near convergence of the E and f state potential walls represents the region in which the E state is beginning to acquire back more of the $[1432]^3\Pi_g$ configuration. The repulsion between the two states is not strong because the two configurations are connected in first order only by the $l_{z_i}s_{z_i}$ component of the spin-orbit operator, not by the $1/r_{12}$ Coulombic term of the electronic interaction.

3.4 References

1. R. Rydberg, *Z. Phys.*, **73**(1931)376.

   O. Klein, *Z. Phys.*, **76**(1932)226.

   A. L. G. Rees, *Proc. Phys. Soc. (London)*, **59**(1947)998.

2. P. M. Morse, *Phys. Rev.*, **34**(1929)57.

3. T. Y. Chang, *Rev. Mod. Phys.*, **39**(1967)911.

4. J. C. D. Brand, A. R. Hoy, A. K. Kalkar and A. B. Yamashita, *J. Mol. Spec.* **95**(1982)350.

5. T. Ishiwata, J. Yamada and K. Obi, *J. Mol. Spec.* **158**(1993)237.

6. E. S. Rittner, *J. Chem. Phys.* **19**(1951)1030.

7. H. Hotop and W. C. Lineberger, *J. Phys. Chem. Ref. Data.* **14**(1985)731.

8. V. N. Sarma and Y. N. Joshi, *Can. J. Phys.* **61**(1983)1434.

9. C. E. Moore, *Atomic Energy Levels*, Vol.III, NSRDS-NBS35.

Chapter 4

ICl DRINCS Studies

4.1 Introduction

Prior to the work in this thesis, only five ion-pair states of ICl (compared with thirteen in I_2) had been observed experimentally using both the (2+1) REMPI and OODR methods. The latter technique and in particular DRINCS, provides the best method to observe these higher ion-pair states in congested spectral regions as shown in this chapter.

In a double resonance experiment from the ground state using the $A(^3\Pi_1)$ intermediate state, the first selective excitation of an ion-pair state of ICl, assigned as the $\beta 1$ ($^3P_2$) state, was achieved by Barnes et al. [1] and later confirmed by King et al. [2]. In 1983, using an OODR polarisation-labelling technique, Brand et al. [3] accessed the first tier Ω=0^+ and Ω=1 ion-pair states via parallel ($\Delta\Omega$=0) transitions from the $B0^+$ and $A1$ intermediate states respectively.

A year later, all three first tier ion-pair states, $\beta 1$, $E0^+$ and $D'2$, were characterised up to about v'=30 by Bussieres et al. [4] in a double resonance experiment using only the $A1$ intermediate state. Figure 4.1 shows some of the experimentally determined ion-pair states together with their predicted attractive branches which at large R tend towards the various I^+ ($^3P_{2,1,0}$ and $^1D_2$) dissociation limits. In the abscence of parity symmetry, the halving of the number of states in each ion-pair tier of ICl compared with the homonuclear halogens results in a much smaller spread in the T_e values in each cluster. For example, ΔT_e for the first tier

states of ICl and I_2 are <50 and >1000 cm^{-1} respectively. Consequently, significant heterogeneous coupling of the $\beta 1$ state with the $E0^+$ and $D'2$ states takes place where the experimental values for the electronic-rotational matrix elements, $\langle \Omega \pm 1 | L_\pm + S_\pm | \Omega \rangle$, are 2.38 and 1.86 cm^{-1} respectively [5]. Such perturbations are most easily observed in the $\beta 1$ state rather than in either of the Ω=0 states because in the former case only the *e*-rovibronic substate is perturbed by neighbouring 0^+ levels whilst the f-substate is unaffected and acts as a reference frame for the other. Brand et al. have shown that the strongest transitions from the $A1$ intermediate state are normally to the $\beta 1$ ion-pair state via parallel, $\Delta\Omega$=0 transition. However, these perturbations allow $E0^+ \longleftarrow A1$ and $D'2 \longleftarrow A1$ transitions to occur with parallel selection rules and indeed are stronger than the unseen though formally allowed perpendicular $\Delta\Omega$=1 transitions.

In recent years, a combination of techniques have accessed a wide range of E-state vibrational levels. Lipson et al. [6] observed vibrational levels between v'=246–351 in a jet-cooled, one-photon laser-induced fluorescence excitation experiment. Between λ_{ex}=175–180 nm dips in the spectra are observed due to predissociation resulting from the homogeneous interaction between the the $E0^+$ state and the $[^2\Pi_{1/2}]_c 6s\sigma : 0^+$ Rydberg state. Donovan et al. [7] used both jet-cooled (2+1) REMPI and DRINCS techniques to fill in the missing levels and extend the data to v'=387 where levels beyond v'=350 are displaced as a result of an avoided crossing of the $E0^+$ state with the $[^2\Pi_{3/2}]_c 6p\pi : 0^+$ Rydberg state. In contrast to I_2 and Br_2 where only strong Rydberg transitions are observed in (2+1) REMPI spectra [8, 9], the $E0^+$ ion-pair state dominates the spectra of ICl and IBr [7, 10]. Because there are no parity selection rules in the heteronuclear halogens, the [1441] configuration of the E-state can be accessed in a two-photon transition which is forbidden for the ungerade state of the homonuclear halogens. Of all the ion-pair states, the reason why the $E0^+$ state alone is observed is less straightforward. Double resonance experiments have shown that the ionisation step is equally efficient for all the observed ion-pair states of ICl as shown in this chapter for the $f'0^+(^1D_2)$, $\beta 1(^3P_2)$, $G1(^3P_1)$ and $H'1(^1D_2)$ states [11, 12] as well as other work

on the E state itself [7]. Strong predissociation of these states also seems unlikely since the DRINCS studies in chapter 2 on the 0_g^+ ion-pair states of I_2 in a similar energy region, show no evidence for the abscence of entire states, only predissociation of individual vibrational levels. The most probable explaination lies in the fact that the lowest energy 0^+ ion-pair state in both the homo and heteronuclear molecules is unique in that it is the only state with the configuration [1441] and can therefore be accessed via a strong $\sigma^* \longrightarrow \sigma^*$ transition.

In contrast to the first tier ion-pair states which correlate with $I^+ \, ^3P_2$, in pure precession [13], states which belong to different J_{I^+} clusters do not couple with one another and hence the second tier states, $f0^+(^3P_0)$ and $G1(^3P_1)$, are not expected to interact heterogeneously. As a result, access to the second tier ion-pair states of ICl requires the use of both the $B0^+$ and the $A1$ intermediate states. Brand et al. [14] using an OODR pulsed polarisation-labelling technique reported vibrational levels v'=0–14 of the $f0^+(^3P_0)$ which have been extended up to v'=75 by Donovan et al. using the DRINCS technique [7].

In chapter 2, the first, second and third-tier 0_g^+ ion-pair states of I_2 were observed in one series of experiments using DRINCS. In this chapter, a similar technique is used to investigate the first, second and third-tier $\Omega = 1$ ion-pair states of ICl populated via the intermediate $A1$ state. The observation of two new ion-pair states of ICl, the $H'1(^1D_2)$ and $f\,'0^+(^1D_2)$, are also reported, where the latter was accessed via the intermediate $B0^+$ state.

4.2 Experimental

The DRINCS experimental arrangement has been described in chapter 2. The molecular beam for ICl was generated by passing pressures of ~200 Torr of argon carrier gas over solid ICl_3 at 300K which dissociates to ICl + Cl_2 in the gas phase.

For the observation of the three lowest Ω=1 ion-pair states the dyes Rhodamine 6G or Rhodamine B were used in the pump laser and frequency-doubled Coumarin

153, Rhodamine 6G and Rhodamine B in the probe. The $f\,'0^+$ ion-pair state was observed using the dye Coumarin 153 in the pump laser and frequency-doubled Rhodamine 6G or Coumarin 153 in the probe laser.

The experimental arrangement for observing dispersed fluorescence at 300K is also described in chapter 2.

4.3 Results and Discussion

4.3.1 The $f\,'0^+(^1D_2)$ State

Access to the $f\,'0^+(^1D_2)$ state was achieved using two inherently strong ($\Delta\Omega$=0) transitions via the $B(^3\Pi_{0+})$ resonant intermediate state as shown in the following double resonance scheme:

$$f\,'0^+,\ v'=2\text{–}28 \longleftarrow B0^+,\ \mathrm{v}=2 \longleftarrow X0^+,\ v''=0$$

where the pump laser was set to the (2, 0) band head of the $B\leftarrow X$ transition of $I^{35}Cl$, which is close to the band origin and lies $\sim$5 cm^{-1} to higher energy than the (2, 0) band head of $I^{37}Cl$ allowing the former to be uniquely excited. From published data the energy of the intermediate level lies at 17855.9 cm^{-1} [15].

However, the $B(^3\Pi_{0+})$ state is crossed by a repulsive state and has only four bound levels, with the highest (v=3) having a lifetime in the subnanosecond range [16]. As a result, transitions to these levels from v''=0 of the ground state are very unfavourable due to the very small Franck-Condon (FC) factors where that of the (2, 0) transition is only 2×10^{-5} [17]. The v'=0 and 1 levels of the $f\,'0^+$ state are absent from the spectra, again as a result of unfavourable FC factors.

The DRINCS spectrum of $I^{35}Cl$ in figure 4.2 shows three vibrational progressions with local spacings of 89, 131 and 159 cm^{-1}, where the first two can be characterised from known molecular constants as the $E0^+$ and $f0^+$ state progressions from the first and second ion-pair clusters respectively. The last is the third

cluster $f\,'0^+$ state following the nomenclature for I_2. As discussed previously, poor FC overlap between the B and low vibrational levels of the f' states accounts for the low intensity of these levels and the absence of v'=0 and 1.

Determination of the absolute vibrational numbering of the $f\,'0^+$ state was achieved by recording the dispersed fluorescence at 300K as illustrated in figure 4.3, where the pump and probe lasers are fixed on the v'=3 resonance as in the nozzle cooled experiment. Fluorescence from $J' \leq 5$ in the $f\,'0^+$ state terminating on the bound levels of the ground $X0^+$ state shows the characteristic nodal structure from v'=3.

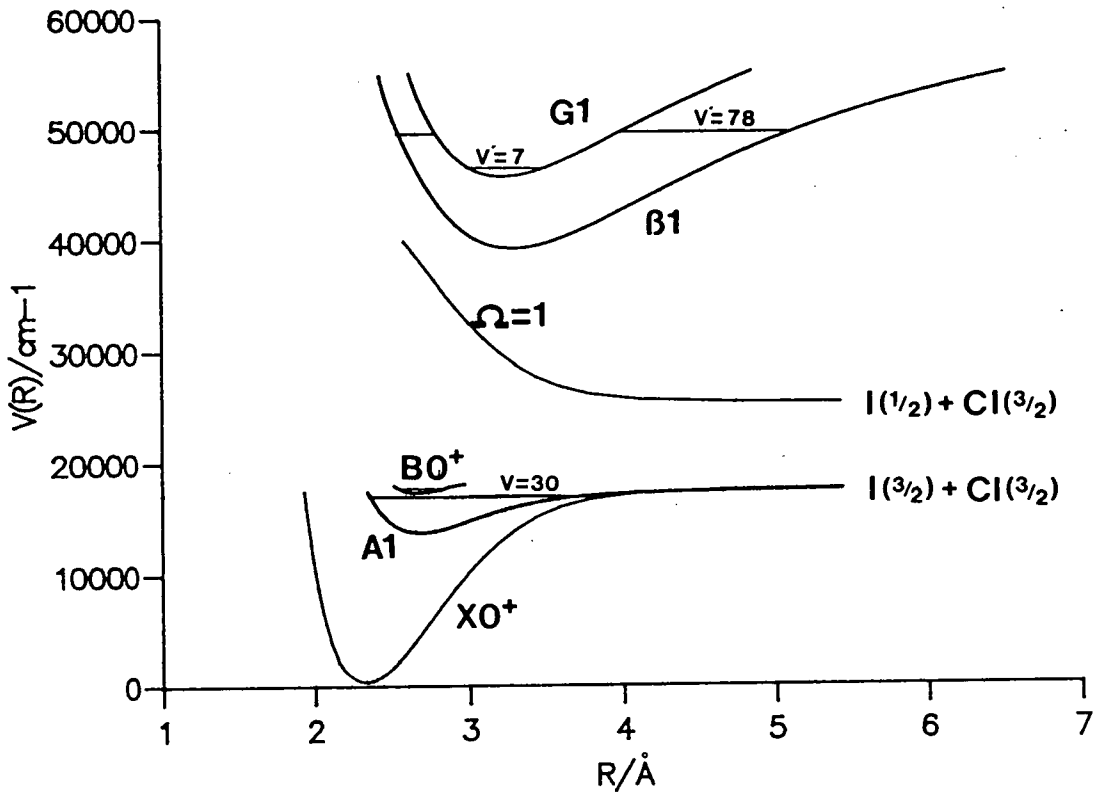

Figure 4.1. Potential energy curves of the observed ion-pair states of $I^{35}Cl$ up to and beyond the full RKR potentials.

The observed two-photon double resonance transition energies to $f\,'0^+$ (v'=2–28) given in table 4.1 were fitted to a third order Dunham expansion whose coefficients are listed in table 4.2. From accurate dissociation energies and T_e values of the first, second and third-tier 0^+ ion-pair states of ICl a progressive increase in D_e values is evident; D_e^E=33698, D_e^f=34284 and $D_e^{f\,'}$=35288 cm^{-1}. The large value of the latter is in fact more similar to the $F\,'0_u^+$ third tier state of I_2, rather than its gerade partner, $f\,'0^+$, which has an anomalously small D_e value [18].

Although all the D_e and ω_e values lie in the range expected for an ion-pair state, there is no close correlation between them. For example, although the $f\,'0^+$ state of ICl has the largest D_e value, it also has the smallest ω_e value where ω_e^E=165.6 cm^{-1}, ω_e^f=184.4 cm^{-1} and $\omega_e^{f\,'}$=160.72 cm^{-1}.

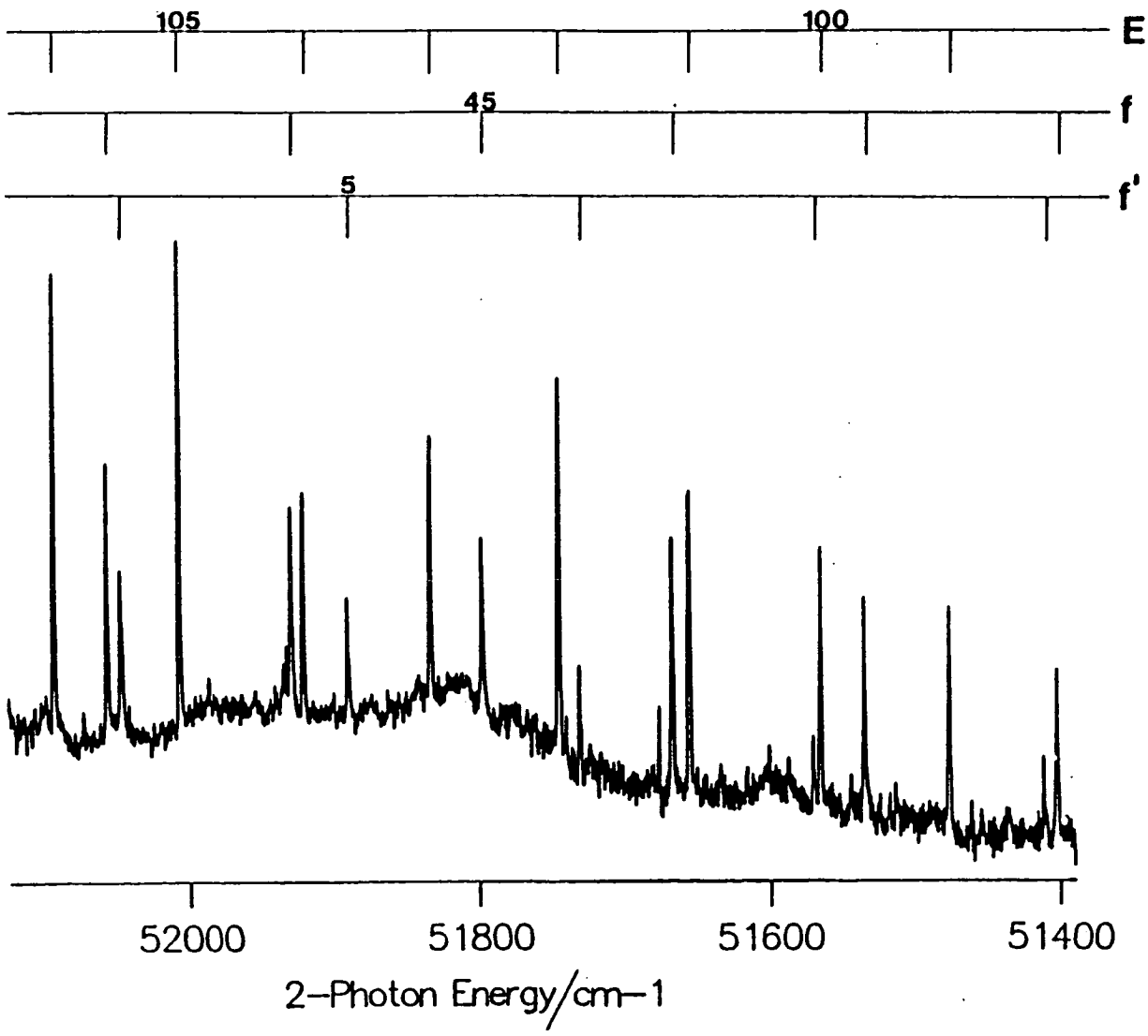

Figure 4.2. Part of the DRINCS excitation spectrum of three 0^+ ion-pair states (E, f and f') of $I^{35}Cl$, via v=2 of the $B0^+$ state.

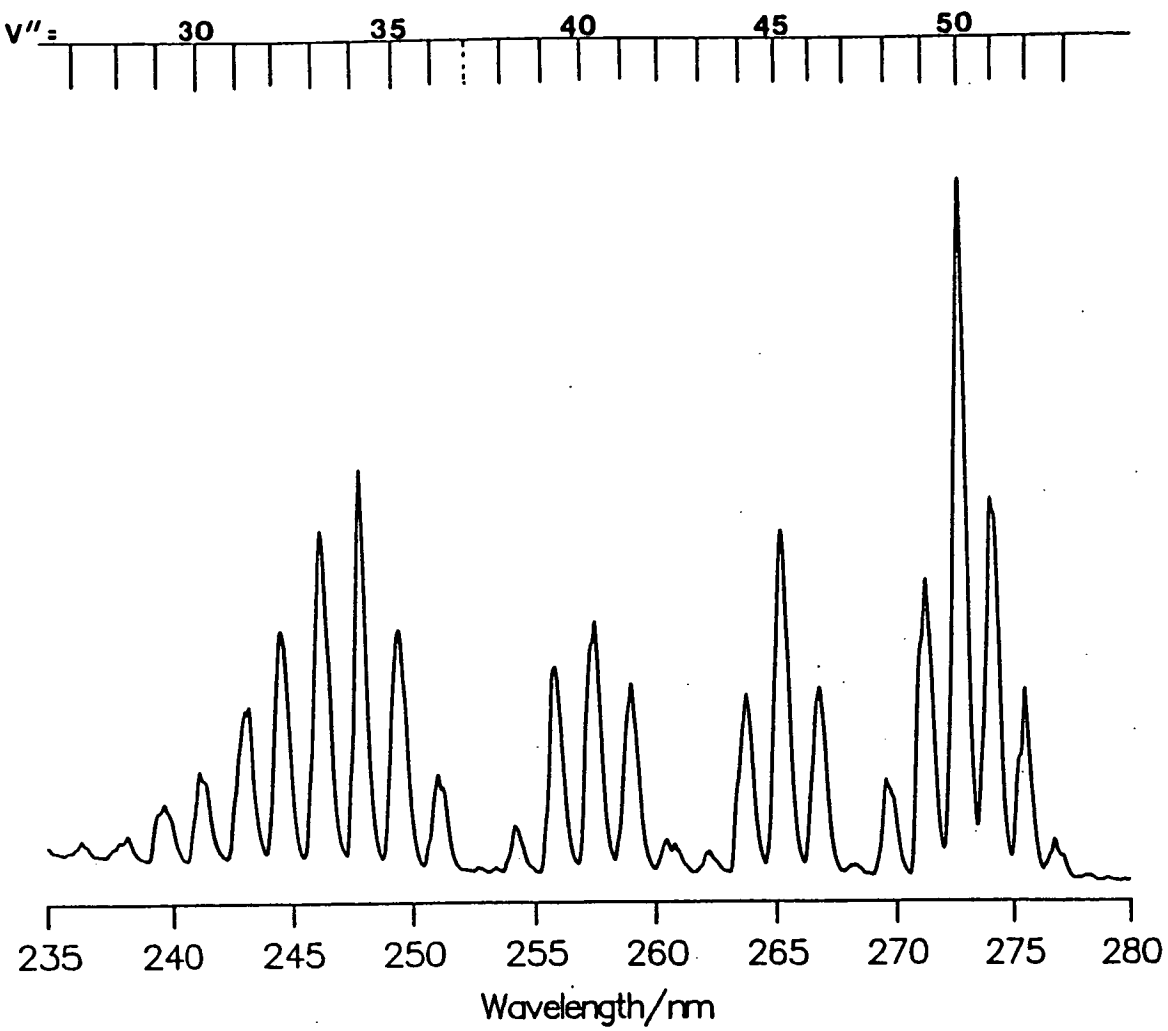

Figure 4.3. Dispersed fluorescence from v'=3 of the $f\,'0^+$ state of $I^{35}Cl$ to a range of vibrational levels of the X state.

v'	$\tilde{\nu}$ (cm^{-1})	$\tilde{\nu}_{obs-calc}$ (cm^{-1})	v'	$\tilde{\nu}$ (cm^{-1})	$\tilde{\nu}_{obs-calc}$ (cm^{-1})
0	-	-	15	53447.0	–0.1
1	-	-	16	53600.5	+0.1
2	51408.9	+0.2	17	53753.1	–0.1
3	51568.2	–0.1	18	53905.3	–0.2
4	51727.3	–0.1	19	54056.9	–0.3
5	51885.9	–0.1	20	54208.4	+0.1
6	52044.1	–0.2	21	54358.4	–0.4
7	52202.1	+0.1	22	-	-
8	52359.3	–0.1	23	54658.2	+0.1
9	52516.4	+0.2	24	54806.8	–0.1
10	52672.7	+0.1	25	54954.9	–0.1
11	52828.6	+0.1	26	55102.2	–0.3
12	52983.8	–0.1	27	55248.9	–0.5
13	53138.8	0.0	28	55395.5	–0.1
14	53293.3	+0.1			

Table 4.1. Two-photon transition wavenumbers for the vibrational levels of the $f\,'0^+(^1D_2)$ state of $I^{35}Cl$. Values accurate to ± 0.4 cm^{-1}.

Dunham Coefficient	f' state/cm^{-1}
Y_{00}	51199.96
Y_{10}	160.72
Y_{20}	-1.93×10^{-1}
Y_{30}	-1.57×10^{-3}

Table 4.2. Vibrational Dunham coefficients, valid up to v'=28, for the $f\,'0^+(^1D_2)$ state of $I^{35}Cl$.

4.3.2 The $\beta 1(^3P_2)$, $G1(^3P_1)$ and $H'1(^1D_2)$ States

The double resonance excitation scheme used for most experiments was:

$$i.p.(1), v' = n \longleftarrow A1, v = 30 \longleftarrow X0^+, v'' = 0,$$

where v=30 is within ~110 cm^{-1} of the dissociation limit of the A state and has a favourable FC overlap with a large range of ion-pair state vibrational levels [19]. The (30, 0) band head of $I^{35}Cl$ is separated by ~ 10 cm^{-1} from the (30, 0) and (31,0) bands of $I^{37}Cl$ and thus there is no interference from this isotopomer. The prohibitively small FC overlap between the intermediate A, v=30 levels and v' <5 of the H' state meant that these levels were populated via v=14 of the A state.

A section of the DRINCS spectrum of $I^{35}Cl$ in the energy region around T_e of the H' state is shown in figure 4.4 where transitions to high vibrational levels of the β and G states can also be seen together with atomic iodine lines resulting from coherent (2+1) ionisation by the probe laser. The two additional bands in figure 4.4, which did not appear when the intermediate levels v'=20, 22 or 30 of the A state were used may arise through interactions at the intermediate level since they could not be assigned to any ion-pair states. The upper vibrational limit to the present experiments was purely arbitrary and should not be seen as an end to the progressions which in fact did not show any significant fall-off in intensity towards higher energies. The lower limit was determined by the data needed to unambiguously number the vibrational levels of the β and G states when combined with the existing data [4, 20].

The two-photon transition wavenumbers of the vibrational levels between v'=0–18 of the H' state of $I^{35}Cl$ are given in table 4.3 and fitted to a second-order Dunham expansion whose coefficients are given in table 4.6. The absolute numbering of the progression was achieved in a similar manner to that described in section 4.3.1 with dispersed fluorescence from $J' \leq 5$ of v'=0 of the H' state terminating on bound levels of the A state as shown in figure 4.5 which displays a characteristic single lobe of intensity.

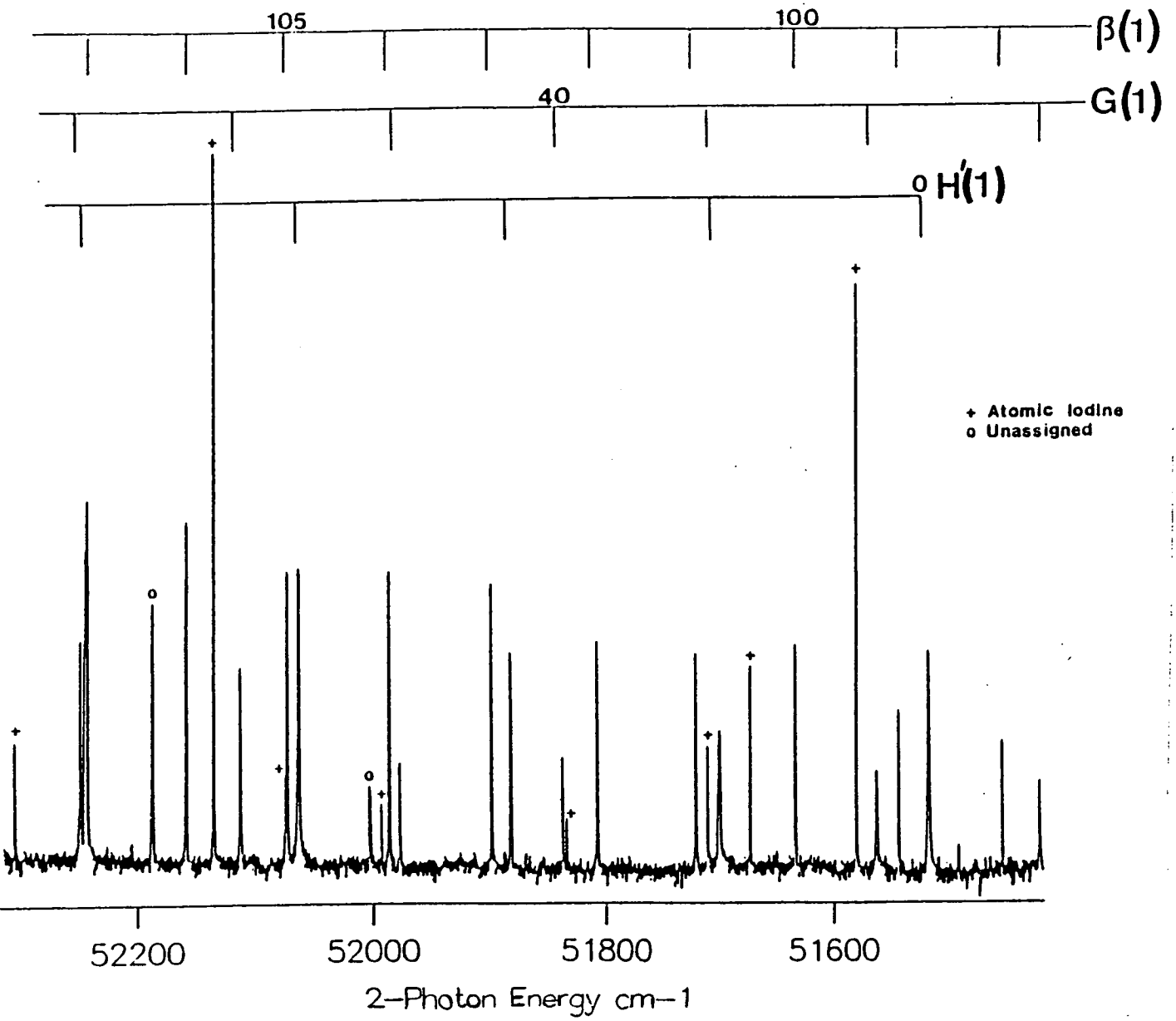

Figure 4.4. DRINCS spectrum of $I^{35}Cl$ via the $A(v{=}14)$ level, in the region of the origin of the H' state. The atomic iodine lines are due to coherent (2+1) ionisation by the probe laser.

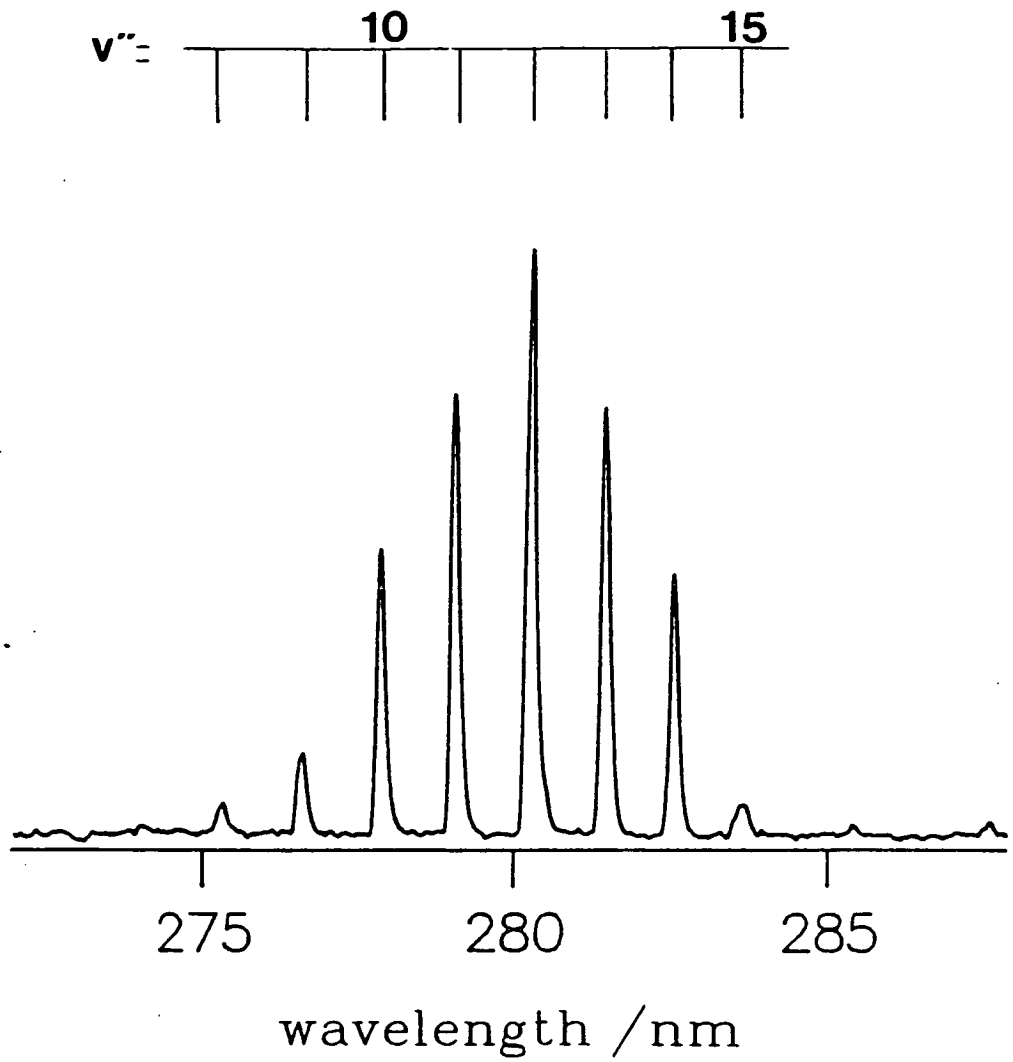

Figure 4.5. Dispersed fluorescence from $H'(v'=0)$ of $I^{35}Cl$, at room temperature, to bound vibrational levels of the A state.

The two-photon transition energies to v'=25–63 of the G state shown in table 4.4 were combined with the regenerated term values for v'=0–7 from the published constants of Brand et al. [20] and fitted to a fourth-order Dunham expansion whose coefficients are given in table 4.6.

A similar procedure was attempted to fit the vibrational levels v'=80–137 of the β state shown in table 4.5. Although the numbering of these levels was unambiguous there was a discrepancy of $\sim$ 10 cm^{-1} between our lowest values and those generated by the constants reported to be valid up to v'=78 by Bussieres and Hoy [4]. However, in a previous paper [3], the very same constants were used only up to v'=54 and therefore we have used these constants to generate vibrational levels v'=0–54 and combined them with the present observed levels, v'=80–137, to produce a fifth-order Dunham expansion whose coefficients are given in table 4.6. The v'=111–115 levels of the $\beta 1$ state are missing in the DRINCS spectrum probably as a result of poor FC overlap between the A and β state levels, although a local perturbation or predissociation in this region cannot be ruled out. Examples of perturbations in ICl involving Rydberg/ion-pair mixing, have been seen in fluorescence excitation and coherent (2+1) REMPI studies as discussed in section 4.1

The calculated D_e values of the $\beta 1(^3P_2)$, $G1(^3P_1)$ and $H'1(^1D_2)$ states are 33576.6, 34214.0 and 34795.2 cm^{-1} respectively. The first state also has a lower than expected ω_e value of 170.4 cm^{-1} compared to $\sim$ 184 cm^{-1} for the other two states suggesting that the potential minimum of the $\beta 1(^3P_2)$ state has been forced up as a result of an interaction with a steeply rising valence state correlating with I($^2P_{1/2}$)+Cl($^2P_{1/2}$ or $^2P_{3/2}$). Inverting the long range behaviour of the $X(0^+)$ ground state suggests that the repulsive valence state would lie $\sim$9000 cm^{-1} below the β state at R_e^β (3.288 Å) as shown in figure 4.1. The valence MOs have assumed mainly atomic (or atomic ion) character at this separation with $\sigma = Cl(3p_\sigma)$, $\pi = Cl(3p_\pi)$, $\pi^* = I(5p_\pi)$, $\sigma^* = I(5p_\sigma)$ and a typical repulsive valence state configuration having Ω=1 would be $\sigma^2\pi^3\pi^{*3}\sigma^{*2}$ or more compactly $[2332]^3\Sigma_1^+$ or $[1432]^3\Pi_1$. The latter component would interact more strongly

with the β state, which in the pure precession limit of I^+Cl^- is the combination $[2442]^3\Sigma_1^+ + [2431]^3\Pi_1$.

This behaviour is also seen in the first two 1_u states of I_2 being most pronounced in the lowest state, but not in the 1_g states possibly because the highest energy asymptote, $X(^2P_{1/2})+X(^2P_{1/2})$, generates only a 1_u valence state and not a 1_g state [21]. Interaction between ion-pair states themselves can be discounted because the $\beta 1(^3P_2)$ state being the lowest Ω=1 state, would be forced down, not upwards and have the largest D_e value.

v'	$\tilde{\nu}$ (cm^{-1})	$\tilde{\nu}_{obs-calc}$ (cm^{-1})	v'	$\tilde{\nu}$ (cm^{-1})	$\tilde{\nu}_{obs-calc}$ (cm^{-1})
0	51515.3	–0.3	10	53290.3	–0.1
1	51698.5	0.0	11	-	-
2	51880.2	+0.1	12	53631.1	+0.1
3	52060.8	+0.2	13	53799.2	–0.3
4	52239.9	+0.1	14	53966.7	–0.2
5	52418.1	+0.2	15	-	-
6	52594.7	–0.1	16	54298.2	+0.2
7	52770.5	0.0	17	54462.0	+0.2
8	52944.9	–0.1	18	54624.3	0.0
9	53118.3	0.0			

Table 4.3. Two-photon transition wavenumbers for the vibrational levels of the $H'1(^1D_2)$ state of $I^{35}Cl$. Values accurate to $\pm$ 0.4 cm^{-1}.

v'	$\tilde{\nu}$ (cm^{-1})	$\tilde{\nu}_{obs-calc}$ (cm^{-1})	v'	$\tilde{\nu}$ (cm^{-1})	$\tilde{\nu}_{obs-calc}$ (cm^{-1})
25	49659.0	+0.2	45	52513.1	+0.1
26	-	0-	46	52645.2	0.0
27	49963.3	+0.1	47	52776.1	–0.4
28	50113.6	–0.1	48	52906.8	0.0
29	50263.3	+0.1	49	53966.7	0.0
30	50411.4	+0.2	50	53164.6	0.0
31	50558.8	–0.1	51	53292.2	0.0
32	50705.3	0.0	52	553418.8	–0.1
33	50850.1	–0.1	53	53544.5	–0.1
34	50994.1	0.0	54	-	-
35	51137.3	+0.1	55	53793.2	–0.2
36	51279.5	+0.2	56	53916.8	+0.3
37	51420.6	+0.1	57	54038.8	+0.1
38	51560.6	+0.2	58	54160.1	0.0
39	51699.6	+0.1	59	-	-
40	51837.4	+0.2	60	54400.4	+0.1
41	51974.5	+0.1	61	554519.1	0.0
42	52110.6	+0.2	62	54636.8	–0.2
43	52246.1	+0.1	63	54754.0	–0.1
44	52379.8	+0.2			

Table 4.4. Two-photon transition wavenumbers for the vibrational levels of the $G1(^3P_1)$ state of $I^{35}Cl$. Values accurate to $\pm$ 0.4 cm^{-1}.

v'	$\tilde{\nu}$ (cm^{-1})	$\tilde{\nu}_{obs-calc}$ (cm^{-1})	v'	$\tilde{\nu}$ (cm^{-1})	$\tilde{\nu}_{obs-calc}$ (cm^{-1})	v'	$\tilde{\nu}$ (cm^{-1})	$\tilde{\nu}_{obs-calc}$ (cm^{-1})
80	49724.5	–0.1	100	51632.0	+0.1	119	53224.3	–0.2
81	49825.6	–0.5	101	51720.9	+0.4	120	53303.2	–0.5
82	49926.7	–0.2	102	51809.1	+0.3	121	53381.2	–0.1
83	50027.2	+0.1	103	51896.7	+0.2	122	53458.5	–0.2
84	50126.4	–0.1	104	51983.9	+0.3	123	53535.8	–0.4
85	50225.5	0.0	105	52070.4	+0.2	124	53612.2	–0.1
86	50323.8	+0.2	106	52156.3	+0.1	125	53688.5	–0.3
87	50420.9	–0.3	107	52241.9	+0.3	126	53763.8	0.0
88	50517.7	–0.3	107	52326.3	–0.2	127	53838.9	–0.3
89	50614.1	–0.2	108	52411.2	–0.2	128	53913.7	–0.2
90	50709.9	+0.1	109	52494.5	+0.3	129	53987.9	+0.1
91	50804.7	–0.1	110	54061.4	–0.2	130	54061.4	0.0
92	-	-	111	-	-	131	54134.5	0.0
93	50992.6	–0.2	112	-	-	132	54207.2	–0.1
94	51086.0	+0.1	113	-	-	133	54279.5	0.0
95	51178.6	+0.2	114	-	-	134	54351.5	+0.2
96	51270.2	0.0	115	-	-	135	54422.9	+0.4
97	51361.4	–0.1	116	52985.9	–0.2	136	54493.4	0.0
98	51452.3	+0.2	117	53066.2	0.0	137	54563.7	0.0
99	51542.3	+0.1	118	53145.5	–0.2			

Table 4.5. Two-photon transition wavenumbers for the vibrational levels of the $\beta 1(^3P_2)$ state of $I^{35}Cl$. Values accurate to $\pm$ 0.4 cm^{-1}.

Dunham coefficient	$H'^{(a)}$ (cm^{-1})	$G^{(b)}$ (cm^{-1})	$\beta^{(c)}$ (cm^{-1})
Y_{00}	51615.6	45552.8	39103.2
Y_{10}	184.03	184.844	170.4289
Y_{20}	-5.96×10^{-1}	-6.8277×10^{-1}	-4.705977×10^{-1}
Y_{30}		1.77427×10^{-3}	-1.13677×10^{-4}
Y_{40}		-2.80777×10^{-6}	6.05777×10^{-6}
Y_{50}			-1.53467×10^{-8}
D_e	34795.2	34214.0	33576.6

Table 4.6. Vibrational Dunham coefficients for the H', G and β states of $I^{35}Cl$.

(a) Valid up to v'=18.

(b) Valid up to v'=63.

(c) Valid up to v'=137.

Conclusion

In concluding the last two chapters on the halogen and interhalogen ion-pair states several important aspects of their spectroscopic behaviour are summarised.

The simple picture of ion-pair states as two ions $X^+ + Y^-$ has proved a good starting point in discussing their unusual spectroscopic behaviour i.e small ω_e and large D_e and R_e values compared with conventional valence states. However, in order to reproduce their observed vibronic levels in order to produce accurate potential curves a more refined model is required where the attractive Rittner potential must be supplemented by long-range multipole terms. In this work we have accessed high lying vibronic levels of several ion-pair states well above their potential minima. As a consequence, ion-pair states are now mixed with Rydberg states at both long and short R values and are no longer relatively unpertubed. At small R the extent of these avoided crossings have been successfully discussed using the MO description of electronic structure which is complimentary to the separated ion model used at large R in describing the attractive part of their potentials.

4.4 References

1. R. H. Barnes, C. E. Moeller, J. F. Kirchen and C. M. Verber, *Appl. Phys. Lett.* **24**(1974)610.

2. G. W. King and I. M. Littlewood, R. G. McFadden and J. R. Robins, *Chem. Phys.* **41**(1979)379.

3. J. C. D. Brand, U. D. Desphande, A. R. Hoy, S. M. Jaywant *J. Mol. Spec.* **100**(1983)416.

4. D. Bussieres and A. R. Hoy, *Can. J. Phys.* **62**(1984)1941.

5. J. Tellinghuisen, *J. Chem. Phys.* **82**(1985)4012.

6. R. H. Lipson and A. R. Hoy, *J. Chem. Phys.* **90**(1989)6821.

7. R. J. Donovan, J. G. Goode, K. P. Lawley, T. Ridley and A. J. Yencha, *J. Phys. Chem.* **98**(1994)2236.

8. T. Ridley, K. P. Lawley, R. J. Donovan and A. J. Yencha, *Chem. Phys.* **148**(1990)315.

9. R. J. Donovan, R. V. Flood, K. P. Lawley, A. J. Yencha and T. Ridley, *Chem. Phys.* **164**(1992)439.

10. R. J. Donovan, R. V. Flood, K. P. Lawley, R. Maier, C. R. Redpath T. Ridley and A. J. Yencha, *Arabian J. Sci. and Eng.* **17**(1992)253.

A. J. Yencha, T. Ridley, R. Maier, R. J. Donovan and A. Hopkirk, *Phys. Chem.* **97**(1993)4582.

11. R. J. Donovan, T. Ridley, K. P. Lawley and P. J. Wilson, *Chem. Phys. Lett.* **205**(1993)129.

12. R. J. Donovan, T. Ridley, K. P. Lawley and P. J. Wilson, *Chem. Phys. Lett.* **207**(1993)129.

13. J. H. Van Vleck, *Phys. Rev.* **33**(1929)467.

14. J. C. D. Brand, A. R. Hoy and S. M. Jaywant, *J. Mol. Spec.* **108**(1984)388.

15. R. D. Gordon and K. K. Innes, *J. Mol. Spec.* **78**(1979)350.

16. R. D. Gordon and K. K. Innes, *J. Chem. Phys.* **71**(1979)2824.

17. M. A. A. Clyne and I. S. McDermid, *J. Chem. Soc. Farad. Trans.* **72**(1976)2242.

18. R. J. Donovan, T. Ridley, K. P. Lawley and P. J. Wilson, *Chem. Phys. Lett.*, **196**(1992)173.

19. J. A. Coxon and M. A. Wickramaaratchi, *J. Mol. Spec.*, **79**(1980)380.

20. J. C. D. Brand, U. D. Deshpande, A. R. Hoy and E. J. Woods, *Can. J. Chem.*, **61**(1983)846.

21. M. Saute and M. Aubert-Frecon, *J. Chem. Phys.*, **77**(1982)5639.

Chapter 5

Vibronic Coupling Between an Ion-Pair and Rydberg State of I_2

5.1 Introduction

Numerous spectroscopic studies of the Rydberg states of I_2 show that these states dominate the spectrum obtained by absorption and REMPI techniques [1]. However, there is very little evidence of transitions to ion-pair states. The application of the (2+1) REMPI technique to I_2 by Dalby et al. [2] provided the first coherent two-photon transitions to gerade Rydberg states. Henceforth, a large number of gerade Rydberg states of I_2 have now been observed using this technique as discussed in more detail in chapter 1.

Even number photon transitions (usually two) from the ground state are to s or d Rydberg orbitals which maintain an overall gerade symmetry state based on the two spin-orbit components of the ground electronic state of the I_2^+ ion core, $[2430]^2\Pi_g$. It is these states which are primarily responsible for the observed perturbations in the DRINCS spectra discussed in chapter 2.

Systematic studies of the Rydberg states of I_2 using (2+1) REMPI in the 48,000–85,000 cm^{-1} energy range have been carried out by Donovan et al. here at Edinburgh [3]. They assigned the $[^2\Pi_{3/2g}]ns$ and $[^2\Pi_{1/2g}]ns$ Rydberg states up to n=11 and n=8 respectively, together with three $5d$ states based on each core from quantum defects, rotational band contour analysis and polarisation ratios.

Using jet-cooled REMPI techniques, in addition to the strong Rydberg transitions which dominate the spectra, an ion-pair system could be resolved above ~58,000 cm^{-1} suggesting the latter have gained intensity by mixing with the adjacent $[^2\Pi_{\frac{3}{2}g}]5d$ Rydberg system [4, 5].

In this chapter, a detailed investigation of the vibronic coupling between these states is carried out using jet-cooled REMPI techniques. In general, only high lying vibrational levels of the ion-pair states can be accessed using this technique since a coherent two-photon absorption via a virtual intermediate state must involve a vertical transition. Jet-cooling allows the vibrational progression of the ion-pair state to be readily resolved. In addition, the ionisation product(s) as a function of excitation energy are studied using mass analysis.

Results of calculations on the coupled two-state system will provide a quantitative measure of the magnitude of H_{12}^{el} which will be discussed in terms of the electronic configurations of the two states.

5.1.1 Coupling of Excited States

THE BORN-OPPENHEIMER APPROXIMATION

In order to solve the exact Schrödinger wave equation for a diatomic molecule,

$$H_i\psi_i = E_i\psi_i \tag{5.1}$$

it is necessary to approximate the nonrelativistic Hamiltonian by a sum of three terms each representing interactions between different particles,

$$H^{BO} = \mathbf{T^N}(R, \theta, \phi) + \mathbf{T^e}(r) + V(r, R) \tag{5.2}$$

where $\mathbf{T^N}$ is the nuclear kinetic energy operator which can be separated into radial and angular components, $\mathbf{T^N}(R) + \mathbf{H^{rot}}$. $\mathbf{T^e}$ is the electron kinetic energy operator and V is the electrostatic potential energy for the nuclei and electrons which includes e–e, e–N and N–N interactions. R is the internuclear distance, r represents the electron's coordinates in the molecule fixed system and θ and ϕ

represent the orientation of the internuclear axis in the molecule-fixed coordinate system.

Solution of equation 5.2 leads to eigenvalues which can be represented by the sum of three energy contributions,

$$E^{BO} = E^{el} + G_v + F(J) \tag{5.3}$$

where E^{el}, G_v and $F(J)$ are the electronic, vibrational and rotational energies respectively. The separation of these terms is valid due to the slower velocity of the nuclei compared with the electrons, i.e $T^N/T^e \equiv \mu/m_e \approx 2000$. In the B.O approximation, terms in **H** between the nuclear and electronic motions are not included.

It is important to remember that in order to try to obtain an exact solution to equation 5.1 it is necessary to go beyond the BO approximation where off-diagonal matrix elements are neglected, but it is necessary to use a BO representation. The wavefunction which represents the approximate energy expression in equation 5.3 is a product of two functions,

$$\psi^{BO}_{i,v} = \Phi_i(r, R)\chi_v(R, \theta, \phi) \tag{5.4}$$

where the first factor is the electronic wavefunction and the second is the vibration-rotation function. Two different types of BO representation are useful starting points when evaluating perturbations resulting from a neglect in the $H^{el} + T^N(R)$ part of the Hamiltonian.

(i) The Crossing (**DIABATIC**) Representation.
The off-diagonal matrix elements of H^{el} connecting the two BO states states, Φ^d_1 and Φ^d_2, which give rise to electrostatic perturbations are defined by,

$$\langle \Phi^d_1 | H^{el} | \Phi^d_2 \rangle = H^{el}_{12} \neq 0 \tag{5.5}$$

$$\langle \Phi^d_1 | T^N | \Phi^d_2 \rangle = 0 \tag{5.6}$$

where H^{el} is the electronic matrix element between the two diabatic states, Φ^d and is usually assumed to be a slowly varying function of R (through the V^{ee}

term in $V(r, R)$) and is often assigned a constant value, $H^e = H^e_{12}(R_c)$ where R_c is the crossing point of the two curves. In this work, an exponential coupling term is used. Φ^d can be approximated by a single configuration function and because $\mathbf{H^{el}}$ is a two-electron operator the interacting configurations may differ by two spin-orbitals.

When the H^{el} coupling term is small and there is little mixing of the configurations around R_c in the adiabatic representation then the diabatic representation is most appropriate and the deperturbed potential energy curves will cross. Even if H^{el} is large, a diabatic basis is still a valid starting point and is particularly useful because the single configuration approach retains the electronic parentage of the two interacting states and therefore they can be conveniently modelled from previous data as is the case for this work because no information is available on the adiabatic curves.

(ii) The Non-Crossing (**ADIABATIC**) Representation.

In contrast to the diabatic representation, the adiabatic basis functions diagonalise H^{el} and therefore the potential energy curves of these states cannot cross. The off-diagonal matrix elements connecting the two adiabatic states are,

$$\langle \Phi_1^{ad} | T^N | \Phi_2^{ad} \rangle = H^{el}_{1,v_1,2,v_2} \neq 0 \tag{5.7}$$

$$\langle \Phi_1^{ad} | H^{el} | \Phi_2^{ad} \rangle = 0 \tag{5.8}$$

The non-zero matrix element is called the non-adiabatic coupling term and gives rise to homogeneous interactions between states of identical symmetry. If the states mix then the non-adiabatic coupling term is a strongly varying function of R around R_c. Adiabatic potential energy curves are generally more difficult to construct compared to diabatic ones and usually require either deperturbed potential energy curves determined from experimental data or those obtained from *ab initio* calculations. However, it is possible to construct adiabatic curves in the diabatic basis, although I shall not expand on this here, the reader is referred to reference [6] for more details.

5.2 Experimental

The jet-cooled REMPI linear TOF experimental arrangement has been discussed in chapter 2. Argon at pressures of up to 500 mbar was passed through a trap containing I_2 producing a gas mixture of ≈0.2–1.0 % halogen in argon. The resulting mixture was then expanded through the pulsed nozzle into a vacuum chamber.

The fundamental output of the dyes DMQ and PTP covered the energy range 57000–59600 cm^{-1}.

5.3 Results

The room temperature (2+1) REMPI spectra of the Rydberg states of I_2 in the 48,000–85,000 cm^{-1} energy range obtained in previous studies by this group [3] showed that strong Rydberg transitions dominate the spectra.

In the jet-cooled, mass-analysed (2+1) REMPI studies of I_2 between ~48000–70000 cm^{-1} an ion-pair system can be resolved above ~58000 cm^{-1}. The I^+ spectrum in the two-photon energy region between 57200–59600 cm^{-1} is shown in figure 5.1. A clearly resolved vibrational progression can be seen, with an average vibrational spacing that decreases from ~34–26 cm^{-1} over this energy range, indicative of a first tier ion-pair state whose identity must be one of the three possible gerade states, $E0_g^+$, $\beta 1_g$ and $D'2_g$ states.

The $E0_g^+$ state can be eliminated as a possible candidate because from the DRINCS studies on I_2 presented in chapter 2, $E0_g^+$ vibrational levels which were accessed in the same energy region (v'_E=255–328 in table 2.2a and 2.2b)) do not correspond with those seen here. The $\beta 1_g$ state can be eliminated as the perturbing state from it s observed interactions or lack of them with various Rydberg states in the energy range between ~48000–70000 cm^{-1}. From a knowledge of the T_e

values of the Rydberg states (all the R_e^{Ryd} values of are assumed to be the same as for the $[1/2]6s : 1_g$ state), the form of the repulsive branch of the $\beta 1_g$ state can be estimated as shown in figure 5.2 where the circles indicate an observed Rydberg/ion-pair interaction. The most certain piece of information is that there is a strong interaction between the $[3/2]7s : 1_g$ state [4] and the $\beta 1_g$ ion-pair state. This crossing occurs between v'=0 and 1 and can be at either the inner or outer wall of the Rydberg state. If the crossing occurs at the outer wall, as shown in figure 5.2, then as a consequence the $\beta 1_g$ state crosses the $[3/2]5d : 1_g$ state around v'=3 as reported by Kvaran [7] and the $[1/2]6s : 1_g$ Dalby system at a vibrational level which is not in the ground state FC window. This supports the unperturbed nature of the Dalby system. If the $\beta 1_g$ state crosses the $[3/2]7s : 1_g$ state at the inner wall then it must cross the $[3/2]5d : 1_g$ below v'=3 and the Dalby levels which lie in the ground state FC window. Both of these crossings would have to result in no interactions, which although not impossible, seems improbable.

The Rydberg state whose origin lies at ~58600 cm^{-1} is responsible for the interactions observed in this work and the $\beta 1_g$ state repulsive branch shown in figure 5.2, crosses it at the outer turning point of $v'_{Ryd} \approx 4$. However, the repulsive branch of the $D'2_g$ state generated in section 5.4 crosses this Rydberg state close to the outer turning point of v'_{Ryd}=1. It is the latter state whose crossing point is in agreement with the observed Rydberg/ion-pair mixing and so the Rydberg state is assigned $[3/2]5d : 2_g$.

In the low energy region of the spectrum the position of the ion-pair levels are relatively unperturbed and their intensities gradually increase towards a maximum at ~58650 cm^{-1} which corresponds to a Rydberg level. Beyond this energy, the positions of the levels become very irregular and no strong Rydberg peaks can be seen which suggests a strong interaction between the ion-pair and Rydberg states. Further evidence for strong mixing between the two states comes from the regular Franck-Condon lobe of ion-pair intensity between 58700–59000 cm^{-1} which lies in the region where a strong Rydberg peak would be expected. The sudden drop in the intensities of all levels above ~59000 cm^{-1} probably results from strong

predissociation of the Rydberg state. A full list of the term values and energy separations of the coupled ion-pair/Rydberg levels are presented in table 5.1.

In an attempt to establish the vibrational numbering of our observed levels for the $D'(2g)$ state, the unperturbed levels between 57281–58654 cm^{-1} shown in table 5.1 were compared with those of Tellinghuisen's low v' levels [7]. Tellinghuisen's vibrational levels, v'=0–30, making up the data set of highest accuracy ($\pm$0.1 cm^{-1}) were combined with our lowest 43 levels of lower precision ($\pm$1 cm^{-1}) which were added with half the weight (the levels labelled 5 and 22 were removed from the fit) and these were assigned quantum numbers n, n+1, n+2,...n+43. n was adjusted to give a minimum standard deviation, the search being from n=200 upwards. However, due to the large energy gap ($\sim$14000 cm^{-1}) between these two relatively small sets of data, the variation in the standard deviation as a function of n was very shallow, even when a low order fit was performed. We therefore, very tentatively estimate $n\approx270\pm10$.

It is the generation of the $D'2g$ ion-pair state discussed in the next section which will provide a more realistic estimate of the absolute numbering of the observed levels.

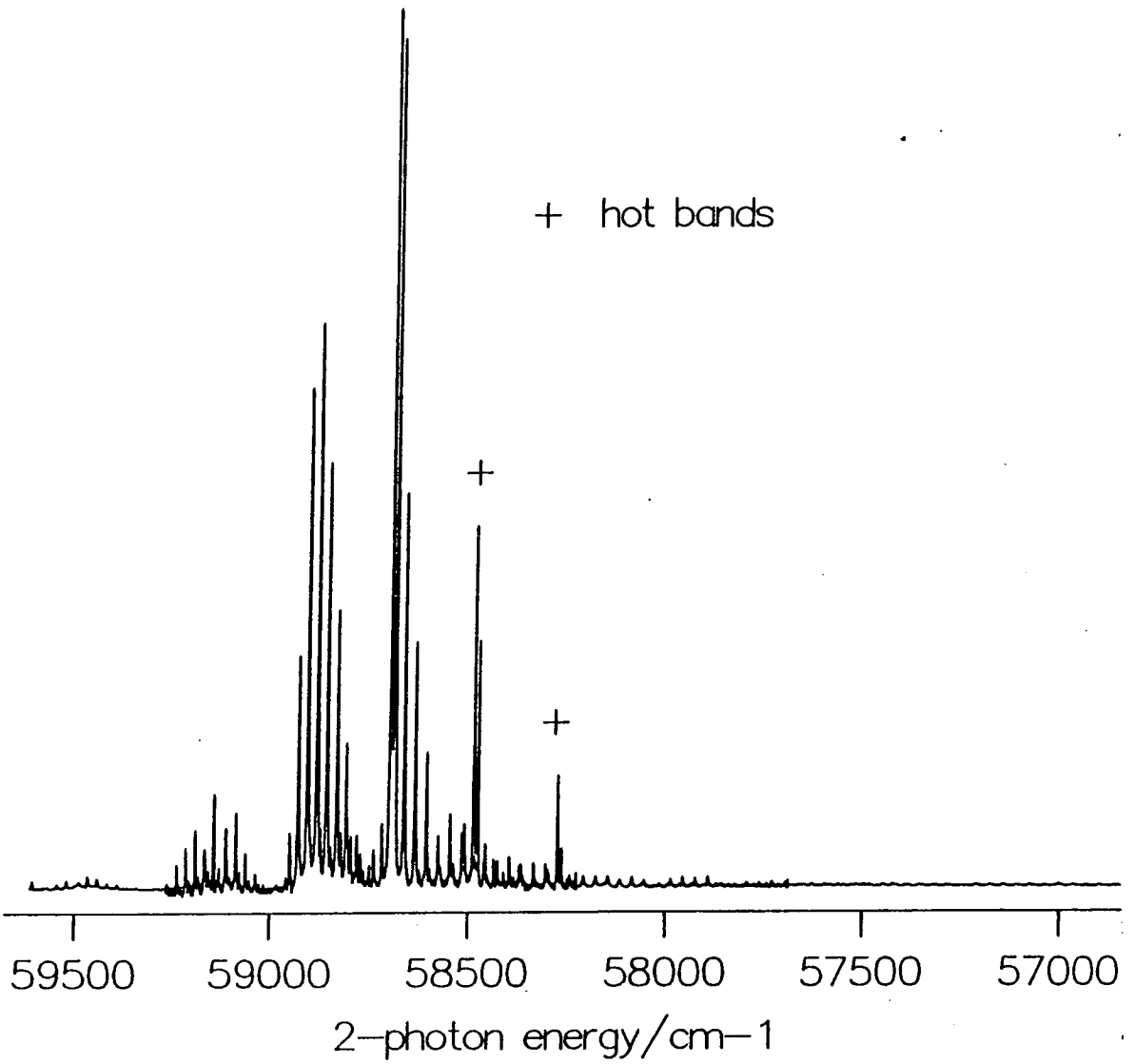

Figure 5.1. The (2+1) mass-resolved REMPI excitation spectrum of jet-cooled I_2 recorded by monitoring the I^+ mass channel.

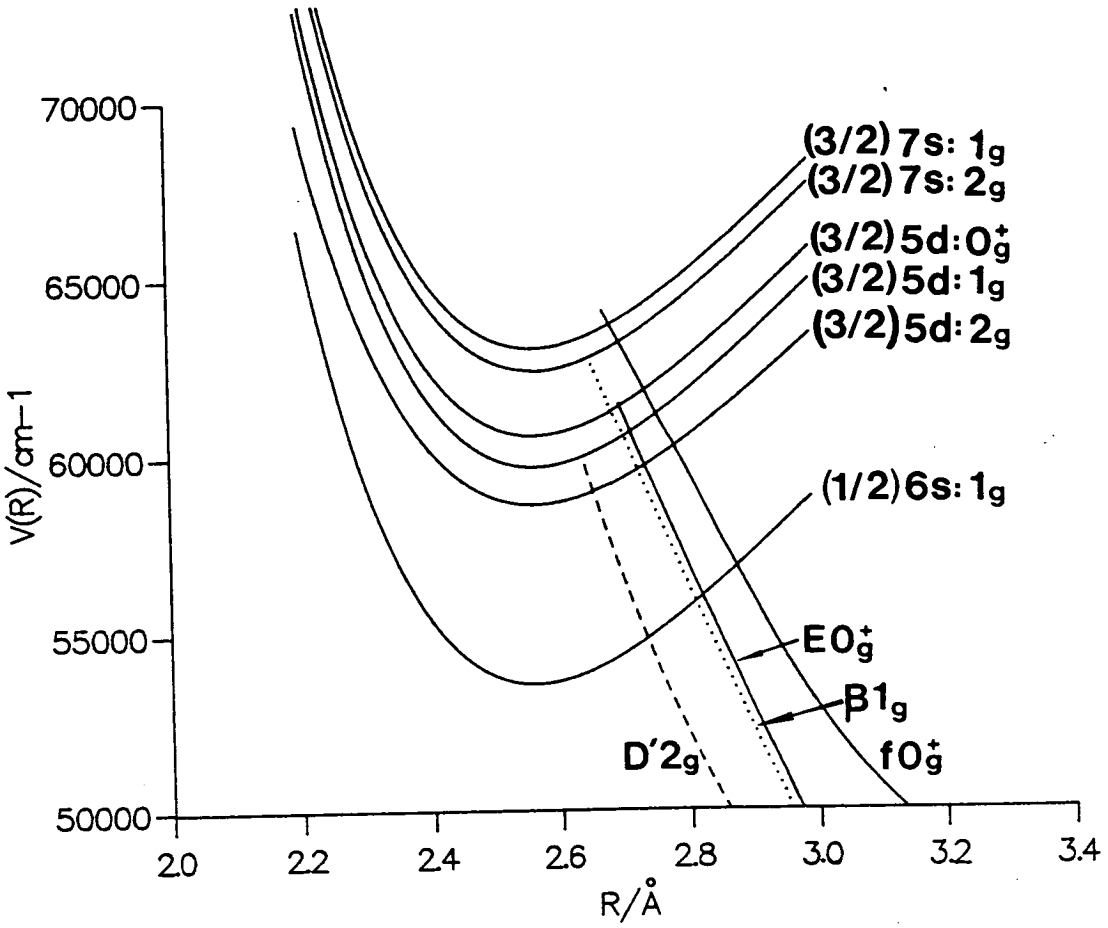

Figure 5.2. Several Rydberg/ion-pair potential curves, including the D' ion-pair state, in the region of their crossings.

	$\tilde{\nu}$ (cm^{-1})	$\Delta\tilde{\nu}$ (cm^{-1})		$\tilde{\nu}$ (cm^{-1})	$\Delta\tilde{\nu}$ (cm^{-1})		$\tilde{\nu}$ (cm^{-1})	$\Delta\tilde{\nu}$ (cm^{-1})
0	57281	-	27	58169	30	54	58923	24
1	57315	34	28	58200	31	55	58943	20
2	57348	33	29	58233	33	56	58975	32
3	57382	34	30	58265	32	57	-	-
4	57416	34	31	58294	29	58	59027	-
5	57455	39	32	58324	30	59	59054	27
6	57486	31	33	58355	31	60	59079	25
7	57519	33	34	58386	31	61	59104	25
8	57553	34	35	58415	29	62	59134	30
9	57587	34	36	58446	31	63	59155	21
10	57620	33	37	58477	31	64	59180	25
11	57653	33	38	58505	28	65	59205	25
12	57687	34	39	58537	32	66	59232	27
13	57720	33	40	58566	29	67	59257	25
14	57753	33	41	58596	30	68	59282	25
15	57785	32	42	58626	30	69	-	-
16	57817	32	43	58654	28	70	59332	-
17	57849	32	44	58678	24	71	59358	26
18	57884	35	45	58690	12	72	59383	25
19	57916	32	46	-	-	73	59408	25
20	57948	32	47	-	-	74	59433	25
21	57979	31	48	58767	-	75	59457	24
22	58009	30	49	58800	33	76	59478	21
23	58046	37	50	58826	26	77	59510	32
24	58077	31	51	58851	25	78	59533	23
25	58109	32	52	58876	25			
26	58139	30	53	58899	23			

Table 5.1. Term values for the vibrational levels of the $D'2g(^3P_2)$ state of I_2.

5.4 Generation of the $D'(2g)$ ion-pair state

Tellinghuisen et al. [7] have generated vibrational and rotational Dunham coefficients for the $D'2g$ state to calculate RKR turning points valid up to v'=30. In chapter 3, the potential energy curves of the three 0_g^+ ion-pair states of I_2 were generated beyond the previously existing RKR potentials using only the vibrational Dunham coefficients and the known asymptotic behaviour of the Coulomb branch of the potentials. However, there are no vibrational Dunham coefficients beyond the previously existing RKR potentials for the $D'2_g$ state which means the $R_+(E) - R_-(E)$ distance at each v' level is no longer available. As before, the absolute positions of the outer turning points of the extended potential are generated from our knowledge of the Coulombic branches of the halogen ion-pair potentials. Therefore, by varying the form of the repulsive inner branch the correct eigenvalues of the set of unperturbed vibrational levels observed below the crossing region were reproduced.

The first tier $D'2g$ state is the lowest lying ion-pair state in I_2 and correlates with the atomic ions $I^-(^1S_0)+I^+(^3P_2)$. As shown in chapter 3, the form of the Coulombic outer branch potential can be successfully modelled at large R using truncated Rittner functions [8] valid for $R \geq 6.0$ Å, of the form,

$$V(R) = T_\infty + C_1/R \pm C_3/R^3 + C_4/R^4 + C_6/R^6 \qquad (5.9)$$

With the exception of the C_3 term, the values of the constants in equation 5.9 are the same as those used for the E-state in chapter 3. For the $D'2g$ state, the diagonal matrix element for the $I^+(^3P_{22})$ Russell-Saunders (RS) configuration $||1^+1^-0^+\underline{1}^+||$ is $-1/5Q$ where $Q = e^2\langle\rho^2\rangle_+/4\pi\epsilon_0 R_{AB}^3$. The Rittner coefficients used for the $D'2g$ state in these studies are $C_1 = -1.16141\times10^5$, $C_3 = -4.34\times10^4$, $C_4 = -5.57\times10^5$ and $C_6 = 1.0\times10^6$. The attractive branch was calculated between 6.0–13.0 Å and these points were splined smoothly on to Tellinghuisen's RKR potential valid up to v'=30.

The form of the repulsive branch can be adequately represented by the function,

$$V(R) = AR^n e^{-\beta R} \tag{5.10}$$

or

$$\ln V(R) = \ln A + n\ln R - \beta R \tag{5.11}$$

A, n and β were determined by solving a set of three simultaneous equations using three knot points, $V(R_n)$ where n=1–3. $V(R_1)$ was fixed throughout at the inner turning point of the v'=30 level ($V(R_1)$=43371.1 cm^{-1}, R_1=3.155103 Å) of Tellinghuisen's RKR data. The $V(R_2)$ and $V(R_3)$ knot points were positioned above and below the energy range of the observed vibrational levels and their positions were varied until the form of the repulsive branch reproduced the set of unperturbed ion-pair eigenvalues between 57281–58654 cm^{-1}.

Initially, the $V(R_2)$and $V(R_3)$ knot points were chosen so that the inner branch passed through the minimum of the $[^2\Pi_{3/2}]5d : 2g$ Rydberg state and to the left of the inner branch of the higher lying $[^2\Pi_{3/2}]7s : 2g$ Rydberg state. The form of this repulsive branch was based on experimental observations which indicated that strong interactions between the former (but not the latter) Rydberg state and the $D'2g$ ion-pair state took place.

However, the gradient of the repulsive branch was too low and did not reproduce the correct eigenvalues over the whole range of unpertubed levels. Because the C_4 term used in the attractive branch was already at its minimum value the correct eigenvalues could only be reproduced by increasing the gradient of the repulsive branch using the following knot points,

$V(R_1)$=43371.1 cm^{-1}, R_1=3.155103 Å
$V(R_2)$=55000.0 cm^{-1}, R_2=2.730 Å
$V(R_3)$=70000.0 cm^{-1}, R_3=2.495 Å.

The resulting A, n and β values, 575281.5 cm^{-1}, –10.9729138 and –3.1767724 Å^{-1} respectively, when substituted into equation 5.10 produces the final repulsive

branch, shown in figure 5.2 which was splined smoothly on to Tellinghuisen's RKR potential. The experimental energies of the vibrational levels agree to within ±2 cm^{-1} compared to the levels supported by our calculated $D'2g$ potential energy curve. The absolute numbering of these levels corresponds to $v'=n+267$.

Although the attractive and repulsive branches smoothly join on to the lower RKR points of Tellinghuisen, their absolute positions do not represent a unique fit for the $D'2g$ state. Bearing in mind that the lateral distance between turning points for a particular energy must be conserved in order to maintain the correct eigenvalues, the effect of varying the C_4 term of the attractive branch on the repulsive branch is briefly investigated.

The uncertainty in the C_4 term arises from the uncertainty of the polarisability of I^+, 2 $Å^3 \leq \alpha_{I^+} \leq 4$ $Å^3$. At $V(R_c)$=58954 cm^{-1} the lateral displacement between these two possible attractive limbs is ~0.012 Å or a vertical energy displacement of ~18 cm^{-1} at 8.9 Å. The contributions to the energy of the attractive branch from the C_3, C_4 and C_6 coefficients are –62, –89 and –2 cm^{-1} respectively at R=8.9 Å. The ratio of the gradient of the repulsive branch of the potential at this energy to that of the attractive branch is ~ –37.

The knot points for the extended $D'2g$ ion-pair state between 2.35–13.00 Å are shown in table 5.2 and plotted in figure 5.3.

R/Å	V/cm^{-1}	R/Å	V/cm^{-1}
2.30	92019.09	4.30	43191.26
2.40	79254.98	4.40	43784.01
2.50	69575.42	4.50	44391.03
2.60	62160.70	5.00	47460.20
2.70	56445.69	5.50	50146.22
2.80	52033.99	6.00	52159.69
2.90	48643.61	6.50	53817.63
3.00	46071.70	7.00	55210.31
3.10	44239.77	7.50	56398.96
3.20	42694.01	8.00	57426.82
3.30	41565.83	8.50	58325.38
3.40	40862.14	9.00	59118.21
3.50	40493.69	9.50	59823.37
3.60	40388.05	10.00	60454.92
3.70	40485.16	10.50	61024.02
3.80	40736.66	11.00	61539.65
3.90	41104.06	11.50	62009.12
4.00	41555.00	12.00	62438.43
4.10	42065.37	12.50	62832.58
4.20	42615.89	13.00	63195.78

Table 5.2. Knot points used to generate the extended $D'2g(^3P_2)$ state potential curve.

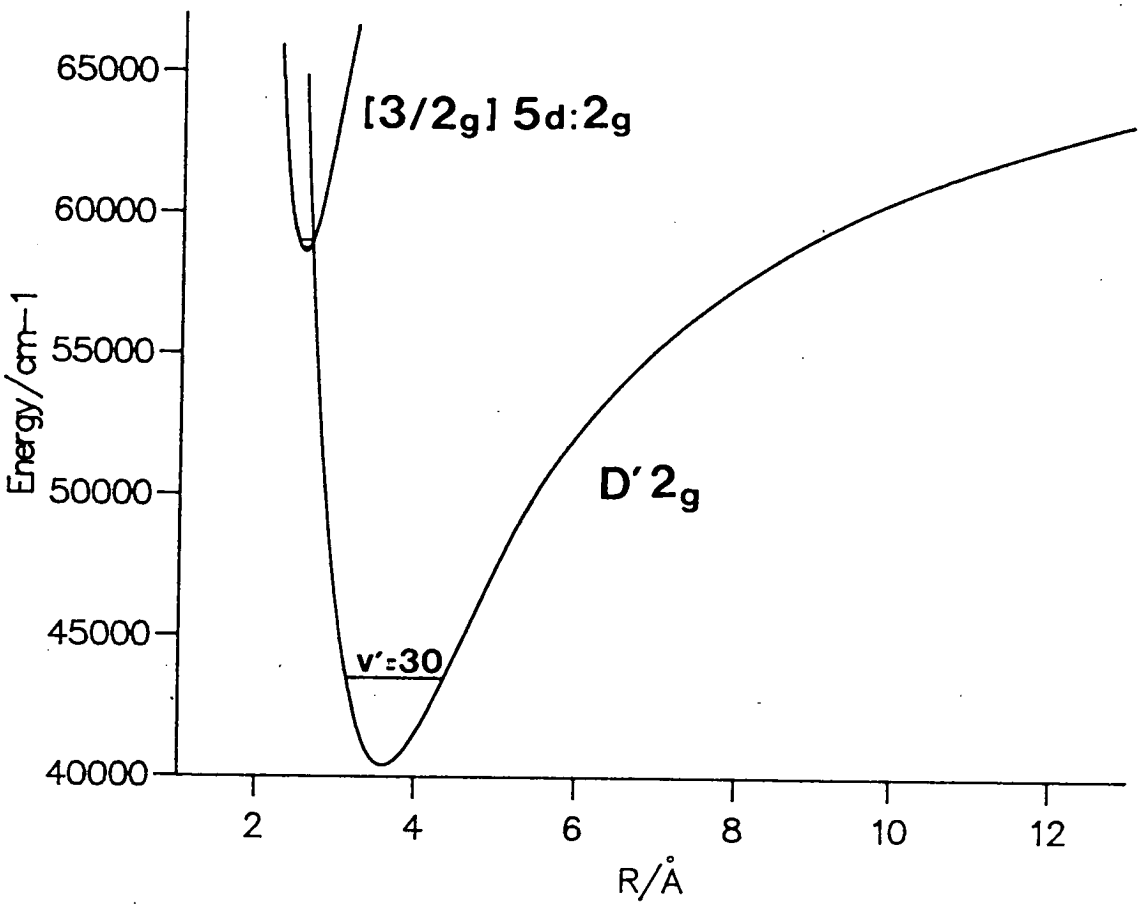

Figure 5.3. The generated $D'2_g$ ion-pair and $[^2\Pi_{3/2}]5d : 2g$ Rydberg states.

5.5 Generation of the $[^2\Pi_{3/2}]5d : 2g$ Rydberg State

The Rydberg state potential energy curves of I_2 determined from experiment are generally not well studied because many of them are strongly predissociated. In general, the form of the curves around T_e will be similar to those of the lowest energy ground state molecular ion core, $I_2^+[2430]^2\Pi_{3/2}$, $^2\Pi_{/2}$. The Rydberg state used in this analysis was generated from a Morse potential of the form,

$$V(R)^{Morse}/hc = D_e[1 - exp[-\beta(R - R_e)]]^2 \tag{5.12}$$

where

$$\beta = (2\pi^2 C\mu\omega_e^2/D_e h)^{1/2} = 0.12177881(\mu\omega_e^2/D_e)^{1/2}\ \mathring{A}^{-1}. \tag{5.13}$$

D_e is the dissociation energy of the state calculated from a knowledge of the Rydberg state dissociation limit, T_∞ and the term value, T_e. Since Rydberg states of I_2 correlate with one ground and one excited state atom, $I(^2P_{3/2},^2P_{1/2})+I^+(^3P,^1D,^1S)nl$, T_∞ was determined relative to the potential minimum of the ground state using the atomic excitation scheme, $I(^2P_{3/2})+I(^2P_{3/2})\rightarrow I(^2P_{3/2})+I^+(^3P_2)5d$. The lowest energy $5d$ Rydberg series of atomic iodine which converges on the $I^+(^3P_2)$ ion has an origin at ~67298.45 cm^{-1} [9]. The ground state dissociation energy of I_2 is 12547.2 cm^{-1}.

Successful modelling of the coupled ion-pair/Rydberg system in the diabatic representation presented in the next section required T_e of the $[^2\Pi_{3/2}]5d : 2g$ Rydberg state to be fixed at 58605 cm^{-1} and therefore D_e=T_∞-T_e=79846-58612=21234 cm^{-1}.

From (2+1) REMPI studies, a rotational contour and vibrational structure analysis of Rydberg states relatively free from perturbations have been carried out by Kvaran et al. [10] on the $[^2\Pi_{3/2g}]5d : 1g$ state and the lower energy $[^2\Pi_{1/2g}]6s : 1g$ Dalby system. The same ω_e and R_e values determined for these states, ~240 cm^{-1} and 2.56 Å respectively were used in our calculations. In comparison, for I_2^+, ω_e=240 cm^{-1} and R_e=2.59 Å.

5.6 Two-State Coupling Calculations

In this section, the results of the two-state interaction calculations are presented. In particular, the effects of the coupling between the Rydberg and ion-pair state as a function of T_e^{Ryd}, R_e^{Ryd} and H_{12}^{el} are discussed in terms of the vibronic energies and peak intensities of the coupled state levels.

Mass analysed (2+1) REMPI studies provide an insight into the competition between the I^+ and I_2^+ ionisation channels as a function of the photon energy, showing the extent of ion-pair or Rydberg character in the observed vibronic levels of the coupled system. In the ionisation step from a Rydberg state both I_2^+ and I^+ ions are observed because energetically, the I_2^+ threshold is reached in the (2+1) step and absorption by a further photon to a repulsive state of the ion then dissociates to I + I^+. In contrast, ionisation from an ion-pair state yields only I^+ ions. The most favourable FC factors in the ionisation step are provided by the outer turning points which for the $D'2g$ state at ~60,000 cm^{-1} corresponds to R_{outer} ≈9 Å as shown in figure 5.1. At such large R, the threshold of the I + I^+ dissociation products correlating with I_2^+ is reached by the absorption of a further two-photons via the dense manifold of repulsive Rydberg states. The I_2^+ mass analysed (2+1) REMPI spectrum in figure 5.4 shows the extent of mixing of Rydberg character amongst the ion-pair levels. The strong peak observed at v'=312 is predominantly of Rydberg character and is assigned as the v'_{Ryd}=0 level.

Figure 5.2 shows that the repulsive limb of the $D'2g$ ion-pair state crosses the $[^2\Pi_{3/2}g]5d : 2g$ Rydberg state at R_c=2.65 Å, close to the outer turning point of the v'=1 Rydberg level. The overlap integral $\langle v'_{Ryd} = 0 | v'_{i.p} \rangle$ and therefore the coupling of these levels will be small.

Initially, T_e^{Ryd} and H_{12}^{el} were adjusted to reproduce the observed vibronic energies around v'=312 (v'_{Ryd}=0). Because an increased energy separation between the v'=312 and v'=311 levels at zero coupling can be compensated for by a lowering

in the H_{12}^{el} value, there were no unique values of T_e^{Ryd} and H_{12}^{el} which reproduced the spectrum in this region. However, for H_{12}^{el} >250 cm^{-1} these two interacting levels are pushed too far apart, beyond the observed 12 cm^{-1} energy separation. Although the positions of the vibronic energy levels in the lower part of the spectrum can be correctly reproduced using a value of H_{12}^{el} <250 cm^{-1}, the positions of the higher energy levels beyond v'=312 compare badly with experiment. On average, the ΔG_v values in this region are generally too large (~26–27 cm^{-1}) compared with the observed values (~25 cm^{-1}) suggesting the present value of H_{12}^{el} is too low.

Therefore, in order to increase H_{12}^{el} beyond 250 cm^{-1} and still maintain the correct positions of the lower vibronic levels, the idea of a simple first-order repulsive interaction between the v'=312 (v'_{Ryd}=0) and v'=311 levels was rejected in favour of a scheme whereby at zero coupling, T_e^{Ryd} is increased so that v'_{Ryd}=0 was positioned 8 cm^{-1} above the v'=312 ion-pair level. When H_{12}^{el} is increased to ~400 cm^{-1} v'=312 is pushed towards v'=311 by the v'=313 (v'_{Ryd}=0) level, the eigenvalues of the lower vibronic levels are correctly reproduced. In addition, the range of ΔG_v values of the observed higher levels were also reproduced.

From the I_2^+ mass-analysed (2+1) REMPI spectrum shown in figure 5.4, the intensity of the v'=312 and 311 levels are in the approximate ratio 60:40 which is a measure of the percentage of Rydberg character in each level and compares favourably with our calculated ratio of 58:25 shown in table 5.3b.

Finally, the absolute positions of the strongly perturbed higher lying levels were reproduced by decreasing the value of ω_e of the Rydberg state from 244 to 224 cm^{-1} which requires a corresponding increase in T_e^{Ryd} in order to maintain the same absolute position of the v'^{Ryd}=0 level at zero coupling. The calculated energy levels are shown in Table 5.3a and 5.3b. The parameters used in the final fit are ω_e=230±10 cm^{-1}, H_{12}^{el}=450±100 cm^{-1} and R_e^{Ryd}=2.56±0.02 Å.

For H_{12}^{el} values below ~350 cm^{-1} although the positions and % Rydberg character of the levels around v'_{Ryd}=0 can be correctly reproduced, a poor fit is obtained

for the higher levels whose ΔG_v values are on average too large. In contrast, for H_{12}^{el} values above ~550 cm^{-1} the calculated eigenvalues for the levels below v'=313 compare poorly with experiment since they are all forced down in energy by the v'_{Ryd}=0 level (obs–calc values decrease towards lower energies as the interaction decreases). In addition, the % Rydberg character observed for the v'=312 and 311 levels has become too dispersed.

A lateral displacement of $R_e^{Ryd} \geq +0.02$ Å results in a rapid increase in the $\langle v'_{Ryd} = 0 | v'_{i.p} \rangle$ overlap integral, requiring a H_{12}^{el} to decrease below 350 cm^{-1} in order to reproduce the correct eigenvalues of levels around $v'^{(v=0)}_{Ryd}$. However, as mentioned previously this value of H_{12}^{el} cannot reproduce the higher energy levels. No change in the parameters could calculate the observed energy of the v'=322 level where an obs–calc value remains at $\sim +5$ cm^{-1}.

The observed peak intensities can be considered to be the product of three factors, the Franck-Condon factors (FCF) for excitation to the Rydberg/ion-pair state from the ground state, $\langle v'_{g.s} | v'_{Ryd/i.p} \rangle$, a vibrational overlap term, $\langle v'_{Ryd} | v'_{i.p} \rangle$, which determines the efficiency of the coupling between the Rydberg and ion-pair states and finally the efficiency of the ionisation step. For the first factor, the relative efficiency of the Ryd:i.p excitation was set to 100:1. At lower ratios the calculated intensities do not reproduce the experimental ones and at a higher ratios the calculated intensities do not change significantly. From previous studies, we concluded that excitation from the ion-pair rather than the Rydberg states provides a more efficient ionisation step. This observation is again borne out in these studies. From figure 5.1, the intensities of the set of weakly coupled levels between v'=300-310 are similar in magnitude to the strongly coupled levels between v'=315-323, but in contrast, the ratio of the % Rydberg character is $\sim$ 1:15 respectively. Assuming the latter set of levels are relatively free from predissociation, then clearly the efficient excitation to Rydberg states in the first step is being cancelled by the ionisation step which favours excitation from the ion-pair states. The simulated peak intensities shown in figure 5.4 exclude this

latter step, which should have no significant effect on the positions of the intensity minima.

The positions of the intensity minima at v'=313/314, 324 and 336 are reproduced in the simulated spectrum shown in figure 5.5. Increasing ω_e^{Ryd} and R_e^{Ryd} by $\sim$5 cm^{-1} and $\sim$0.01 Å respectively, shifts the v'=336 intensity minimum peak by one level. The calculated energies of the v'=341–345 levels can be improved upon if H_{12}^{el} is increased to 450 cm^{-1} but this has the effect of lowering the position of the v'=336 intensity minimum peak by one level.

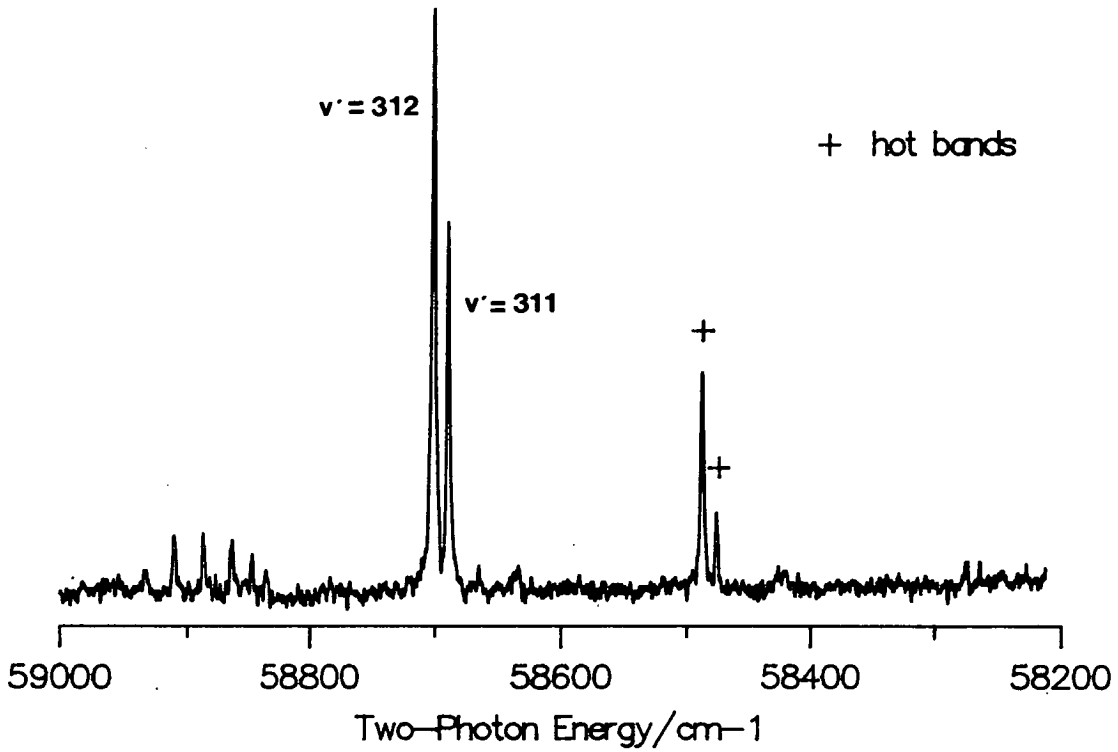

Figure 5.4. The (2+1) mass-resolved REMPI excitation spectrum of jet-cooled I_2 recorded by monitoring the I_2^+ mass channel.

v'	calc. $\tilde{\nu}$ (cm^{-1})	$\tilde{\nu}_{obs-calc}$ (cm^{-1})	% Ryd	$(FCF)^2$ $\times 10^{-3}$	v'	calc. $\tilde{\nu}$ (cm^{-1})	$\tilde{\nu}_{obs-calc}$ (cm^{-1})	% Ryd	$(FCF)^2$ $\times 10^{-3}$
267	57282.6	−1.6	0.05	0.272	287	57947.0	+1.0	0.11	0.706
268	57317.0	−2.0	0.05	0.284	288	57979.0	0.0	0.12	0.751
269	57351.2	−3.2	0.06	0.297	289	58010.8	−1.8	0.12	0.801
270	57385.4	−3.3	0.06	0.309	290	58042.5	+3.5	0.13	0.855
271	57419.4	−3.3	0.06	0.323	291	58074.1	+2.9	0.14	0.914
272	57453.2	+1.8	0.06	0.336	292	58105.6	+3.4	0.15	0.978
273	57487.0	−0.9	0.06	0.351	293	58137.0	+2.0	0.15	1.05
274	57520.6	−1.6	0.06	0.366	294	58168.2	+0.8	0.16	1.13
275	57554.1	−1.1	0.07	0.382	295	58199.3	+0.7	0.17	1.21
276	57587.5	−0.5	0.07	0.398	296	58230.3	+2.7	0.19	1.31
277	57620.8	−0.8	0.07	0.416	297	58261.2	+3.8	0.20	1.42
278	57654.0	−1.0	0.07	0.436	298	58292.0	+2.0	0.22	1.54
279	57687.0	0.0	0.08	0.457	299	58322.7	+1.3	0.23	1.68
280	57719.9	+0.1	0.08	0.479	300	58353.3	+1.7	0.25	1.84
281	57752.7	+0.3	0.09	0.504	301	58383.7	+2.3	0.28	2.03
282	57785.4	−0.4	0.09	0.530	302	58414.1	+0.9	0.31	2.25
283	57818.0	−1.0	0.09	0.559	303	58444.3	+1.6	0.35	2.53
284	57850.4	−1.4	0.10	0.591	304	58474.4	+2.6	0.39	2.87
285	57882.7	+1.3	0.10	0.626	305	58504.4	+0.6	0.46	3.32
286	57914.9	+1.1	0.11	0.664	306	58534.3	+2.7	0.55	3.91

Table 5.3a. Calculated vibronic energies and peak intensities.

v'	calc. $\tilde{\nu}$ (cm^{-1})	$\tilde{\nu}_{obs-calc}$ (cm^{-1})	% Ryd	$(FCF)^2$ $\times 10^{-3}$	v'	calc. $\tilde{\nu}$ (cm^{-1})	$\tilde{\nu}_{obs-calc}$ (cm^{-1})	% Ryd	$(FCF)^2$ $\times 10^{-3}$
307	58564.1	+1.9	0.69	4.76	328	59107.7	−3.7	10.09	11.5
308	58593.6	+2.4	0.95	6.10	329	59132.3	+1.7	14.35	23.8
309	58623.0	+3.0	1.58	8.78	330	59155.9	−0.9	15.76	27.5
310	58651.7	+2.3	3.82	15.6	331	59179.8	+0.2	12.89	15.9
311	58678.1	−0.1	24.94	52.7	332	59204.6	+0.4	9.27	7.88
312	58691.8	−1.8	57.62	59.3	333	59230.1	+1.9	6.62	4.12
313	58713.3	–	7.91	0.617	334	59256.1	+0.9	5.10	3.06
314	58741.3	–	2.97	1.20	335	59282.4	−0.4	4.59	0.881
315	58769.7	−2.6	2.45	3.84	336	59308.6	–	4.95	0.0971
316	58798.0	+2.0	2.78	7.01	337	59334.4	−2.4	6.26	0.228
317	58826.1	−0.1	3.95	11.9	338	59359.6	−1.6	8.97	4.92
318	58853.5	−2.5	6.90	20.0	339	59383.8	−0.8	13.89	16.30
319	58879.3	−3.3	13.93	36.6	340	59406.5	+1.5	18.93	36.2
320	58902.5	−3.5	23.32	49.9	341	59428.5	+4.5	16.51	43.6
321	58924.6	−1.6	20.86	31.7	342	59451.8	+5.2	10.12	34.6
322	58948.5	−5.5	11.39	11.3	343	59476.5	+1.5	6.13	1.16
323	58974.7	+0.3	6.51	2.19	344	59501.8	+8.2	4.06	20.3
324	59001.6	–	4.89	0.0612	345	59527.4	+5.6	2.94	17.1
325	59028.6	−1.6	4.72	0.361					
326	59055.4	−1.4	5.35	2.10					
327	59081.9	−2.9	6.92	5.44					

Table 5.3b. Calculated vibronic energies and peak intensities.

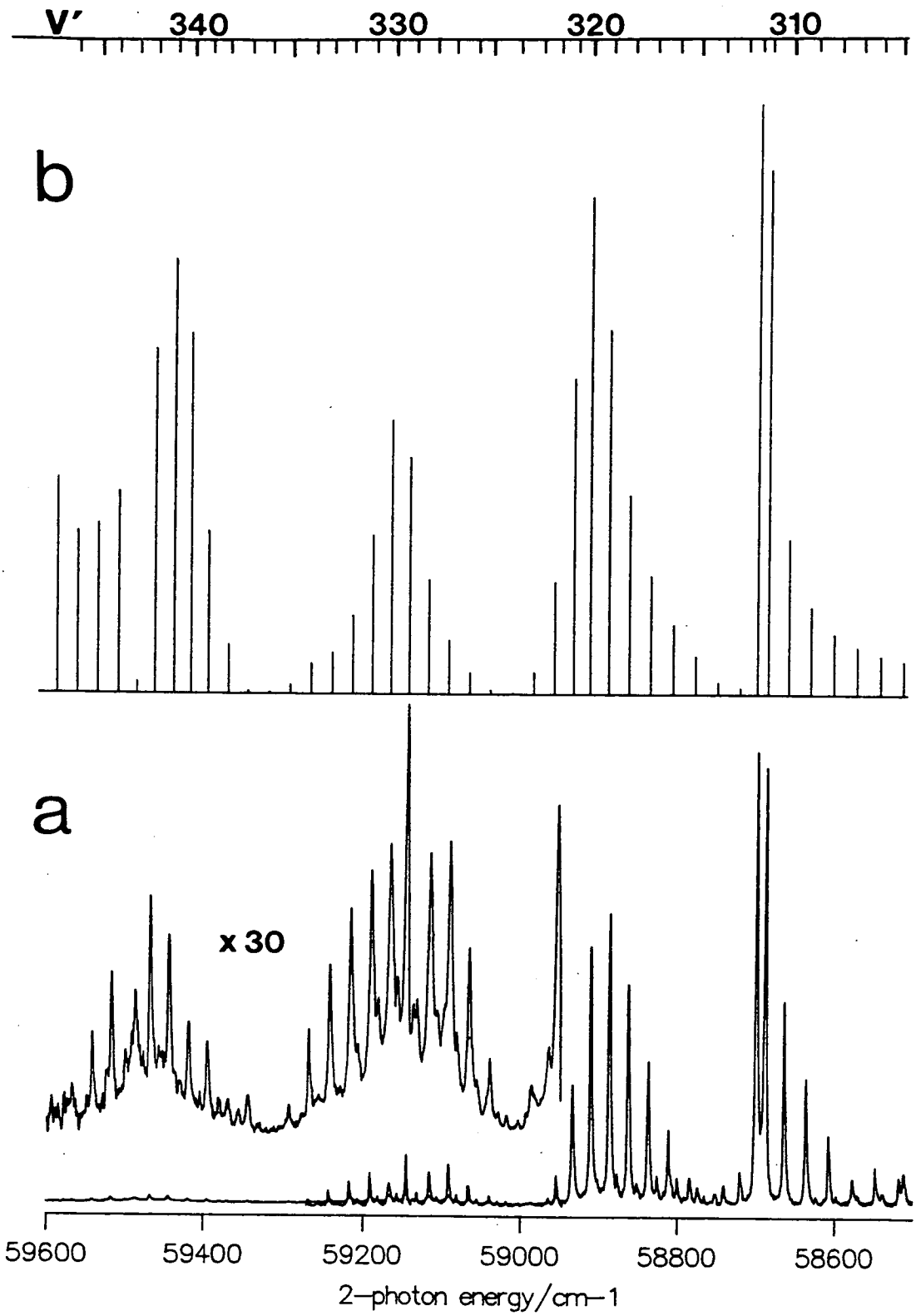

Figure 5.5. The observed (2+1) REMPI I^+ spectrum (a) and the simulated spectrum (b) between 58500-59600 cm^{-1}.

5.7 Discussion

The extent to which the crossings of states are avoided in homogeneous interactions ($\Omega_{Ryd} = \Omega_{i\text{-}p}$) varies widely. In chapter 2 we observed that the crossing of the $[^2\Pi_{1/2}]6s : 0_g^+$ Rydberg state by the $f0_g^+$ and $E0_g^+$ ion-pair states resulted in a strong and weak interaction respectively. The different extent of the vibronic coupling of the two states was shown to be a consequence of their electronic configurations.

In general, the magnitude of H_{12}^{el} will be large if the Rydberg and ion-pair states have the same spin multiplicity and differ in their orbital occupancies by either one or two electrons, where the greatest strength is associated with configurations that are connected by two parallel electron transfers ($\sigma \leftrightarrow \sigma$ or $\pi \leftrightarrow \pi$) between MOs. The single Mulliken configurations (which dominate at $R < R_e^{i\text{-}p}$) for the two interacting states, $D'[1432](^3\Pi_{2g})$ and $[[2430];^2\Pi_{3/2}]5d : 2g(^3\Pi_{2g})$ are both triplet in character and can be connected by a two electron transfer (one being a strong $\sigma \leftrightarrow \sigma$ valence electron transfer). In (2+1) REMPI studies the 5d Rydberg states are only observed when they are coupled with another state. When Ω=2 and ω_e=3/2 only 5dσ and 5dπ Rydberg states can be derived and since only one of these states has been observed by us in this energy region (they will be expected to lie close together in energy), we would expect the 5dσ Rydberg state to couple most strongly with the $D'[1432]$ state via two parallel electron transfers. A predicted medium/strong interaction is borne out by our calculated value for H_{12}^{el} of $\sim$400 cm^{-1}.

In comparison, Hoy et al. [11] in a rotationally resolved double resonance experiment observed a weak homogeneous interaction between high vibrational levels of the $F0_u^+$ ion-pair state ($v'_F \approx$200–250) and the $R0_u^+$ Rydberg state (v'_R=0–4). The interaction matrix element, W_{v_R}, which is a product of an overlap integral, $\langle v'_R | v'_F \rangle$, and the electronic matrix element W_e was observed to be large when v'_R is even and small for odd v'_R. This is a direct consequence of the alternation in

$\langle v'_R|v'_F\rangle$ since the inner branch of the F state crosses the R state at R_e^{Ryd} and passes through or near to a node in the odd v'_R vibrational wavefunctions. W_e was calculated to be 107±1 cm^{-1} which is ~1/4 times the strength of W_e calculated for our coupled system. The electronic configurations of the two interacting states are $F[2332]^3\Sigma^-_{0^+_u}$ and $[[2430];^2\Pi_{1/2}]6p\sigma_u : 0^+_u(^3\Pi_0)$. In the F state the spin vector must be anti-parallel to the axis to give m_s=0 needed to combine with Λ=0 to give a resultant 0^+ state. In the Rydberg state, the spin vector must be anti-parallel to the Λ=1 vector to give a resultant 0^+. In making the transition between a $^3\Sigma^-_{0^+}$ and $^3\Pi_{0^+}$ state, the spin vector has to be re-orientated ($\Delta m_s = \pm 1$) as well as Λ ($\Delta\Lambda\mp 1$). Although the latter is perfectly permissible with two photons (one parallel and one perpendicular transition), there is no way of re-aligning the spin with a photon. The transition is thus two-photon forbidden. As far as vibronic mixing is concerned, the coupling is through the $1/r_{12}$ term, which cannot change Λ or s. The $F[2332]$ and Ryd $6p_\sigma$ mixing is thus quite strongly forbidden and becomes weakly allowed through mixing of $F[2332]$ with $[1342]^3\Pi_{0^+_u}$ and $[2431]$ $^3\Pi_{0^+_u}$ (the B state).

5.8 References

1. K. P. Lawley and R. J. Donovan, *J. Chem. Soc. Farad. Trans.* **89**(1993)1885.

2. F. W. Dalby, M. H. L. Pryce, G. Petty-Sil and C. Tai, *Can. J. Phys.* **55**(1977)103.

3. R. J. Donovan, R. V. Flood, K. P. Lawley, A. J. Yencha and T. Ridley, *Chem. Phys.* **164**(1992)439.

4. M. C. R. Cockett, J. G. Goode, K. P. Lawley and R. J. Donovan, *Chem. Phys. Lett.* **214**(1993)27.

5. M. C. R. Cockett, J. G. Goode, R. R. J. Maier, K. P. Lawley and R. J. Donovan, accepted by *J. Chem. Phys.* **100**(1994).

6. *Perturbations in the Spectra of Diatomic Molecules*, H. Lefebvre-Brion and R. W. Field, Academic Press 1986.

7. J. Tellinghuisen, S. Fei, X. Zheng and M. C. Heaven, *Chem. Phys. Lett.* **176**(1991)373.

8. E. S. Rittner, *J. Chem. Phys.* **19**(1951)1030.

9. C. E. Moore, *Atomic Energy Levels* Vol III, NSRDS-NB535.

10. A. Kvaran, H. Wang and G. H. Johannesson, *Chem. Phys. Lett* (1994).

11. A. R. Hoy, S. M. Jaywant and J. C. D. Brand, *Mol. Phys.* **60**(1987)749.

Chapter 6

Electronic States of the H_2...HF Cluster

6.1 Introduction

Over recent years there has been considerable interest in both the experimental and theoretical aspects of van der Waals (VDW) and hydrogen-bonded interactions between small molecules [1]. A whole class of photoinitiated reactions in VDWs complexes are known and have been shown to proceed via a charge-transfer (CT) process [2] e.g $Hg...Cl_2 + h\nu \longrightarrow Hg^+...Cl_2^- \longrightarrow Hg^+Cl^- + Cl\cdot$. Consider also, the rare-gas dimer cations, Rg_2^+, which are stable species (e.g $D_e \approx 1eV$ [3]) and have been shown to form ionic complexes. For example, fluorescence to the ground state from the ion-pair state, $Xe_2^+I^-$, has been observed in the gas-phase where the possible structure of the excited state is probably transient between $Xe...Xe^+ + I^-$ ($D_{\infty h}$) and [Xe_2^+ ($^2\Sigma_u^+$) I^- (C_{2v}) [4].

Spectroscopic studies of CT processes in the halogen and interhalogen molecules is an active area of research here at Edinburgh. Recently, the vibrational term values in the ν_3 stretching mode of $Ar...I_2^*$ have been measured, where the Rydberg electron has been observed in the I 7s and 8s levels [5]. Chapters 2 and 4 of this thesis discuss some of the intramolecular CT ion-pair states of I_2 and ICl observed in multiphoton absorption spectroscopy.

Accurate, theoretical calculations of the potential energy surfaces of VDW type molecules are mainly limited by the size of their constituent atoms and for

this reason *ab initio* calculations on the H_2...HF complex which contain first row atoms only, can be performed quickly and accurately. A consideration of the potential energy surface of this complex, accessible in spin-allowed, vertical one and two-photon electronic transitions will provide a good theoretical basis for future spectroscopic experiments on VDW type molecules especially when considering the electronic excitation of a diatomic chromophore within the cluster. As a result of the light nuclei present in the H_2...HF system and the relatively shallow nature of the intermolecular potentials in such weakly bonding systems, large amplitude motion (LAM), small barriers to internal rearrangement and strong coupling between the rotational and vibrational modes can be investigated both experimentally and theoretically.

Anticipating our results, Rydberg states in particular will be expected to dominate the electronic spectra of this complex and for this reason, emphasis is given to these states together with their corresponding core states of the positive ion. Complementary to these studies is the increasing availability of spectroscopic data on the low vibrational levels of positive-charged clusters from zero kinetic energy photoelectron (ZEKE-PES) techniques [6], and the high lying Rydberg state levels obtained from jet-cooled TOF-REMPI studies [5].

Another objective in our studies is to determine which state(s) of H_2...HF correlate with the $H_3^+F^-$ proton transfer state and whether this state can be accessed spectroscopically from the ground state.

Wherever possible, the electronic states of the H_2...HF complex will be discussed using a purely classical model describing the intermolecular interaction between the H_2 and HF monomer units in terms of the molecular electrical fields resulting from the permanent and induced electrical multipoles. This interaction depends on the isolated monomer molecular charge distributions and on their multipole polarisabilities, hyperpolarisabilities, etc.

However, such a classical model, even if all infinite-order permanent and induced multipole moments are included, fails to take into account quantum effects

between the two monomers especially at intermediate and short range intermolecular distances where charge cloud overlap becomes significant. For example, exchange repulsion effects result in repulsive potential walls between the monomer molecules which prevents them from totally coalescing (the classical electrostatic model fails to prevent this). On the other hand, dispersion and charge-transfer processes are attractive and are largely responsible for keeping the monomer units together in the the form of a VDW complex. The former force can be considered as arising from an induced-dipole induced-dipole correlation of charge distributions between monomer units which lowers the energy, resuling in a binding force. This dispersion energy has a characteristic R^{-6} dependence and persists even at large R which reflects the relatively large intermolecular bond distances in VDW complexes. At very large R distances, the dispersion force becomes R^{-7} dependent due to a retardation effect in the response time between the instantaneously fluctuating dipoles on each monomer unit and hence the interaction falls of more rapidly [7]. As the intermolecular distance increases, the non-electrical interactions vanish first and the classical electrostatic contributions persist at long range.

6.2 *Ab initio* Methods for the Calculation of Molecular Wavefunctions

6.2.1 The Self-Consistent Field (SCF) Method

The electronic Schröedinger wave equation (SWE) [10] containing n-electrons and N nuclei given by

$$\left[\sum_{i=1}^{n} -\frac{h^2}{8\pi^2 m_e}\nabla_i^2 - \sum_{i=1}^{n}\sum_{\alpha=1}^{N}\frac{Z_\alpha e^2}{4\pi\varepsilon_0 r_{i\alpha}} + \sum_{i}\sum_{<j}\frac{e^2}{4\pi\varepsilon_0 r_{ij}}\right]\Phi(R,r) = E(R)\Phi(R,r) \tag{6.1}$$

where m_e is the mass of an electron and the summation indices i and α extend over electrons and nuclei respectively, can only be solved exactly for one-electron

systems and so for other systems approximate methods are adopted. Within the independent particle model (IPM), in which the electronic repulsion terms in equation 6.1 are omitted, the MO method generally provides the best description of the electronic structure of molecules near their equilibrium geometries (with the exception for example of the ion-pair states of the halogens discussed in chapter 1). The MO wavefunction can be separated into n one-electron wave equations of the form,

$$\hat{h}(i)\phi_i(r_i) = e_i\phi_i(r_i) \tag{6.2}$$

where $\phi_i(r_i)$ is a one-electron wavefunction or orbital for electron i, e_i is an orbital energy and $h(i)$ is a one-electron operator given by,

$$\hat{h}_i = -\frac{1}{2}\nabla_i^2 - \sum_{\alpha=1}^{N}\frac{Z_\alpha}{r_{i\alpha}} \tag{6.3}$$

The n-electron wavefunction can be separated into a product of n one-electron wavefunctions, $\phi_i(r_i)$,

$$\Phi(R, r_1, ..., r_n) = \phi_1(r_1)\phi_2(r_2)...\phi_n(r_n) \tag{6.4}$$

Each of the orbitals in equation 6.4 must be multiplied by either of the spin wavefunctions α or β corresponding to the $\frac{1}{2}h/2\pi$ and $-\frac{1}{2}h/2\pi$ components of the spin angular momentum respectively. From the Pauli principle, each orbital, ϕ_i, may only be occupied by a maximum of two electrons, one with α and the other with β spin. The resulting molecular wavefunction for an even electron molecule is most conveniently written as a single Slater determinant as shown below, which represents the wavefunction as a linear combination of all the possible $n!$ permutations of the indistinguishable electrons amongst the orbitals.

$$\Phi(R, r) = 1/\sqrt{(n!)}\begin{vmatrix} \phi_1(r_1)\alpha & \phi_1(r_1)\beta & ... & \phi_{n/2}(r_1)\beta \\ ... & ... & ... & ... \\ ... & ... & ... & ... \\ ... & ... & ... & ... \\ \phi_1(r_n)\alpha & \phi_1(r_n)\beta & ... & \phi_{n/2}(r_n)\beta \end{vmatrix}$$

where $1/\sqrt{(n!)}$ is a normalisation factor.

The neglected interelectronic interactions, which are far from negligible, are partially accounted for when the orbitals, ϕ_i, are calculated assuming that any one electron within the molecule moves in a potential which is a spherical average of the potential due to all the other n-1 electrons and the two nuclei. The Schroedinger wave equation for the electron is solved analytically for this potential, resulting in a new improved wavefunction for the electron which is then used in the calculation of the potential experienced by one of the other electrons, resulting in a refined average potential. This procedure is repeated for all the electrons and hence the potential experienced by the first electron can be recalculated. The whole cycle continues in an iterative manner until the solutions for all the electrons are unchanged in a threshold variational sense, resulting in orbitals which are self consistent by minimising the electronic energy E given by the expectation value,

$$E = \frac{\int \Phi^* \hat{H} \Phi d\tau}{\int \Phi^* \Phi d\tau} \tag{6.5}$$

where $d\tau$ represents intergration over all space and $\hat{H}$ is the Hamiltonian operator given by the terms in the square brackets in equation 6.1.

For normalised and mutually orthogonal orbitals which satisfy the conditions: $\int \phi_i \phi_j d\tau = \delta_{ij}$=1 and 0 if $i = j$ and $i = j$ respectively, the energy for a closed shell molecule with $n/2$ doubly occupied orbitals is given by:

$$E = \sum_{i=1}^{n/2} 2h_{ii} + \sum_{i=1}^{n/2} \sum_{j=1}^{n/2} (2J_{ij} - K_{ij}) \tag{6.6}$$

where h_{ii} is the one-electron energy given by,

$$h_{ii} = \int \phi_i(1)[-\frac{1}{2}\nabla_i^2 - \sum_{\alpha=1}^{N} \frac{Z_\alpha}{r_{1\alpha}}]\phi_i(1)d\tau_1 \tag{6.7}$$

where electron 1 has been arbitrarily assigned to orbital ϕ_i and $d\tau_1$ is an intergration with respect to the coordinates of electron 1. The second term in equation 6.6 is the contribution of the interelectron interactions to the energy from the Coulomb integral, J_{ij} given in equation 6.8, which describes the average electro-

static interaction between the two charge distributions $\phi_i(1)^2$ and $\phi_i(2)^2$.

$$J_{ij} = \int \phi_i(1)\phi_j(2)\frac{1}{r_{12}}\phi_i(1)\phi_j(2)d\tau_{12} \tag{6.8}$$

where $d\tau_{12}$ represents intergration with respect to the coordinates of electrons 1 and 2.

K_{ij}, the exchange integral given in equation 6.9 has no classical interpretation because it is a purely quantum mechanical correction which takes into account the effects of spin correlation.

$$K_{ij} = \int \phi_i(1)\phi_j(2)\frac{1}{r_{12}}\phi_i(2)\phi_j(1)d\tau_{12} \tag{6.9}$$

When the 'best' wavefunction is obtained by minimising the energy of equation 6.5, provided the orbitals remain mutually orthogonal, and following a considerable amount of algebra a set of coupled integro-differential equations as developed by Hartree [8,9] and improved by Fock are arrived at as shown in equation 6.10. These equations can only be solved by an iterative method since the Coulomb and exchange operators defined in equations 6.8 and 6.9 respectively are defined in terms of the orbitals ϕ_i.

$$\hat{F}_i(1)\phi_i(1) = \varepsilon_i\phi_i(1) \tag{6.10}$$

where $\hat{F}_i$ is the Fock operator given by:

$$\hat{F}_i(1) = \hat{h}(1) + \sum_j (2\hat{J}_j(1) - \hat{K}_j(1)) \tag{6.11}$$

where $\hat{h}(1)$ is the one-electron operator for electron 1 given by:

$$\hat{h}(1) = -\frac{1}{2}\nabla_1^2 - \sum_{\alpha=1}^{N}\frac{Z_\alpha}{r_{1\alpha}} \tag{6.12}$$

The spherical symmetry of atoms means that the Hartree-Fock equations can be solved numerically giving the atomic orbitals, ϕ_i, which can be used to produce the best atomic wavefunction represented by a Slater determinant. However, for molecules, due to their lower symmetry, this procedure is not possible and as a

consequence, Roothaan [11] suggested that the MOs, ϕ_i, are formed from a linear combination of m basis functions $\{\chi_q\}$:

$$\phi_i = \sum_{q=1}^{m} C_{iq}\chi_q \tag{6.13}$$

The MOs, ϕ_i, provided a large enough basis set is used, should approach those obtained in the Hartree-Fock limit if equation 6.10 could be solved directly.

The electronic wavefunctions for open shell molecules are considerably more complicated than for closed shell ones because in order to obtain a wavefunction which has the correct symmetry and for which the total spin angular momentum has a well defined value, a linear combination of Slater determinants is required to describe the final wavefunction.

In the restricted Hartree-Fock (RHF) method as derived by Roothaan [12], the open-shell SCF wavefunction contains orbitals which can be either doubly or singly occupied and the energy expression is given by:

$$E = 2\sum_{k} H_{kk} + \sum_{k}\sum_{l}(2J_{kl} - K_{kl}) + f[2\sum_{m} h_{mm} + f\sum_{m}\sum_{n}(2aJ_{mn} - bK_{mn}) + 2\sum_{k}\sum_{m}(2J_{km} - K_{km}) \tag{6.14}$$

where the indices k, l and m, n represent the doubly-occupied closed shell and the partially-occupied orbitals of the open shell respectively. f, a and b are independent coefficients whose values depend on the molecule in question. The first two terms represent the closed shell contribution to the energy whilst the third and fourth terms are the open-shell contributions and the last term constitutes the interaction between the closed and open-shell orbitals.

By relaxing the requirement that the value of the total spin angular momentum should be well defined a simpler form of the open-shell SCF wavefunction can be obtained by allowing the orbitals for the α and β electrons to be defined by two separate Fock matrices. This method constitutes the unrestricted Hartree-Fock (UHF) method where optimisation of the final wavefunction is much more straightforward than for the RHF case since it is analogous to the closed shell case.

6.2.2 Electron Correlation

The SCF Hartree-Fock method only partially takes into account interelectron repulsion because it averages any instantaneous distortions produced by neighbouring electrons, over the whole orbital and although the SCF scheme adequately describes most of the contributions to the intermolecular interaction energies including polarisation, CT and higher order exchange effects, it fails to take into account correlation energy (CE).

Configuration interaction (CI) methods provide a convenient technique to account for these instantaneous electron correlations and also provides a correct description of the dissociation behaviour of the wavefunction. By describing the molecular wavefunction, Φ, as a superposition of wavefunctions corresponding to different electronic configurations, Φ_I, where $\Phi = \sum_I C_I \Phi_I$, an improved description of the wavefunction is obtained by optimising the coefficients, C_I, in a variational calculation using equation 6.5. If the SCF or RHF wavefunction, Φ_0, is a reasonable approximation to the wavefunction then we may limit the configuration list to single and double excitations only because there is no direct interaction between states differing by more than two electron spin orbitals. Furthermore, for closed shell molecules, Brillouin's theorem states that no singly excited states can interact with Φ_0 and can therefore be neglected, but for open shell molecules they are very important and must be included in the configuration list.

A variety of techniques are available to account for EC, the most common ones include multi-configuration (MC-SCF) [13,14,15], Moller-Plessett perturbation theory [16], many-body perturbation theory [17] and coupled cluster methods [18] etc, but for our purposes, the multi-reference single and double excitation CI (MRDCI) technique is used [19]. This method produces an energy lowering in a secular equation following initial configuration selection by adding a test configuration to a series of dominant configurations, where those configurations producing an energy lowering below a given threshold are not included in the final secular equation. The combined effect of these neglected species on the energy lower-

ing are determined separately using an approximate extrapolation method which estimates the energy that would be obtained if a full configuration space were used.

6.2.3 The H_2..HF Cluster

Bernholdt et al. have carried out extensive calculations on the H_2..HF dimer, providing structural, bonding and vibrational frequency shift information suggesting a T-shaped (C_{2v}) equilibrium structure [20]. This has also been confirmed in studies by Andrews using infra-red (IR) matrix isolation techniques [21]. Such studies indicate that the H_2..HF dimer has a relatively large well-depth of about 120 K as compared to other VDWs complexes (due to the relatively large dipole-quadrupole interaction between the monomer units), allowing the intermolecular potential to be investigated by a variety of spectroscopic techniques. In recent years, IR studies have been used in many respects, but surprisingly, microwave studies have been neglected where rotational fine structure may be resolvable due to the relatively large rotational energy level spacings in H_2 and HF.

I.R studies indicate how a shift in the intramolecular vibrational frequency resulting from formation of the complex gives an approximate measure of the change in the well-depth of the intramolecular potential upon vibrational excitation [20]. I.R excitation of the HF vibrational mode results in a reduction of the VDW bond length as a result of increased dipole-induced dipole attractions. Because the intermolecular potential is relatively shallow, vibrational predissociation often accompanies vibrational excitation producing homogeneous line broadening via non-resonant coupling of the intermolecular and excited intramolecular vibrations.

I.R Stark measurements [22] provide information on the wide amplitude bending motion of HF within the complex, suggesting that the dipole moment, μ_z, of the complex is less than μ_z(HF) monomer, resulting from the average projection of the μ_z(HF) along the principle symmetry axis. Complete free rotation of the

HF subunit resulting from the wide amplitude bending motion (even with zero point vibrational motion) is prevented due to the anisotropy of the intermolecular potential. Such behaviour is confirmed from differential scattering experiments by Miller et al. [23].

The literature provides no evidence for any studies on the excited electronic states of the H_2..HF dimer. *Ab initio* calculations on the intermolecular forces of the ground state of the complex have been carried out notably by Bernholdt et al. [20] and Lischka [24], both of which provide a breakdown of the various contributions of the classical electrostatic interactions to the SCF and correlation energies where the largest contributors in stabilising the H_2..HF complex are the dipole(HF)-quadrupole(H_2) (d-q) and quadrupole-quadrupole (q-q) interactions. Quantitatively, the electrical contributions to the well depth are shown to be 120, 97, 42 and 126 cm^{-1} for the d-q, q-q, other permanent and induced moments respectively.

6.3 *Ab Initio* Calculations

The General Atomic and Molecular Electronic Structure System (GAMESS) suite of *ab initio* programs [25] was used to investigate the H_2..HF and $[H_2..HF]^+$ potential energy hypersurfaces in the regions of their respective equilibrium geometries. The wavefunctions generated at each point on the surface were calculated at the Hartree-Fock-Roothaan SCF [8,9] and MRDCI [19] levels.

The relatively large basis set employed consisted of a triple-zeta (TZ) Dunning contracted Huzanaga (10s6p/5s3p) and (5s/3s) basis on the fluorine and hydrogen atoms respectively. Split polarisation functions on each nuclear centre were supplemented with a diffuse s and p basis. These additional functions beyond the TZ set are summarised in table 6.1.

In C_{2v} symmetry, the resulting molecular orbital space comprises a total of 54 functions. At the CI level, the core 1s orbital on fluorine is frozen and the two

highest energy unoccupied molecular orbitals are discarded. The remaining 51 active orbitals are partitioned into 24 functions of A_1 symmetry, 9 of B_1, 15 of B_2 and 3 functions of A_2 symmetry. In order to accurately calculate the first five roots of a particular symmetry on the potential energy surface, between 30–50 main reference configurations were required. At a selection threshold of 10 μhartrees between 12,000–18,000 selected symmetry adapted functions (SAFs) were obtained from an initial list of $\sim$ 600,000 configurations generated from single and double excitations only.

A similar procedure was employed for calculations on the $[H_2..HF]^+$ dimer. In this case, the basis set contained no diffuse p-functions on any of the three hydrogen atoms. The resulting 45 active basis functions were grouped into 24 functions of A_1 symmetry, 7 of B_1, 12 of B_2 and 2 functions with A_2 symmetry. About 30 main configurations were required to accurately calculate the first five roots of the cation resulting in $\sim$ 6000–10,000 selected SAFs, using a selection threshold of 10 μhartrees.

Nuclear centre	exponents of uncontracted functions		
	s	p	d
H	0.01	0.35 1.40 0.01	
F	0.02	0.35 1.40 0.02	0.5 2.00

Table 6.1. Summary of additional functions beyond the TZV basis set.

6.4 Results

6.4.1 The Ground $^1A_1$ State of H_2...HF

Due to the large number of degrees of freedom on the potential energy hypersurface of the H_2...HF dimer we have restricted our studies to a T-shaped C_{2v} geometry whose parameters are defined in the figure 6.1. *Ab initio* calculations performed by Bernholdt et al. [20] and Lischka [24] determined this to be the minimum energy configuration and experimental confirmation for this is provided by Lovejoy et al. [26] from the vibration-rotation spectrum of ortho H_2...HF and from the work of Andrews, involving infra-red matrix isolate studies [21].

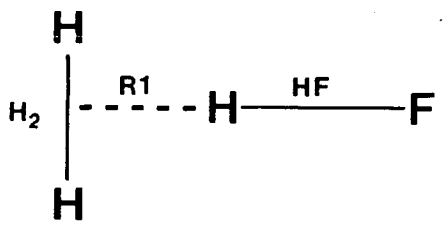

Figure 6.1. The parameters of H_2...HF for a T-shaped C_{2v} geometry.

In the search for energy minima the H_2 and HF coordinates have been varied individually and in a concerted manner, but no attempt was made to vary the angular coordinates.

In the discussion that follows, the subscripts v and d correspond to valence and diffuse type orbitals respectively.

GAMESS geometry optimisation procedures [25] resulted in a minimum energy configuration with a total energy of –101.196 hartrees (E_h) (1 E_h=27.212 eV) at the SCF level, corresponding to values of 2.338 Å, 0.898 Å and 0.735 Å for the R1, HF and H_2 bond lengths respectively. However, SCF calculations alone are inadequate in accurately describing VDW type interactions because only at the CI

level are long range intermolecular dispersion effects and changes in intramolecular monomer correlation taken into account. MRDCI calculations result in an improved equilibrium geometry of 2.330 Å, 0.910 Å and 0.735 Å for R1, HF and H_2 respectively, corresponding to a total energy of -101.463 E_h. At this geometry, about 95% of the final CI wavefunction is composed of the SCF MO basis whose bonding characteristics are shown in table 6.2. *Ab initio* calculations performed using a double substitution coupled cluster technique by Bernholdt et al. [20], employing a similar size basis to ours, resulted in equilibrium bond lengths of 1.914 Å, 0.9263 Å and 0.7432 Å for R1, HF and H_2 respectively. It is noticeable that the intermolecular distance, R1, is ~0.4 Å smaller than in our calculations.

MO N°	Orbital Occupancy	Energy (E_h)	Bonding Character
$1A_1$	2.0	-26.289	F(1s)
$2A_1$	2.0	-1.604	F(2s)
$3A_1$	2.0	-0.773	HF(σ)
$1B_1$	2.0	-0.647	F($2p_x$)
$1B_2$	2.0	-0.647	F($2p_y$)
$4A_1$	2.0	-0.627	H_2(σ_g)

Table 6.2. The SCF molecular basis at the [H_2...HF] equilibrium geometry.

Variation of the HF Coordinate

The SCF $^1A_1$ ground state potential energy curve generated by varying the HF bond only is shown in figure 6.3a and the resulting SCF dipole moment, (μ_z^{SCF}), directed along the C_2 symmetry axis is shown in figure 6.3b. Due to the partial ionic character of HF in the complex, μ_z^{SCF} initially increases as the HF bond stretches, simply as a result of the increased separation between $H^{\delta+}$... $F^{\delta-}$ and beyond R_{HF} ~1.5 Å the gradient of μ_z^{SCF} increases slightly and continues to rise as the H-atom of HF approaches H_2. However, analysis of the SCF eigenvectors indicates that the bonding character of HF within the complex becomes more covalent

as its bond length increases and as a consequence, $d\mu/dz$ is expected to decrease with increasing covalent character because μ_z^{SCF} becomes more dependent on the polarisation of two neutral atoms. However, the onset of significant CT effects, particularly beyond R_{HF} ~1.5 Å, increases the effective charge separation, confirmed by considering the change in μ_z^{SCF} of isolated HF following complexation with H_2, where μ_z^{SCF}(isolated HF)=1.897 D and μ_z^{SCF}(H_2...HF)=2.000 D with HF fixed at R_e=0.867 Å.

The CI potential curve of the ground $1\,^1A_1$ state of H_2...HF as a function of the HF coordinate is shown in figure 6.2. The calculated ω_e value of 4344.2 cm^{-1} compares with the theoretical value for isolated HF of 4136.0 cm^{-1} obtained by Bernholdt et al. [20], indicating that the fundamental vibrational frequency of HF increases on complexation with H_2.

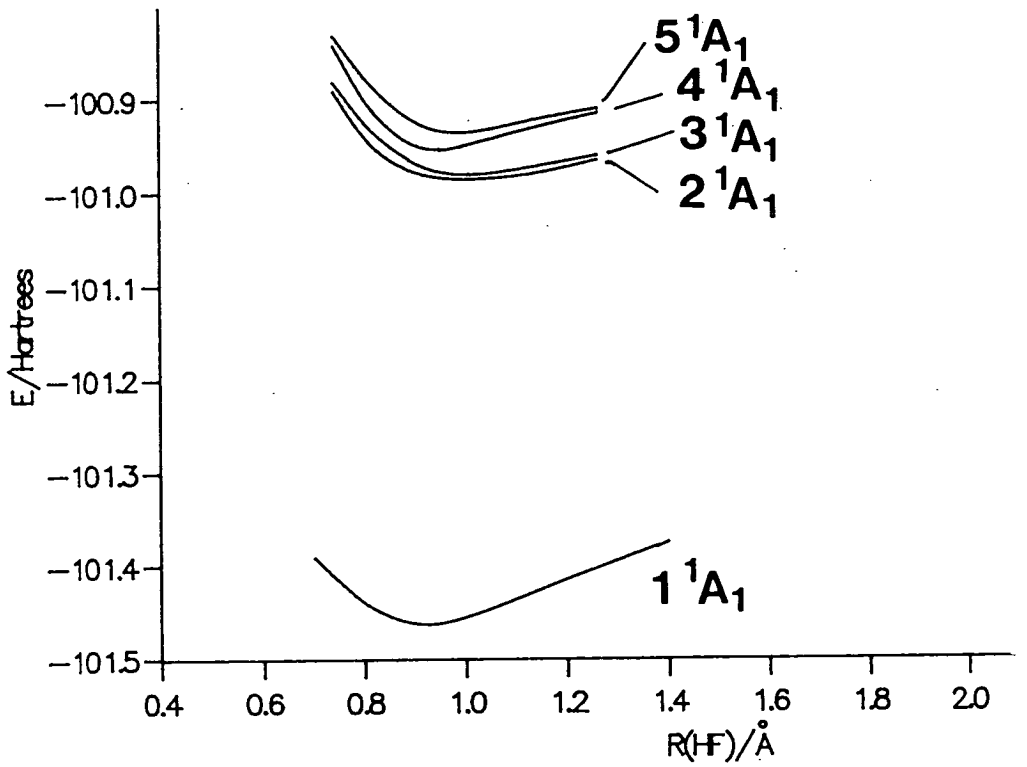

Figure 6.2. The $^1A_1$ state potential curves of H_2...HF as a function of R(HF).

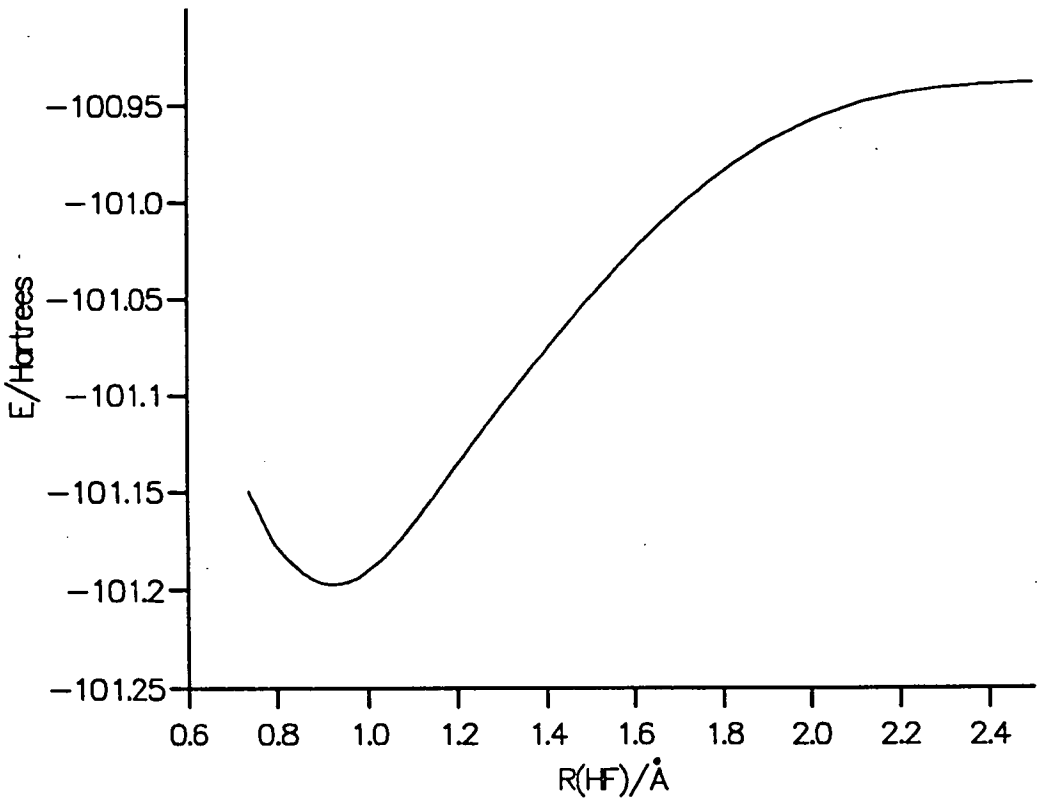

Figure 6.3a. The SCF $^1A_1$ ground state potential curve.

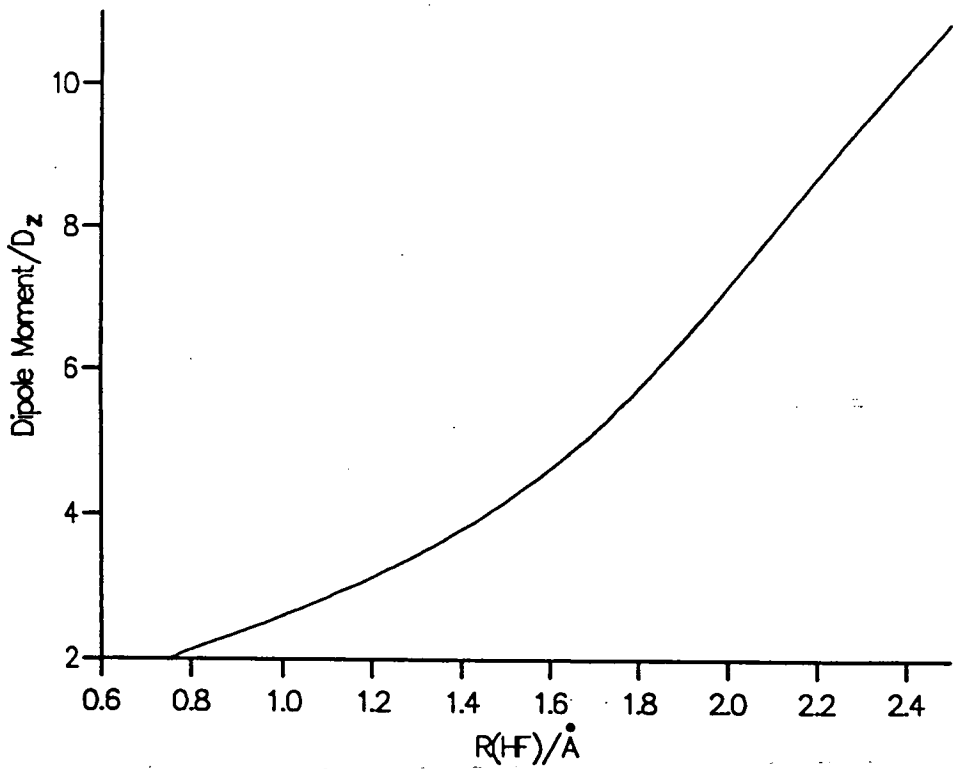

Figure 6.3b. The calculated SCF dipole moment, μ_z, as a function of R(HF).

Variation of the H_2 coordinate

The ground $^1A_1$ state potential curves resulting from a variation in the H_2 coordinate only are shown in figure 6.4 for two different regions of the hypersurface. The dashed curves represents the potential surfaces generated at fixed HF and R1 bond lengths of 2.27 Å and 1.00 Å respectively whilst the full curves were generated by fixing the HF and R1 coordinates at their global minimum equilibrium distances of 0.94 Å and 2.33 Å respectively. There are two important points to note. Firstly, at the CI level, the H_2 bond lengths at the minima of both sets of curves are 0.735 Å and 0.790 Å corresponding to R1 values of 2.33 Å and 1.00 Å respectively and therefore, as the H-atom of HF approaches the midpoint of H_2, the minimum energy H_2 bond length decreases by only $\sim$ 0.06 Å for a corresponding change in R1 of 1.33 Å. Secondly, at the two different R1 geometries, both the corresponding $1\,^1A_1$ ground state H_2 potential curves are only very shallowly bound indicating that the total energy of the dimer is relatively unaffected by changes in the H_2 bond length for different R1 distances.

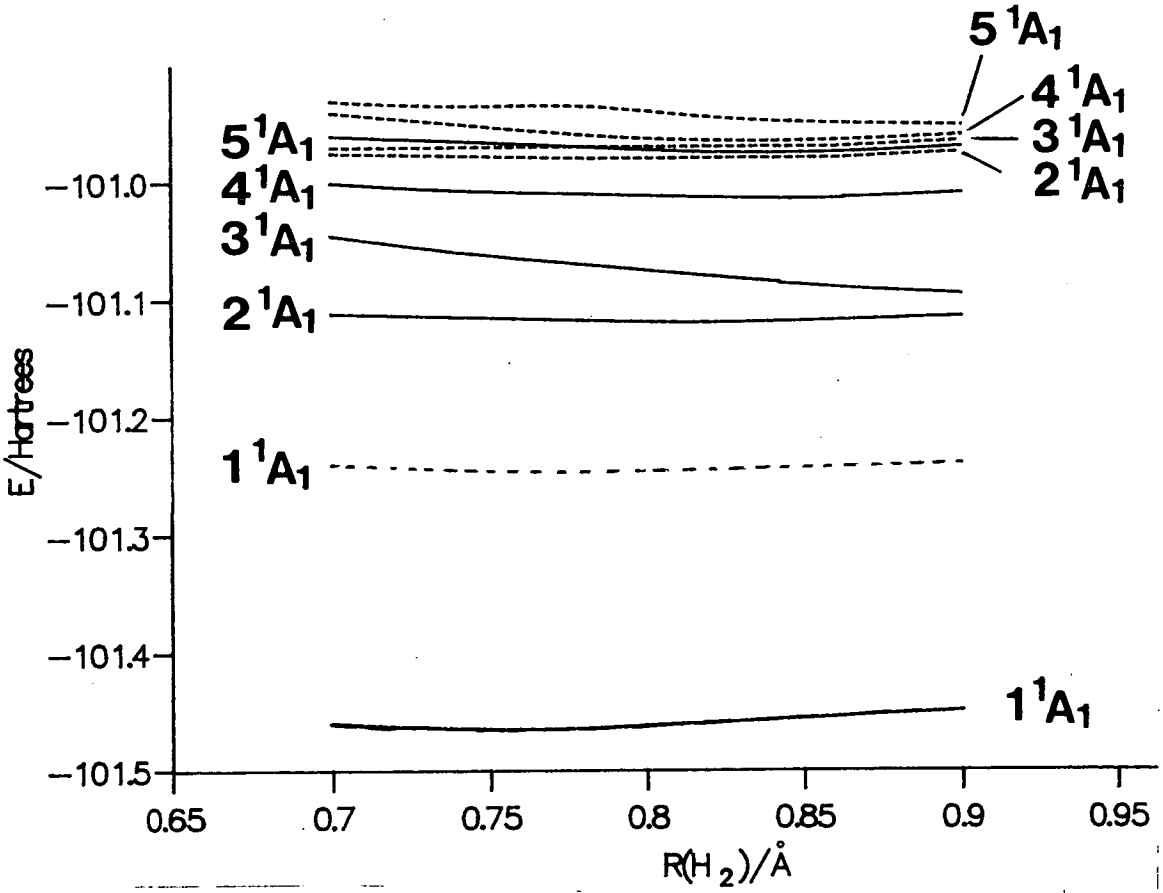

Figure 6.4. The $^1A_1$ state potential curves as a function of $R(H_2)$.

The calculated ω_e value of the H_2 stretching mode shown for the 1^1A_1 state (full curve) 4430.9 cm^{-1} where the HF and R1 coordinates are fixed at their equilibrium bond lengths of 0.94 Å and 2.33 Å respectively whilst the theoretical ω_e value of isolated H_2 determined by Bernholdt et al. [20] is 4376.3 cm^{-1} suggesting that, as with the HF stretching mode, ω_e of H_2 increases following complexation.

Concerted HF and H_2 Stretching

Figure 6.5 shows the potential energy curve generated as a function of the HF coordinate of the ground $1\,^1A_1$ state resulting from concerted HF and H_2 stretching. At a particular HF bond distance, GAMESS SCF geometry optimisation procedures [25] were performed on the H_2 coordinate and the resulting minimum energy H_2 bond length was used in the CI calculations. This procedure was repeated at several points along the HF coordinate.

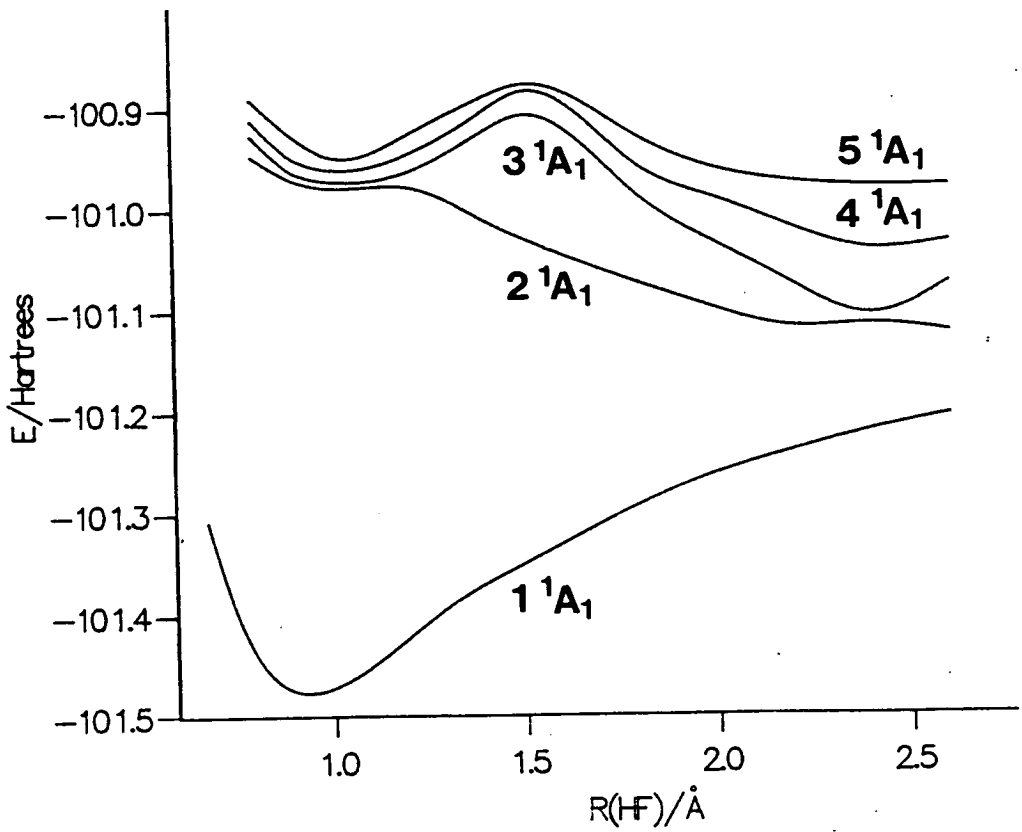

Figure 6.5. The $^1A_1$ state potential curves of H_2...HF generated by concerted HF and H_2 stretching.

The resulting potential curve behaves in a similar way to the one generated when the HF coordinate alone was varied, which comes as no surprise because the variation of the H_2 coordinate alone, had very little effect on $V(R)$ of the complex. Figure 6.6 shows the relationship between the SCF geometry optimised H_2 coordinate and the varying HF bond length. Between 1.4 Å $\geq$HF$\geq$ 0.7 Å, the optimised H_2 bond length increases slowly and beyond this region increases rapidly with increasing HF length. Along the whole of the potential curve, the main configuration in the final CI wavefunction is the SCF molecular orbital basis shown in table 6.2 and as the HF bond length increases away from the its equilibrium geometry, its bonding character becomes more σ-like, resulting in an increase in $V(R)$, an effect which is offset to a certain extent by formation of in-phase H_3^+.

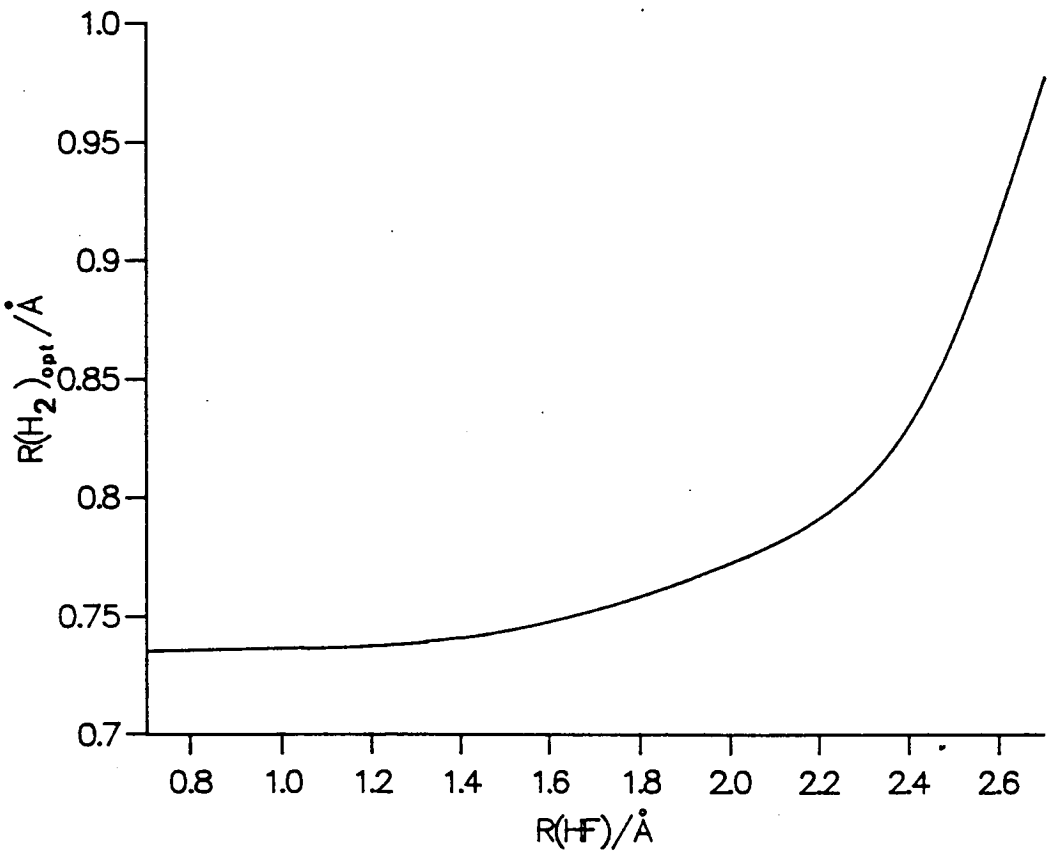

Figure 6.6. The relationship between R(HF) and $R(H_2)_{opt}$.

Concerted R1 and HF Stretching

Finally, we consider the potential energy curve generated as a function of the R1 coordinate where at each R1 distance the HF bond length is optimised at the SCF level and this value is used in the subsequent MRDCI calculation with the H_2 coordinate remaining fixed at 0.752 Å throughout.

Figure 6.7 shows the 1^1A_1 ground state potential curve as a function of the R1 coordinate for concerted R1 and HF stretching. As R1 decreases away from the the equilibrium geometry, the total energy of the complex increases slowly and beyond R1 ~1.10 Å a rapid rise in energy takes place, behaviour which is mirrored in figure 6.8 which shows how the the R1 and HF optimised bond lengths are related where for R1 values ≥1.00 Å, a rapid increase in the optimised HF distance takes place.

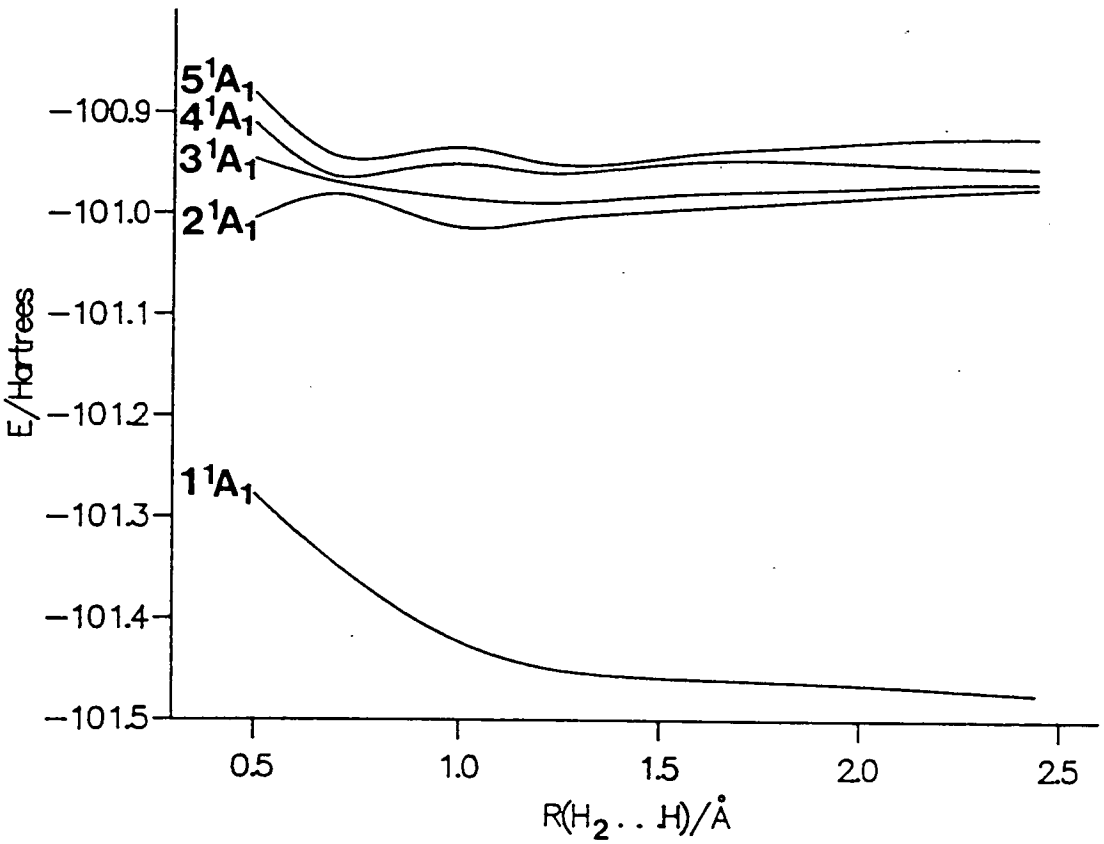

Figure 6.7. The $^1A_1$ state potential curves of H_2...HF generated by concerted (H_2...H) and HF stretching.

Analysis of how the character of the MOs transform along this potential curve provides an insight into why a rapid increase in $V(R)$ occurs at R1≥1.10 Å. Between 1.5 Å ≥R1≥ 0.9 Å as R1 decreases the HF character becomes increasingly antibonding and at the same time in-phase H_3^+ is formed, but beyond R1∼ 1.5 Å, H_3^+ becomes increasingly antibonding and the HF MOs become more σ-bonding.

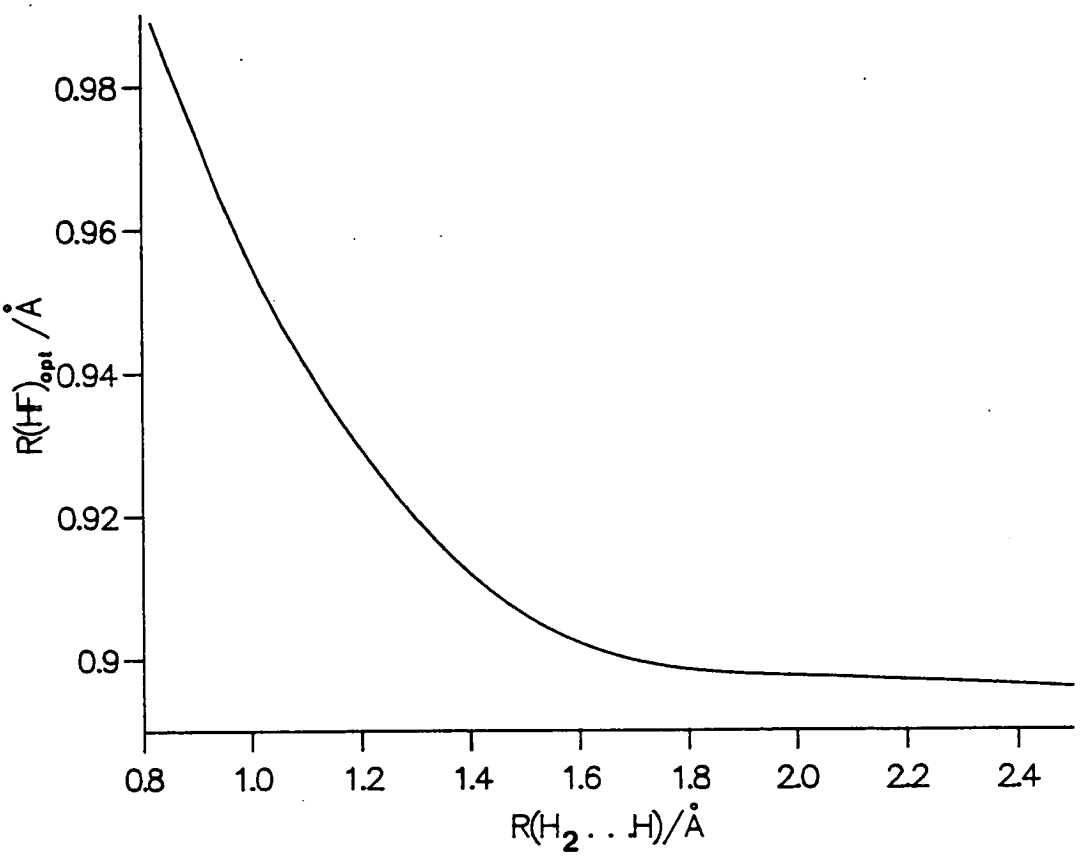

Figure 6.8. The relationship between $R(H_2...H)$ and $R(HF)_{opt}$.

6.5 Low Lying Rydberg States of H_2...HF

The electronic spectrum of the H_2...HF dimer will be dominated by transitions to Rydberg states and we have attempted to determine the behaviour of these states in the region above the global $^1A_1$ ground state minimum.

6.5.1 The $^1A_1$ Rydberg States

Variation of the HF Coordinate

The $^1A_1$ Rydberg states have electronic configurations arising from the promotion of a valence electron from a MO whose symmetry is the same as the destination Rydberg MO i.e $B_{1,2} \leftrightarrow B_{1,2}$ and $A_{1,2} \leftrightarrow A_{1,2}$ where the former transitions provide the lowest energy Rydberg states. The potential energy curves produced by varying only the HF bond length within the complex are shown in figure 6.2 whilst table 6.3 provides a summary of the bonding character of these states together with their vertical electronic energies, ΔE_v, calculated relative to the global $1\,^1A_1$ ground state minimum. From a comparison of our data with the $^1\Sigma$ Rydberg state energies of isolated HF, as calculated by Bettendorff et al. [27] shown in table 6.4, it is noticeable that without exception, all the $^1A_1$ ΔE_v values are lower in energy than the corresponding ones in isolated HF mainly as a result of CT and polarisation effects within the complex. The $2\,^1A_1$ state is formed by the one electron promotion $F(2p_y) \longrightarrow F(3p_y) + H_2(\sigma^*)$.

A good guide to the parentage of a particular Rydberg state can be found in the quantum defect, δ, calculated from a knowledge of the T_e values of the Rydberg state and the corresponding ionic core state as discussed previously in section 1.2.1 and 1.2.2.

H_2...HF State	ΔE_v (eV)	Bonding Character	R_e^{HF} (Å)
$1\,^1A_1$	-	ground state	0.91
$2\,^1A_1$	13.30	$F(2p_y)_v \rightarrow F(3p_y)_d + H_2(\sigma_u)_d$	1.02
$3\,^1A_1$	13.41	50% $F(2p_y)_v \rightarrow F(3p_y)_d + H_2(\sigma_u)_d$ 50% $F(2p_x)_v \rightarrow F(3p_x)_d$	1.01
$4\,^1A_1$	14.14	$H_2(\sigma_g)_v \rightarrow (H_3)_d + HF(\sigma^*)_d$	0.895
$5\,^1A_1$	14.60	$F(2p_y)_v \rightarrow F(3p_y)_{v/d} + H_2(\sigma_u)_{v/d}$	1.00

Table 6.3. Summary of the pertinent energies of the $^1A_1$ states of H_2...HF above the global minimum.

HF State	ΔE_v (eV)	Bonding Character	R_e^{HF} (Å)
$2\,^1\Sigma^+$	13.40	$2p_\pi \rightarrow 3p_\pi$	2.15
$3\,^1\Sigma^+$	14.46	$2p_\pi \rightarrow 3p_\pi$	1.10
$4\,^1\Sigma^+$	14.87	$\sigma \rightarrow \sigma^*$	1.02

Table 6.4. Vertical excitation energies and bonding characteristics of the low lying excited states in isolated HF from ref. [27] where R_{HF}=0.87 Å.

The calculated δ values of the $2\,^1A_1$ and $3\,^1A_1$ states are 0.63 and 0.57 corresponding to the $F(3p_y)$ and $F(3p_x)$ Rydberg orbitals respectively and are almost unchanged on complexation compared to those obtained in free HF ($\delta \approx 0.55$), although they are slightly non-degenerate probably as a result of the $F(2p_y)$ Rydberg orbital being considerably polarised by the $H_2(\sigma_u)$ anti-bonding orbital. The $4\,^1A_1$ state (E_v=14.14 eV) is predominantly charge-transfer in character due to the promotion $H_2(\sigma^*) \longrightarrow HF(\sigma^*)$.

Variation of the H_2 Coordinate

The four $^1A_1$ excited state potential energy curves resulting from a variation in the

H_2 coordinate only are shown in figure 6.4 at the two different regions of the potential energy surface discussed previously for the ground $1\,^1A_1$ state. All the excited state potentials associated with a fixed R1 bond length of 2.33 Å show little change in $V(R)$ as the H_2 coordinate alone is varied where only the ground and the $4\,^1A_1$ excited state seem significantly bound. At a compressed R1 bond length of 1.00 Å the behaviour of the excited states are similar to those at R1=2.33 Å with the exception of the $3\,^1A_1$ state which becomes steeply repulsive as the H_2 coordinate increases. The electronic character of this state is $HF(\sigma)_v \rightarrow H_2(\sigma_g)_d + HF(\sigma^*)_d$ where $(H_3)_d$ exhibits antibonding character. Hence, as the H_2 bond length increases there is a reduction in the overlap of the anti-bonding orbitals in $H_3(\sigma^*)$.

Concerted HF and H_2 Stretching

Figure 6.5 shows how the $^1A_1$ excited state potential energy curves behave as the HF and H_2 bond lengths are varied in a concerted manner as described previously for the $1\,^1A_1$ ground state. In general, the $3\,^1A_1$, $4\,^1A_1$ and $5\,^1A_1$ states all display similar behaviour over the potential surface. All are relatively deeply bound directly above the $1\,^1A_1$ ground state minimum and as the HF and H_2 coordinates expand the curves rise in energy and reach a saddlepoint at HF=1.50 Å and H_2=0.74 Å before falling sharply towards shallow minima centred at HF=2.40 Å and H_2=0.82 Å.

In contrast, the $2\,^1A_1$ state is quite shallowly bound in the region above the $1\,^1A_1$ minimum and as the HF and H_2 bond lengths increase this state traverses a small barrier in the potential surface (height of the barrier is $\sim$0.35 eV) and then falls sharply in energy towards a shallow minimum at HF=2.25 Å and H_2=0.80 Å before experiencing a strong avoided crossing with the $3\,^1A_1$ curve. Table 6.5 summarises the geometries and corresponding electronic configurations of the various minima in the region where 2.54 Å >HF>2.2 Å.

H_2...HF State	Bonding Character	Geometry at minima (Å)
$2\,^1A_1$	$HF(\sigma)_v \rightarrow HF(\sigma^*)_{v/d}+H_2(\sigma)_{v/d}$ and $H_3(\sigma^*)$	R1=1.00,HF=2.24,H_2=0.795
$3\,^1A_1$	50% as above + 50% $F(2p_y)\rightarrow H_2(\sigma^*)_{v/d}$	R1=0.84,HF=2.4,H_2=0.736
$4\,^1A_1$	as for $2\,^1A_1$	R1=0.81,HF=2.43,H_2=0.736
$5\,^1A_1$	$F(2p_x)_v \rightarrow F(3p_x)_{v/d}$	R1=0.74,HF=2.5,H_2=0.737

Table 6.5. The geometries and bonding characteristics for the $^1A_1$ excited state minima between 2.54 Å >HF>2.2 Å.

Concerted R1 and HF stretching

The first four $^1A_1$ potential energy curves generated as a function of the R1 and HF coordinates in a similar manner to the $1\,^1A_1$ state discussed previously, (with H_2 fixed at 0.725 Å) are shown in figure 6.7. Table 6.6 summarises their bonding characteristics in the region where R1 ≈1.0 Å.

H_2...HF State	Bonding Character	Geometry at minima (Å)
$1\,^1A_1$	Ground State	-
$2\,^1A_1$	$F(2p_y)\rightarrow F(3p_y)_d+H_2(\sigma^*)_d$	R1=1.036,HF=0.948
$3\,^1A_1$	$F(2p_x)\rightarrow F(3p_x)_d$	R1=1.236,HF=0.880
$4\,^1A_1$	$HF(\sigma)_v \rightarrow HF(\sigma^*)_d+H_2(\sigma)_d$	R1=1.236,HF=0.918
	+ $F(2p_x)\rightarrow F(3p_x)_d$	R1=0.736,HF=1.048
$5\,^1A_1$	$F(2p_y)\rightarrow F(3p_y)_d+H_2(\sigma^*)_d$	R1=1.236,HF=0.918
	+ $HF(\sigma)_v \rightarrow HF(\sigma^*)_d+H_2(\sigma)_d$	R1=0.736,HF=1.048

Table 6.6. The equilibrium geometries and bonding characteristics for the $^1A_1$ excited state minima at R1 ~1.0 Å.

6.5.2 The $^1B_1$ and $^1B_2$ Rydberg States

The B_1 and B_2 Rydberg states have electronic configurations which arise from the excitation of an F($2p_x$) (out of plane) and F($2p_y$) (in plane) valence electron respectively, to a Rydberg MO with A_1 symmetry. The potential curves generated by varying the HF and H_2 bond lengths in a concerted manner as described in the previous section are shown in figures 6.9 and 6.10 for the $^1B_1$ and $^1B_2$ states respectively.

Unlike in isolated HF where the Π_x and Π_y states are degenerate, the prescence of H_2 lifts the degeneracy of the corresponding B_1 and B_2 states within the complex. Directly above the $1\,^1A_1$ ground state minimum, the difference in energy between the $1\,^1B_1$ and $1\,^1B_2$ states is only 0.034 eV, where the former state has the lower energy. Table 6.7 shows the bonding characteristics and ΔE_v values of the $^1B_2$ states obtained in our calculations together with their geometries at their respective minima.

H_2...HF State	ΔE_v (eV)	Bonding Character	Geometry at the minima (Å)
$1\,^1B_2$	10.80	F($2p_y$)$_v$ $\rightarrow$HF(σ^*)$_v$+H_2(σ)$_v$	repulsive
$2\,^1B_2$	13.27	F($2p_y$)$_v$ $\rightarrow$HF(σ^*)$_d$+H_2(σ)$_d$ and H_3(σ^*)	R1=2.14,HF=1.095 H_2=0.736
$3\,^1B_2$	13.76	as for $2\,^1B_2$	R1=2.25,HF=0.985 H_2=0.736
$4\,^1B_2$	14.55	as for $2\,^1B_2$	R1=2.24,HF=1.000 H_2=0.739
$5\,^1B_2$	14.91	F($2p_y$)$_v$ $\rightarrow$HF(σ^*)$_v$+H_2(σ)$_{v/d}$ and H_3(σ^*)	R1=2.16,HF=1.075 H_2=0.739

Table 6.7. Bonding characteristics and vertical excitation energies of the $^1B_2$ Rydberg states.

HF State	ΔE_v (eV)	Bonding Character	R_{HF} at minima (Å)
$2\,^1\Pi_{val}$	10.42	F(2pπ)→ σ^*	repulsive
$3\,^1\Pi_{Ryd}$	13.07	F(2pπ)→3s	1.02
$4\,^1\Pi_{Ryd}$	13.94	F(2pπ)→3pσ	1.02
$5\,^1\Pi_{Ryd}$	14.41	F(2pπ)→3dσ	1.01

Table 6.8. Vertical excitation energies and bonding characteristics above R_e=0.87 Å for the Π-states of isolated HF [27].

The corresponding $^1\Pi$ states of isolated HF obtained from the theoretical calculations of Bettendorf et al. [27] are given for comparison and shown in table 6.8. In contrast to the ground $1\,^1B_1$ and $1\,^1B_2$ states shown in figures 6.9 and 6.10 respectively, all the excited Rydberg states are significantly bound. The $1\,^1B_2$ potential curves generated with a fixed and variable H_2 coordinate are almost identical in nature suggesting that the repulsive nature of this state is dependent on the HF stretching mode alone. The electronic configurations of the repulsive $1\,^1B_1$ and $1\,^1B_2$ states correspond to an electron being removed from the F($2p_x$) and F($2p_y$) orbitals respectively, into a valence HF(σ^*) MO. Therefore as the HF coordinate is stretched, the overlap between the antibonding orbitals on HF decreases resulting in a lowering of $V(R)$, which is very similar in nature to that of the repulsive $^1\Pi_{val}$ state in isolated HF. The $2\,^1B_2$ (E_v=13.27 eV), $3\,^1B_2$ (E_v=13.76 eV) and $4\,^1B_2$ (E_v=14.55 eV) states all result from the excitation, F($2p_y$)⟶F(3s)+F($3p_z$)+HF(σ^*). There is thus no state with the characteristic quantum defect of the atomic 3s orbital (E_v expected at ≈11 eV). The situation is further complicated by the fact that σ⟶σ^* excitation in H_2 (which occurs at ≈13 eV in the isolated molecule) also gives rise to a state of $^1B_2$ symmetry and this configuration is an important component of these same three states.

The potential energy curves of the $^2B_1$ and $^2B_2$ ground state cations are also shown in figures 6.9 and 6.10 and they represent the limit of the $^1B_1$ and $^1B_2$ Rydberg series respectively. At the equilibrium geometry of the ground $1\,^1A_1$

state, the difference in energy between the $^2B_1$ and $^2B_2$ ground state cations is only 3.05×10^{-4} eV which is far smaller than our level of accuracy, where only $\geq$0.5 eV is significant. The very small $^2B_1/^2B_2$ splitting in H_2...HF^+ arises because the unpaired electron is located on the F atom which is remote from the H_2 molecule, and it is the latter which is responsible for lowering the $C_{\infty v}$ symmetry. Presumably, had the geometry H_2...F^+H been examined, a much larger $^2B_1/^2B_2$ splitting would have been found. None of these states have bonding character associated with the F(3s) orbital which would be expected to be at $E_v\approx11$ eV.

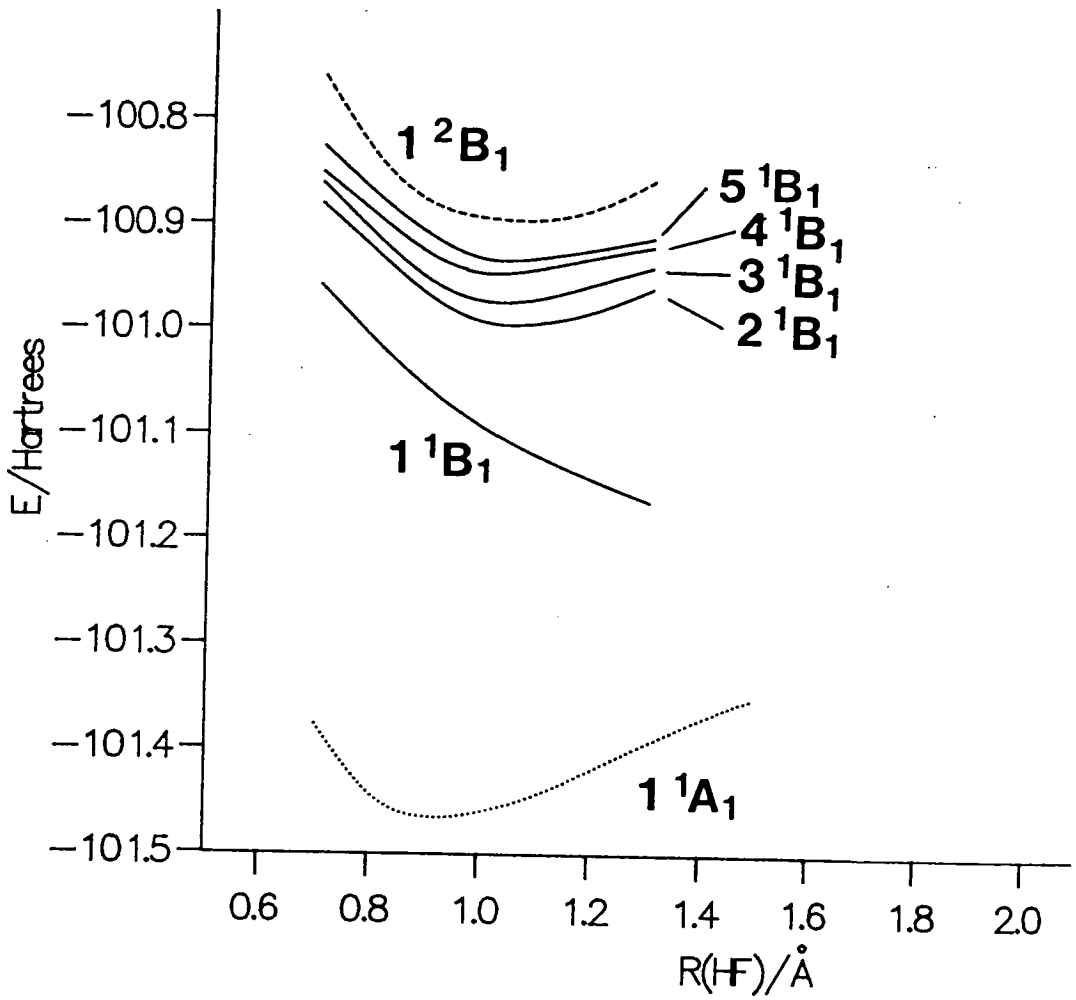

Figure 6.9. The $^1B_1$ Rydberg state potential curves of H_2...HF generated by concerted HF and H_2 stretching.

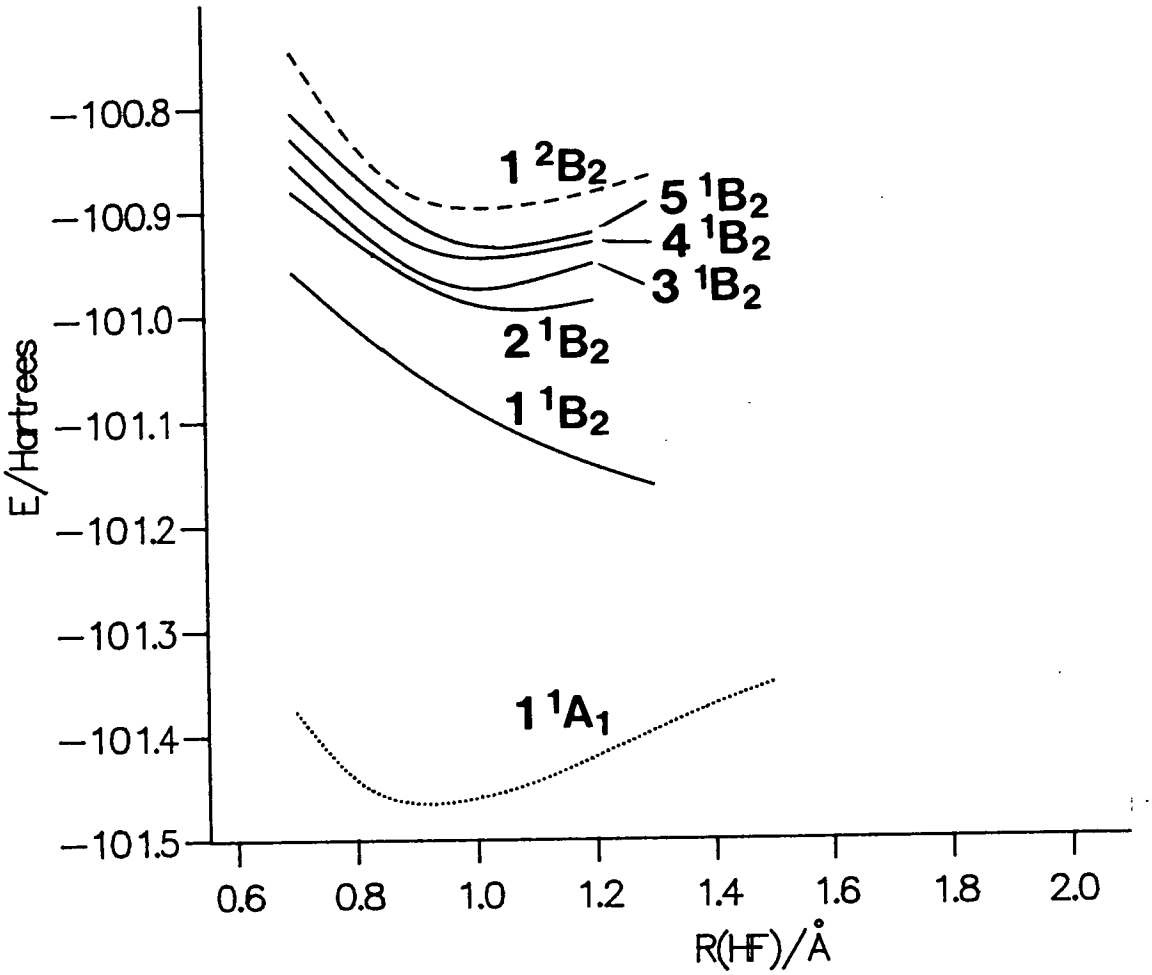

Figure 6.10. The $^1B_2$ Rydberg state potential curves of H_2...HF generated by concerted HF and H_2 stretching.

6.5.3 The $^1A_1$ Ground and Excited States of $H_3^+F^-$

One of the principal objectives in our studies was to determine which state(s) of the H_2...HF dimer in the T-shaped geometry of C_{2v} symmetry correlates with the $^1A_1$ $H_3^+F^-$ state. In particular, a knowledge of the lowest energy pathway on the potential energy surface from which the minimum of this ion-pair energy state may be reached is desirable.

There now follows a brief discussion on the energetics of $H_3^+F^-$ formation bearing in mind that the experimental question is whether this state can be accessed

from the neutral $[H_2...HF]_{eqm}$ geometry by a vertical transition to the H^+F^- ion-pair state ($\sigma \longrightarrow \sigma^*$ transition). From figure 6.11, it is clear that the H_3^++F^- surface is higher in energy than the H_2...H...F one as $R \rightarrow \infty$, but as the H atom approaches the H_2 molecule the ground state surface rises steeply (H_3· is unstable since the extra electron is in an anti-bonding orbital), whereas the $H_2...H^+...F^-$ surface is falling rapidly (if F^- is brought in concertedly). A crossing of these two surfaces would therefore be expected to occur somewhere.

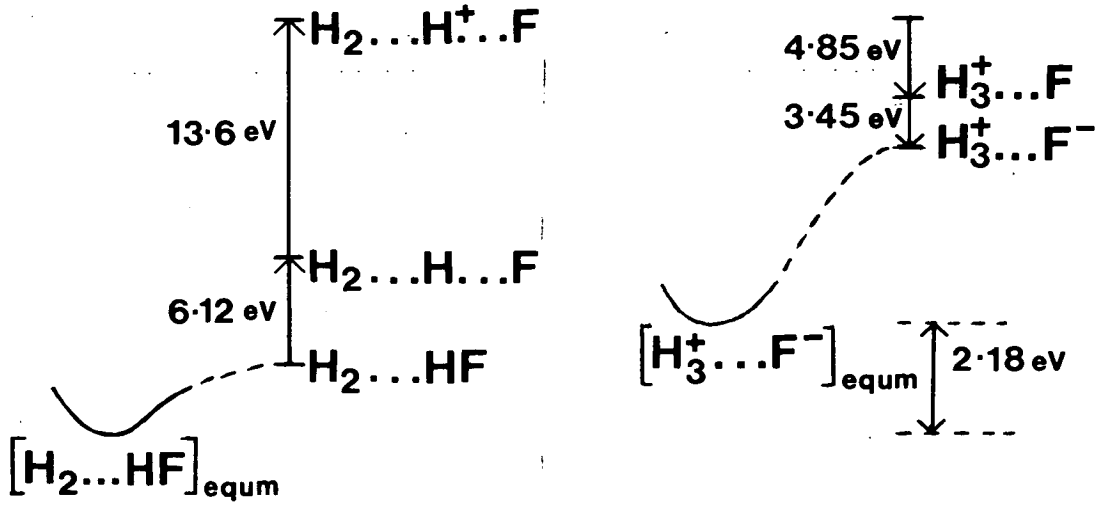

Figure 6.11. The energetics of $H_3^+...F^-$ formation.

Figure 6.12 shows the potential energy curves of the lowest five $^1A_1$ states of $H_3^+F^-$ generated by fixing the three H-atoms in the equilibrium geometry of H_3^+ (R_{H-H}=0.879) [28,29] and the F atom moved. The 1^1A_1 $H_3^+F^-$ ground state has a strongly bound potential minimum at R_{HF}=1.075 Å with a well depth of 9.28 eV measured relative to the H_3^++F^- dissociation limit calculated using experimental values for the proton affinity of H_2 [30,31] and the electron affinity of F [32]. A

simple Coulombic interaction model (which does not take into account any polarisation/CT effects) between a point charge $-e$ centred on the F atom and charges of $+\frac{1}{3}e$ on each of the three H-atoms predicts a well depth of ~9.55 eV at a HF bond length of 1.075 Å and confirms the proton-transfer nature of the state. The H_3^++F^- minimum is found to be only 2.23 eV above the global minimum of the lower $^1A_1$ surface which is remarkably close when compared with the T_e value of the lowest ion-pair state of HF($B^1\Sigma^+$) which is ~11 eV above the minimum of HF($X^1\Sigma^+$).

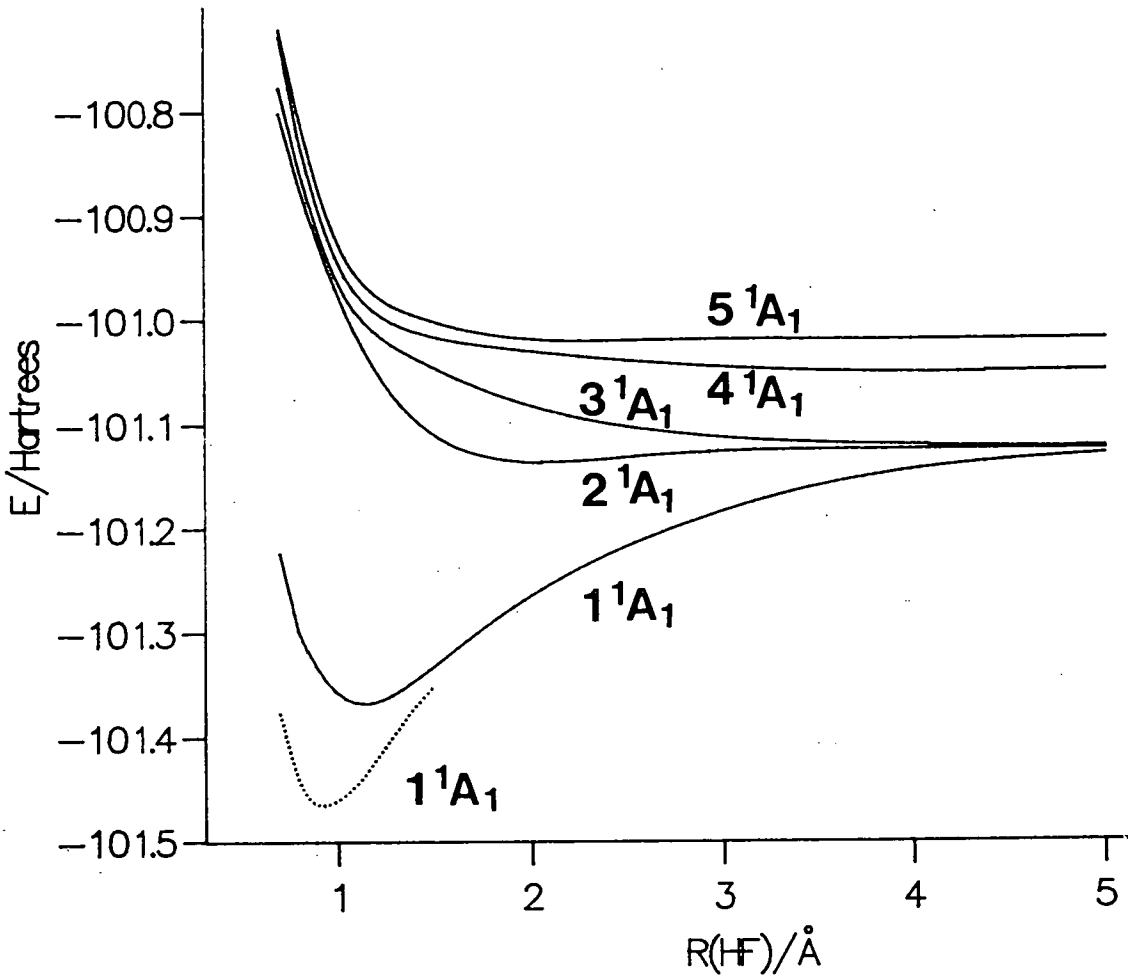

Figure 6.12. The $^1A_1$ state potential curves of H_3^+...F^- as a function of R(HF). The $R(H_2)$ and $R(H_2...H)$ geometries being fixed at $(H_3^+)_{eqm}$.

At the $H_3^+F^-$ minimum, about 95% of the final wavefunction of the $1\,^1A_1$ state is composed of the SCF MO basis shown in table 6.9 and as the F atom moves away from H_3^+, these MOs transform into ones with purely ionic character resulting in the attractive part of the potential being mainly Coulombic in nature. In reality, the $^1A_1$ ground state correlates adiabatically with the neutral H_3 + F dissociation products because an avoided crossing takes place with the $2\,^1A_1$ state between 4.9 Å $\geq R_{HF} \geq$4.7 Å. The dissociation products associated with the ground and excited states of $^1A_1$ $H_3^+F^-$ are shown in table 6.10.

R_{HF}=2.0 Å		R_{HF}=5.0 Å	
MO	Bonding Character	MO	Bonding Character
$1\,A_1$	F(1s)	$1\,A_1$	F(1s)
$2\,A_1$	F(2s)	$2\,A_1$	F(2s)
$3\,A_1$	$H_3^+(\sigma)$+F^- with HF(σ^*)	$3\,A_1$	H_3^+
$1\,B_1$	F($2p_x$)	$1\,B_1$	F($2p_x$)
$1\,B_2$	F($2p_y$)	$1\,B_2$	F($2p_y$)
$4\,A_1$	$H_3^+(\sigma^*$+F^- with HF(σ^*)	$4\,A_1$	F($2p_z$)

Table 6.9. SCF MOs for H_3^++F^- for a fixed H_3^+ geometry at two HF distances.

$H_3^+F^-$ State	ΔE_v (eV)	Bonding Character	ΔE_v (eV)	Bonding Character for Diss. Products
$1\,^1A_1$	-	$H_3^+F^-$	-	$F(2p_y) \rightarrow H_2(\sigma^*)_v + (H_3^+)\sigma_d^*$
$2\,^1A_1$	10.25	$F(2p_y) \rightarrow H_2(\sigma^*)_{v/d}$+HF($\pi_y^*$) $(H_3^+)\sigma_{v/d}^*$	0.35	$H_3^+F^-$
$3\,^1A_1$	10.58	as above	0.68	$F(2p_z) \rightarrow (H_3^+)\sigma_{v/d}^*$
$4\,^1A_1$	11.18	$F(2p_x) \rightarrow (H_3^+)\sigma_{p_x}^*$+HF($\pi_x^*$)	2.23	as above
$5\,^1A_1$	11.56	$(H_3^+)_v \rightarrow H_3^+\sigma_{v/d}^*$+ HF($\sigma$)$_d$	3.02	$F(2p_x) \rightarrow (H_3^+)_d^*(p_x)$

Table 6.10. Pertinent energies and the bonding characteristics of the $^1A_1$ $H_3^+F^-$ states for H_3^+ fixed at the isolated equilibrium geometry where the HF coordinate only was varied.

The first four excited states of $^1A_1$ H_3^++F^- are all strongly repulsive and their vertical excitation energies, ΔE_v, relative to the $1\,^1A_1$ $H_3^+F^-$ minimum are shown in table 6.10, together with a summary of their electronic configurations.

Having located H_3^+...F^- in C_{2v} geometry, there is probably a steep downhill path to the global minimum on the 1^1A_1 surface for the proton transfer state in C_{3v}. In this geometry the H_3^+...F^- structure would be the probable minimum energy one simply because only dissociation to H_3+F rather than H_2 + HF can occur, though there are conical intersections. The pathway between C_{2v} and C_{3v} symmetries would correspond to out-of-plane bending of HF so that F^- can move onto the three-fold axis above the H_3 plane.

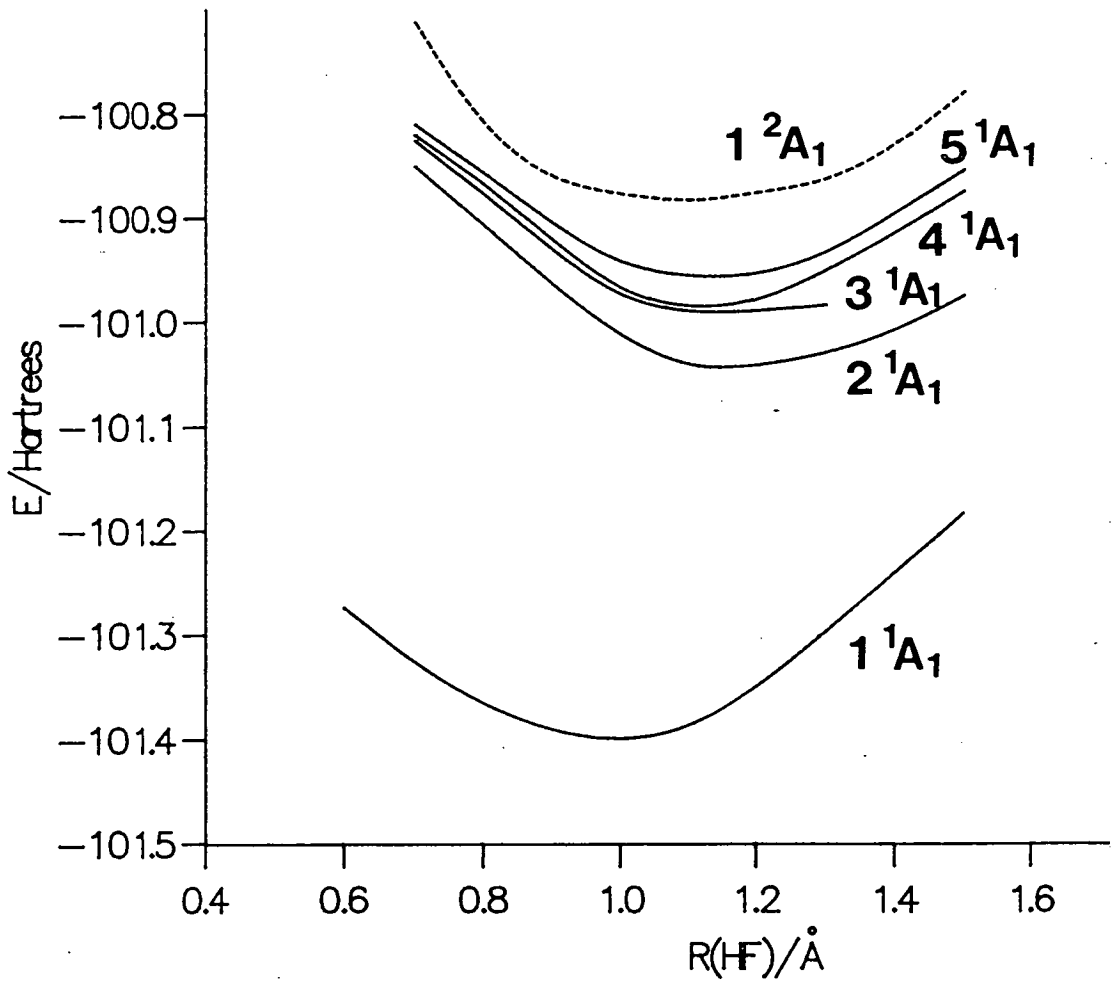

Figure 6.13. The $^1A_1$ state potential curves of H_3^+...F^- as a function of R(HF) with the F atom being fixed at 1.86 Å from H_2.

So far we have explored the behaviour of the first five states of $^1A_1$ symmetry for a fixed H_3^+ equilibrium geometry where only the F-atom was moved. We now consider the potential energy curves generated as the $R(H_2...H)$ coordinate was compressed from 3.17 Å to 1.54 Å with the F atom and H_2 being fixed throughout. The resulting potential curves for the ground and excited states of $^1A_1$ $H_3^+F^-$ are shown in figure 6.13. The ground state minimum at HF=1.00 Å and R1=0.86 Å is ~0.46 *eV* lower in energy than the minimum obtained using the fixed H_3^+ geometry described previously. Only a limited search in the H...H coordinate was carried out at each step. Table 6.11 summarises the pertinent energies and bonding characteristics of the Rydberg states relative to the $^1A_1$ $H_3^+F^-$ ground state minimum.

$H_3^+F^-$ State	ΔE_v (*eV*)	Bonding Character
$1\,^1A_1$	-	$H_3^+F^-$
$2\,^1A_1$	10.61	$F(2p_y) \rightarrow H_2(\sigma^*)_v + H_3^+(\sigma_d^*) + HF(\pi_y^*)$
$3\,^1A_1$	11.51	$H_2(\sigma^*)_v + HF(\sigma^*)_v \rightarrow H_3^+(\sigma_{v/d}^*)$
$4\,^1A_1$	11.75	$F(2p_x) \rightarrow H_3^+(\sigma_d^*)(p_x)$
$5\,^1A_1$	12.51	$H_2(\sigma^*)_v + HF(\sigma^*)_v \rightarrow H_3^+(\sigma_{v/d}^*) + HF(\sigma)_{v/d}$

Table 6.11. The vertical excitation energies relative to the $1\,^1A_1$ $H_3^+F^-$ minimum for the Rydberg states of $H_3^+F^-$.

The calculated ω_e for the HF stretching mode of the 1^1A_1 $H_3^+F^-$ state is 5238.5 cm^{-1} compared with 4344 cm^{-1} in the ground $1\,^1A_1$ state of H_2...HF which is very unexpected because ion-pair states are generally characterised by relatively small ω_e values compared with the global ground state. However, as the HF coordinate stretches, a node develops in the wavefunction between the the H-atom of HF and H_2 and as a result they are increasingly repelled by each other causing the steeper than expected repulsive limb in the $1\,^1A_1$ $H_3^+F^-$ state to produce the larger than expected ω_e value.

All the higher states show evidence of a strongly avoided crossing with a state that has a minimum at $R(H_2...H)$ ~0.8 Å. For the 2^1A_1 state, there is a small barrier of less than 0.1 eV before the potential falls steeply to a minimum at 9.52 eV. The 2^1A_1 state vertically above the ground state is essentially $2p_y \rightarrow 3p_y$ excitation, but this soon becomes mixed with the HF($\sigma \longrightarrow \sigma^*$) excitation as $R(H_2...H)$ decreases.

In this region of the potential energy surface none of the states correlate with $H_3^+F^-$ because there is no doubly occupied MO composed of three H(1s) orbitals combined in phase.

6.5.4 The $[H_2...HF]^+$ Cations

An understanding of the behaviour of the $[H_2...HF]^+$ cationic potential energy curves is important for two main reasons. Firstly, it provides an insight into the photoelectron dynamics of weakly bound WDV complexes and secondly, the behaviour of the Rydberg states potential curves discussed in the previous sections are largely dependent on the electronic character of the ion-core as opposed to the diffuse nature of the Rydberg electron.

All the potential curves are generated by varying the HF and H_2 coordinates in a concerted manner as described previously and it is worth noting that no diffuse p-orbitals are employed on any of the three H-atoms.

The $^2B_1$ and $^2B_2$ Cations

From a knowledge of isolated HF where the lowest energy ground state cation is the $^2\Pi$ state arising from the removal of a degenerate, non-bonding F(p_y) or F(p_x) electron, the analogous non-degenerate ^2B states are found to be those with lowest energy in $[H_2...HF]^+$.

SCF geometry optimisation calculations [25] were performed on both the $^2B_1$ and $^2B_2$ cations where the HF, H_2 and R1 bond lengths were allowed to relax towards a global energy minimum such that dE/dR_{H_2}=0, dE/dR_{R1}=0 and dE/dR_{HF}=0 simultaneously. For the $^2B_1$ state however, after a large number of program cycles the energy remained unconverged with $R(H_2)$=0.7622 Å, $R(H_2...H)$=0.1355 Å and R(HF)=1.24134 Å. A similar procedure was carried out for the $^2B_2$ and again the calculation remained unconverged with $R(H_2)$=1.1 Å, $R(H_2...H)$=4.666 Å and R(HF)=0.895 Å. When the R1 coordinate was fixed at 2.33 Å the T1 and HF minima for the energy gradients of these two coordinates were found to be $R(H_2)$=0.87 Å and R(HF)=0.92 Å at the SCF level.

The ground state potential curves of the $^2B_1$ and $^2B_2$ cations corresponding to removal of an F(p_x) (out of-plane) and F(p_y) (in-plane) electron respectively are shown in figure 6.14 together with the first four excited states. The $^2B_1$ and $^2B_2$ curves are indistinguishable with the energy scale used. Their bonding characteristics and ΔE_v energies relative to the 1^1A_1 global minimum are summarised in table 6.12 for the $^2B_2$ state.

The minimum of the ground $1\,^2B_2$ potential curve shown in figure 6.13 corresponds to a geometry with HF=1.06 (0.91) Å, R1=2.18 (2.33) Å and H_2=0.736 (0.735) Å where the values in brackets are those of the neutral complex. The removal of a non-bonding F($2p_y$) electron results in a 0.15 Å increase in the HF bond length. This behaviour is mirrored in isolated HF where removal of an effectively non-bonding F($p\pi$) electron results in an increase in the bond length of 0.109 Å [27].

$[H_2...HF]^+$ State	ΔE_v (eV)	Bonding Character	Geometry of minima (Å)
$1\,^2B_2$	15.72	$F(2p_y)^{-1}$	HF=1.06, H_2=0.736
$2\,^2B_2$	26.19	$F(2p_y)^{-1} \rightarrow HF(\sigma^*)_d + (H_3^+)_v$	-
$3\,^2B_2$	26.87	as above	-
$4\,^2B_2$	30.30	$F(2p_y)^{-1} \rightarrow HF(\sigma^*)_d + H_3^+(\sigma_d^*)$	-
$5\,^2B_2$	30.95	as above	HF=0.99, H_2=0.736

Table 6.12. The bonding characteristics and pertinent energies of the $^2B_2$ $[H_2...HF]^+$ cation.

Directly above the ground $^1A_1$ global minimum the difference in energy between the $1\,^2B_1$ and $1\,^2B_2$ states is only 3.05×10^{-4} eV where the latter is the lower in energy (which is the reverse trend from that expected for the more unfavourable $\theta_{yy}(H_2)/\theta_{yy}(F2p)$ interaction in the $^2B_2$ state). The vertical ionisation energy of the ^2B cation is 15.72 eV as compared to 15.91 eV [27] for isolated HF^+ ($^2\Pi$) corresponding to a lowering in the vertical IP of the cluster due mainly to the polarisation of H_2 by the newly formed HF^+. The adiabatic IPs of $[H_2...HF]^+$ (^2B) and isolated HF ($^2\Pi$) are summarised in table 6.13.

Species	Adiabatic IP (eV)	reference
$[H_2...HF]^+$ (^2B)	15.50	this work
ab initio HF^+ ($^2\Pi$)	15.66	[27]
expt HF^+ ($^2\Pi$)	16.03	[32]

Table 6.13. Summary of adiabatic IPs.

In reality, the effective charge does not reside exclusively on the F atom from which the electron was removed. At $R(H_2...F)$=3.24 Å corresponding to vertical ionisation from the global 1^1A_1 ground state minimum, a simple charge-polarisation interaction given by, $V(R) = -\frac{1}{2}\alpha_\perp e^2/4\pi\varepsilon_0 R^4$, which predicts a Δ(IP) of 0.046 eV rather than the calculated 0.19 eV using $\alpha_\perp(H_2)$=0.705 Å [21]. This

suggests there is some charge migration within the $HF^+(\sigma)$ bond which in effect increases the dipole moment of HF.

The ^2B cation potential energy curves generated over the HF stretching region shown in figure 6.14 results in a corresponding change in the H_2 coordinate of only 0.01 Å and therefore the calculated ω_e value for the HF stretching mode is 3006.4 cm^{-1} which is almost unchanged from isolated HF^+ (3016 cm^{-1}). Table 6.14 summarises various pertinent ω_e values.

Species	ω_e(HF)/cm^{-1}	Reference
[H_2...HF] (1^1A_1)	4344.2	this work
ab initio HF ($X^1\Sigma$)	4136.0	[27]
[H_2...HF]$^+$ (^2B)	3006.4	this work
ab initio HF^+ ($^2\Pi$)	3050-3090	[27]
expt HF^+ ($^2\Pi$)	3016	[33]

Table 6.14. Some pertinent ω_e values for the HF stretching mode.

In isolated HF there is a 1086 cm^{-1} decrease in ω_e following ionisation suggesting that the F($2p\pi_{x,y}$) electron is not exclusively non-bonding. Similarly, in the complex, ionisation of the F($2p_{x,y}$) electron results in a decrease in ω_e of ~1338 cm^{-1}. The values in table 6.13 also show that a lowering in $\omega_e(HF^+\ ^2\Pi)$ takes place following complexation with H_2. In contrast, in the neutral complex there was a an increase in ω_e(HF) following complexation with H_2.

Finally, we briefly discuss how the steeply repulsive behaviour of the 2^2B and 3^2B states in figure 6.14 can be explained by considering how the MO eigenvectors transform as the HF coordinate is stretched. These two states have an electronic configuration resulting from the promotion of a valence $H_2(\sigma)$ electron into an unoccupied MO with a mixture of valence H_3^+ in-phase and diffuse $HF(\sigma^*)$ bonding character. Therefore, as the HF bond length increases, there is enhanced in-phase H_3^+ bonding and a reduction in antibonding $HF(\sigma)$ character resulting in a lowering in $V(R)$.

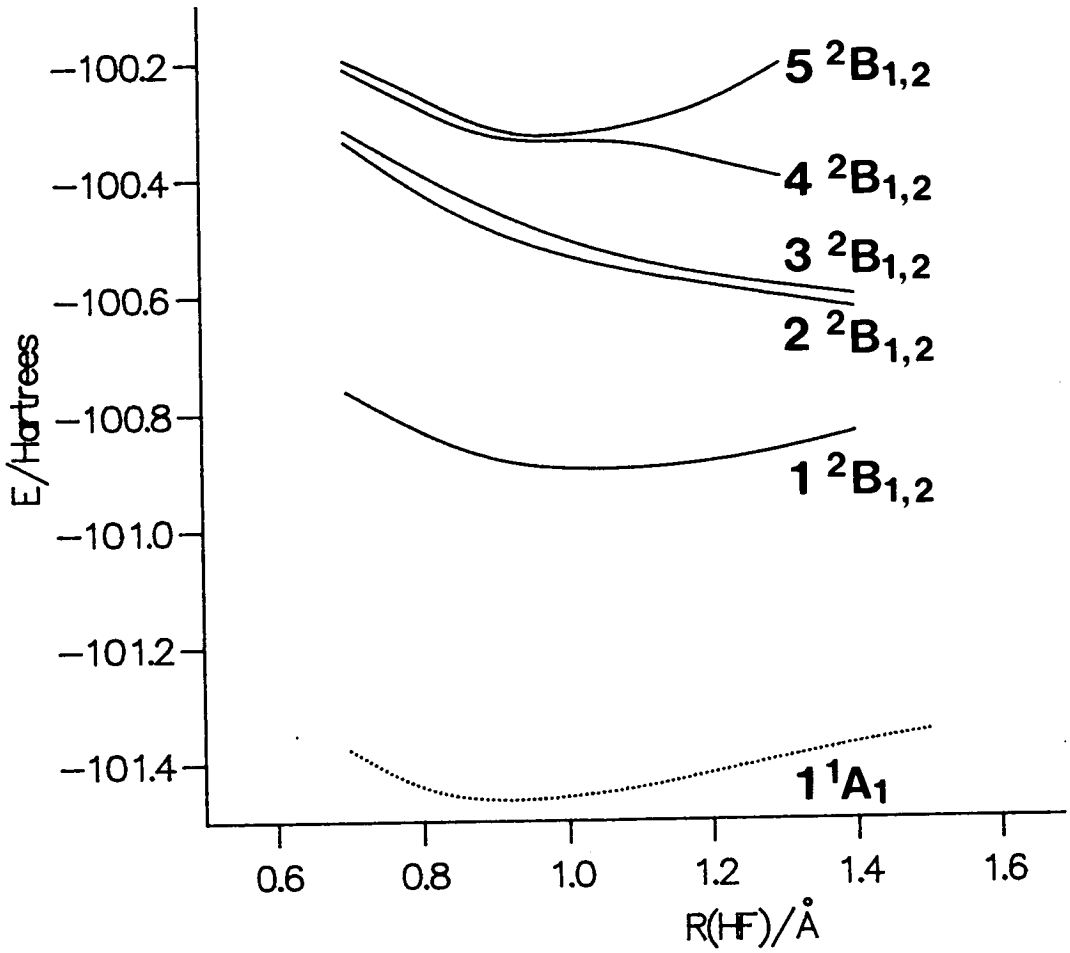

Figure 6.14. The $^2B_1$ and $^2B_2$ state potential curves of $[H_2...HF]^+$ as a function of R(HF). The $^2B_1$ and $^2B_2$ curves are indistinguishable in energy at this scale.

The $^2A_1$ Cations

The potential energy curves of the first five states with $^2A_1$ symmetry generated by concerted HF and H_2 stretching are shown in figure 6.15 and their bonding characteristics and ΔE_v values are summarised in table 6.15.

The $1\,^2A_1$ state of $[H_2...HF]^+$is essentially a single configuration resulting from the removal of a $H_2(\sigma_g)$ bonding electron. The calculated adiabatic IP is 17.53 compared with the experimental adiabatic IP of isolated H_2 of 15.42 eV and hence the prescence of HF increases the IP of H_2 within the complex by 2.11 eV due to the unfavourable orientation of the HF dipole with respect to the newly created positive charge on H_2. The resulting potential surface is presumably steeply repulsive in the R and θ coordinates and this ionisation channel should result in the rotation of the HF molecule into the more stable H_2^+...FH species.

The minimum of the 1^2A_1 potential curve corresponds to a geometry with HF=0.925 (0.91) Å, R1=2.311 (2.33) Å and H_2=0.736 (0.735) Å where the values in brackets represent the equilibrium geometry of the neutral H_2...HF $1\,^1A_1$ ground state. Because the electron has been removed from the $H_2(\sigma)$ MO the resulting change in the HF bond distance following ionisation is only 0.015 Å. Consider also that the equilibrium bond distance in isolated H_2^+ of 1.06 Å is 0.324 Å larger than the H_2 distance at our minimum in the $[H_2^+...HF]$ ($^2A_1$) complex where the H_2 coordinate has not been allowed to relax. SCF geometry optimisation of this coordinate, keeping R1 fixed at ~2.3 Å results in the H_2 coordinate increasing to 1.05 Å when dE/dR_{H_2} is a minimum. CI calculations were not carried out at this new geometry.

The calculated ω_e(HF) value of the 1^2A_1 state 7023.6 cm^{-1} which is significantly larger than the corresponding value obtained in neutral H_2^+...HF of 4344.2 cm^{-1}. A possible reason for this is as a result of the $H^{\delta+}$ atom on HF being repelled by the positive charge on H_2^+ as the HF bond stretches.

State	ΔE_v (eV)	Bonding Character	Geometry at minimum (Å)
$1\,^2A_1$	17.08	$H_2(\sigma)^{-1}$	HF=0.92, H_2=0.736
$2\,^2A_1$	19.94	$HF(\sigma)^{-1}$	HF=1.125, H_2=0.738
$3\,^2A_1$	26.94	$H_2(\sigma)^{-1}$+F($2p_y$)$\rightarrow H_2(\sigma^*)_{v/d}$	HF=1.00,H_2=0.736
$4\,^2A_1$	29.32	as above	HF=1.40, H_2=0.74
$5\,^2A_1$	29.87	as above	HF=1.00, H_2=0.736

Table 6.15. The bonding characteristics and vertical energies of the $^2A_1$ cationic states.

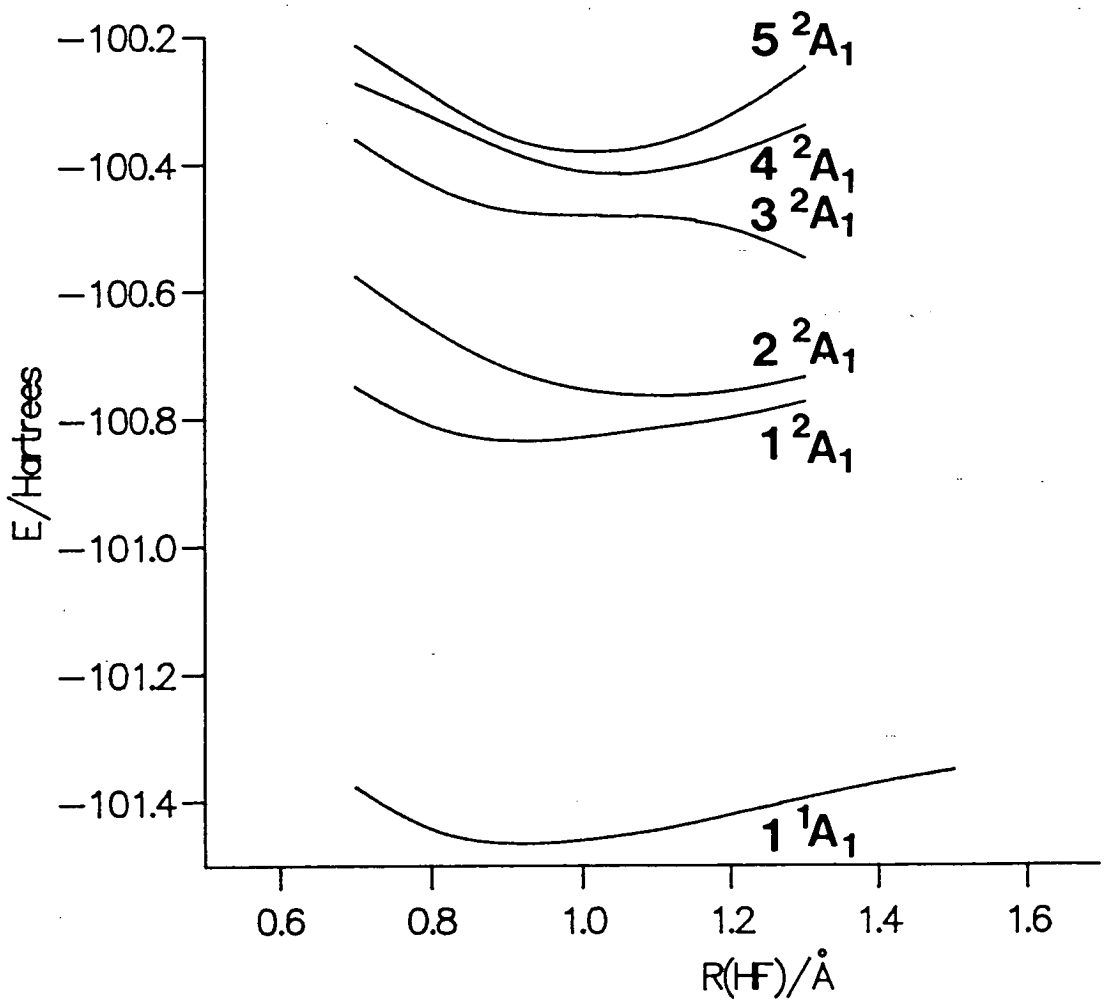

Figure 6.15. The $^2A_1$ state potential curves of $[H_2...HF]^+$ as a function of R(HF).

The $2\,^2A_1$ state shown in figure 6.15 is essentially a single configuration resulting from an electron being removed from an exclusively HF(σ) bonding orbital. The calculated adiabatic IP is 20.55 *eV* which compares with 19.118 *eV* [33] for isolated HF^+ ($^2\Sigma$) showing that there is an increase in the HF(σ)$^{-1}$ IP following complexation with H_2. The geometry at the minimum of the $2\,^2A_1$ state is HF=1.125 (0.91) Å, R1=2.111 (2.33) Å and H_2=0.738 (0.735) Å, where the values in brackets represent the equilibrium geometry of the neutral $1\,^1A_1$ ground state. As expected, following HF(σ)$^{-1}$ ionisation, the HF bond length within the complex has increased by 0.215 Å which compares with the corresponding change in bond length for isolated HF is 0.238 Å [33].

The $^2A_1$ Cations of $H_3^+F^-$

Assuming it is possible to reach the $H_3^+F^-$ ($^1A_1$) state from the $^1A_1$ ground state minimum of H_2...HF then we may anticipate that the lowest energy cations of the ion-pair state will be those of ^2B symmetry formed by the removal of a $2p_x$ or $2p_y$ electron on F^-. However, it is the higher energy $^2A_1$ states of $[H_3^+F^-]^+$ that we shall be concerned with.

The potential energy curves of the first four states with $^2A_1$ symmetry generated by varying the HF coordinate only (H_2 remains fixed at 0.879 Å throughout) are shown in figure 6.16. Their bonding characteristics and ΔE_v values calculated relative to the 1^2A_1 [$H_3^+F^-$] minimum are summarised in table 6.16.

The 1^2A_1 state arises from the removal of an electron from the MO shown in table 6.16 where the minimum of this potential state curve corresponds to a geometry with HF=1.15 Å and the HF bond length at the minimum of the 1^2A_1 $H_3^+F^-$ state is 1.00 Å. We would expect the removal of a partially antibonding HF electron to reduce the HF bond length in the cation but this effect is overidden by the reduced antibonding character in H_3^+ and therefore the HF bond actually increases. The vertical and adiabatic IPs are 14.55 (17.08) *eV* and 13.95 (17.53) *eV* respectively, relative to the $1\,^1A_1$ $H_3^+F^-$ state minimum. The values in brackets

refer to the IPs obtained for the $[H_2...HF]^+ \, 1\,^2A_1$ state relative to the $H_2...HF \, 1\,^2A_1$ global minimum. Although the difference in geometry between $H_2...HF$ and $H_3^+F^-$ species is significant, these results seem to indicate that ionisation of the latter is lower in energy by $\sim$2.53 eV relative to the former.

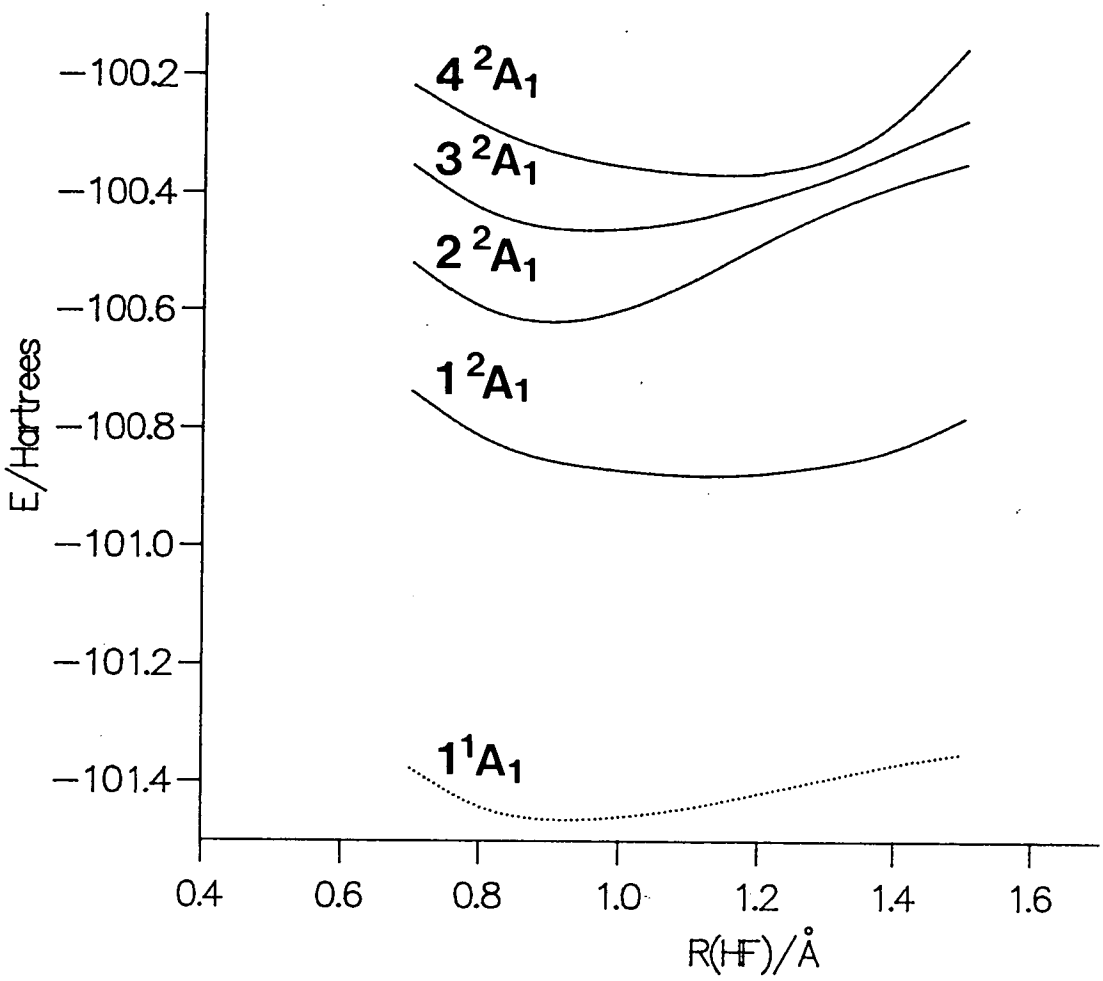

Figure 6.16. The $^2A_1$ state potential curves of $[H_3^+...F^-]$ as a function of R(HF).

State	ΔE_v (eV)	Bonding Character	R_{HF} at minimum (Å)
$1\,^2A_1$	14.55	$[H_3(\sigma^*)+HF(\sigma^*)]^{-1}$	HF=1.15
$2\,^2A_1$	21.90	$[H_3(\sigma)+HF(\sigma^*)]^{-1}$	HF=0.88
$3\,^2A_1$	25.70	50% as for $1\,^2A_1$ + 50% $F(2p_y)_v \rightarrow F(3p_y)_d+H_2(\sigma^*)_d$	HF=0.95
$4\,^2A_1$	29.24	as above	HF=1.17

Table 6.16. The bonding characteristics and vertical energies of the $^2A_1$ cationic states of $H_3^+F^-$.

The ω_e value corresponding to HF stretching alone within the the $[H_3^+F^-]^+$ (1^2A_1) cationic state is 2563.2 cm^{-1} as compared to 5238.5 cm^{-1} in neutral $H_3^+F^-$ $(1\,^2A_1)$. The lowering in the force constant of HF following ionisation of an electron from the MO shown in table 6.16 results in an increase in the HF bond length as described previously.

The $2\,^2A_1$ state correlates with an electron being removed from the MO shown in table 6.16, resulting in a decrease in the HF bond length of 0.125 Å compared to the minimum energy geometry of the $H_3^+F^-$ (1^1A_1) species. Since we are effectively creating H_3^{2+} which is very electron deficient and hence repulsive, a decrease in the HF bond length is expected.

6.6 Analysis of Basis Set Superposition Error (BSSE)

Basis set truncation in *ab initio* calculations of VDW complexes can produce errors in the total interaction energy between the monomer units. Such a phenomenon is known as BSSE and may be large or small depending on the molecular system studied and on the size of the basis set employed.

If the intermolecular distance between two monomer units X and Y of a dimer is small enough, the proximity to X of the basis functions on Y enlarges the effective basis set on X. If the finite basis on monomer X is unable to accurately describe its electronic properties then the neighbouring basis functions on Y may diminish this deficiency. The same argument also applies to the effect of the basis functions of X on those of monomer Y.

The counterpoise correction method developed by Boys and Bernardi [34] accounts for the effects of BSSE in an approximate way resulting in a first-order corrected interaction energy (a second-order corrected interaction energy would presumably require polarised monomer units, etc) given by equation 6.15,

$$E^{cc}_{XY}(G) = E_{XY}(G) - E^{cc}_{X}(G) - E^{cc}_{Y}(G) \tag{6.15}$$

where G represents the geometry of the dimer, $E_{XY}(G)$ is the total energy of the dimer and $E^{cc}_{X,Y}(G)$ are the total energies of monomers X and Y with basis functions from the other dimer present as 'ghost orbitals' with no nuclei present.

In our studies we have attempted to determine at the SCF level the extent of BSSE at a fixed geometry close to the equilibrium structure of the H_2...HF dimer for six basis sets of varying size. Although intermolecular changes following complexation are not accurately accounted for using SCF methods alone, no attempt has been made to extend this analysis to the CI level. However, *ab initio* calculations performed by Bernholdt et al. [20] on the T-shaped H_2...HF dimer around its equilibrium geometry concluded that only $\sim$1/3 of the overall well-depth arises from correlation effects and therefore our results should be of some qualitative value. The effect of a changing geometry for a fixed basis set, on the size of the counterpoise correction may be significant but has not been investigated in this work and the reader is referred to the work of Schwenke and Truhlar [35].

Table 6.17 lists the corrected and uncorrected interaction energies together with the resulting counterpoise corrections for six finite basis sets at and beyond the TZV level. With one exception, all the interaction energies are negative, indicating an attractive intermolecular potential in the region of equilibrium geometry.

As the basis set size increases, the uncorrected interaction energies remain relatively constant and are about ten times larger than the corresponding corrected energy values which in contrast gradually increase in magnitude. The resulting counterpoise correction quickly converges to a value of about 1.6×10^{-3} E_h (0.04 eV) for the largest basis sets 5 and 6.

Basis set N°	Type of Basis Set	Nuclear Centre	N° Gaussian Functions	Uncorr. Int. Energy (eV)	Corr. Int. Energy (eV)	CC (eV)
1	TZV	H and F	23	-0.085	+0.025	0.087
2	TZVP	H and F	38	-0.052	-0.060	0.046
3	TZV2P	H and F	38	-0.052	-0.098	0.043
4	diffuse s	H and F	42	-0.053	-0.106	0.043
5†	diffuse p	F only	45	-0.053	-0.109	0.042
6†	diffuse p	H and F	54	-0.055	-0.112	0.043

Table 6.17. Conterpoise corrections for six finite basis sets at and beyond the TZV level at a geometry of R1=2.136Å, HF=0.867Åand H_2=0.735Å. † indicates the basis sets used in our calculations.

The abscence of any polarisation functions on the TZV basis set (N°1) results in an anomalously large counterpoise correction which underlines the work of Schwenke and Truhlar [35] who found without exception that large BSSE results in basis sets which neglect polarisation functions. From table 6.17, the TZVP (N°2) and in particular the split polarisation basis set (N°3) clearly show a much reduced counterpoise correction. Basis sets 4, 5 and 6 all contain additional diffuse functions which in general only slightly effect the size of the counterpoise correction. However, their inclusion is essential in CI calculations in order to accurately describe the long range interactions associated with VDW molecules.

The spread in energies for the H_2 and HF monomers over the six basis sets are 0.136 and 0.816 eV respectively and the corresponding spread in the corrected and uncorrected interaction energies are 0.014 and 0.027 eV respectively, indicat-

ing that any errors in the monomer energies have been partially cancelled in the interaction energies.

In conclusion, the addition of polarisation functions to the TZV basis set results in a rapid convergence of the interaction energy and the prescence of diffuse functions as well, produce a small further improvement in E_{XY}^{CC}.

6.7 Conclusions

These preliminary calculations indicate that the potential energy surfaces of the lower Rydberg and positively charged states of the H_2...HF complex are quite unlike those of Hal_2...Rg. Vertically above the equilibrium geometry of the ground state there are large gradients with respect to H atom motion in nominally Rydberg states.

We were able to explore only a very small part of the coordinate space. Having located H_3...F^- in C_{2v} geometry, there is probably a steep downhill path to global minimum on the 1^1A_1 surface for the proton transfer state in C_{3v} symmetry. This path would correspond to out-of-plane bending of HF so that F^- can move onto the 3-fold axis above the H_3 plane. We would have also liked to explore the relative stabilities of H_2...HF^+ and H_2...FH^+ and the passage between them. The effect of symmetry breaking-modes of motion on the $^1B_1$ and $^1B_2$ 3p Rydberg states should also be quite different and lead to overlapping bending vibrational progressions in REMPI spectra.

6.8 References

1. P. Carsky and M. Urban, *Ab Initio Calculations: Methods and Applications in Chemistry.*

2a. C. Wittig, S. Sharpe and R. A. Beaudet, *Acc. Chem. Res.* **21**(1988)341.

C. Jouvet, M. Boivineau, M. C. Duval and B. Soep, *J. Phys. Chem.* **91**(1987)5416.

3. W. R. Wadt, *J. Chem. Phys.* **68**(1978)402.

4. D. C. Lorents, D. L. Huestis, M. V. McKusker, H. H. Nakano and R. M. Hill, *J. Chem. Phys.* **68**(1978)4657.

5. M. C. R. Cockett, J. G. Goode, K. P. Lawley and R. J. Donovan, *Chem. Phys. Lett.* **214**(1993)27.

6. K. Muller-Dethlefs and E. W. Schlag, *Ann. Rev. Phys. Chem.* **42**(1991)109.

7. P. W. Atkins, *Quanta: A Handbook of Concepts*, (Clarendon Press, 1974)

8. E. Schrodinger, *Collected Papers on Wave Mechanics*, Blackie and Sons, London (trans. J. F. Shearer and W. M. Deans), 1928.

9. D. R. Hartree, *The Calculation of Atomic Structures*, (Wiley, New York, 1957.)

10. D. R. Hartree, W. Hartree and B. Swirles,
Phil. Trans. Roy. Soc. (London) **A238**(1939)299.

11. C. C. J. Roothaan, *Rev. Mod. Phys.* **23**(1951)69.

12. C. C. J. Roothaan, *Rev. Mod. Phys.* **32**(1960)179.

13. M. Dupuis, D. Spangler and J. J. Wendoloski,
NRCC Program QG01 (1980).

14. H. J. Werner, *Adv. Chem. Phys.* **69**(1987)1.

15. R. Shepard, *Adv. Chem. Phys.* **69**(1987)63.

16. C. Moller and M. S. Plesset, *Phys. Rev.* **46**(1934)618.

17. K. A. Brueckner and C. A. Levinson, *Phys. Rev.* **97**(1955)1344.

18. C. C. Ballard, Thesis, Edinburgh 1993.

19. R. J. Buenker and S. D. Peyerimhoff, *Theor. Chim. Acta* **35**(1974)33.

R. J. Buenker and S. D. Peyerimhoff, *Theor. Chim. Acta* **39**(1975)217.

R. J. Buenker, *Procedings of the Workshop on Quantum Chemistry and Molecular Physics*, Wollongong, Australia (1980)

R. J. Buenker, *Studies in Physical and Theoretical Chemistry*, **21**(1982)17.

R. J. Buenker and R. A. Phillips, *J. Mol. Struc. (Theochem)* **123**(1985)291.

20. D. E. Bernholdt, S. Lui and C.E. Dykstra,
J. Chem. Phys. **85**(1986)5120.

21. L. Andrews, *Farad. Disc. Chem. Soc.* **86**(1988)1.

22. K. W. Jucks and R. E. Miller, . *J. Chem. Phys.* **87**(1987)5629.

23. R. E. Miller, P. F. Vohralik and R. O. Watts,
J. Chem. Phys. **85**(1986)3891.

24. H. Lischka, *J. Chem. Phys.* **2**(1973)191.

25. M. F. Guest, *GAMESS: User Guide and Ref. Manual* 1987.

26. C. M. Lovejoy, D. D. Nelson and D. J. Nesbitt,
J. Chem. Phys. **87**(1987)5621.

27. M. Bettendorff, R. J. Buenker, S. D. Peyerimhoff and J. Romelt,
Z. Phys. A-Atoms and Nuclei. **125**(1982)304.

28. L. J. Schaad and W. V. Hicks, *J. Chem. Phys.* **61**(1974)1934.

29. G. D. Carney and R. N. Porter, *J. Chem. Phys.* **60**(1974)4251.

30. A. E. Roche, M. M. Sutton, D. K. Bohme and H. I. Schiff,
J. Chem. Phys. **55**(1971)5480.

31. P. F. Fennelly, R. S. Hemsworth, H. I. Schiff and D. K. Bohme,
J. Chem. Phys. **59**(1973)6405.

32. H. Hotop and W. C. Lineberger, *J. Phys. Chem. Ref. Data*
14(1985)731.

33. J. Berkowitz, *Chem. Phys. Lett.* **11**(1971)21.

34. S. F. Boys and F. Bernardi, *Mol. Phys.* **19**(1970)553.

35. D. W. Schwenke and D. G. Truhlar, *J. Chem. Phys.* **82**(1985)2418.

36. S. K. Loushin, S. Liu and C. E. Dykstra, *J. Chem. Phys.* **84**(1986)2720.

Appendix A

Vibrational Numbering from Fluorescence Nodal Structure

The absolute numbering of an excited state vibronic level can be readily determined by analysing the nodal structure of dispersed fluorescence since the number of nodes in the upper vibronic state wavefunction equals the number of intensity minima observed in the dispersed fluorescence spectrum, provided the following criteria are met:

(i) A single vibronic level (of known energy) in the upper state is selectively excited.

(ii) The dispersed fluorescence from the upper vibronic level is to a region of the lower state potential energy curve which results in a spectra with low frequency modulation over several Franck-Condon (FC) envelopes, typically in a frequency domain where the Mulliken difference potential is monotonic.

(iii) Vibronic levels in the lower state are free from perturbations which may result in a loss in intensity for individual levels.

The FC principle states that the position and momenta of the diatomic nuclei remain constant during an electronic transition. The difference potential in figure A represents the locus of points where the electronic transition conserves BOTH the position and the kinetic energy of the nuclei. Therefore, emission from a diatomic molecule must land on the difference potential with a photon energy given by the difference between the initial energy of excitation minus the energy of the difference potential at the point where the transition terminates.

The intensity of a transition between two vibronic levels is proportional to $|\langle v'|\mu_{12}(R)|v\rangle|^2$, where $\mu_{12}(R)$ is the electronic transition dipole function and $\langle v'|v\rangle$ is the overlap integral between the upper and lower vibronic states, v' and v respectively. Because μ_{12} is usually a slowly varying function of R, it can be regarded as constant over the small range of R covered by the v'=2 level. Hence,

the observed fluorescence spectrum will consist of a series of peaks with spacings corresponding to the lower state vibronic levels whose intensities are governed by the FC factors. From figure 2.3 it can be seen that at the red and blue extrema of the spectrum, $\langle v'|v\rangle$ will be relatively large where the amplitude of v' and v are largest and in phase. At intermediate frequencies the magnitude of $\langle v'|v\rangle$ is much more sensitive to the relative phases of the two wavefunctions and will decrease due to the smaller amplitude of the v' wavefunction in this region.

Appendix B

Fitting of the Fluorescence Decay Data

Figure B shows a representative example of the profile of the time resolved fluorescence, $I_{fl}^{obs}(t)$, for the transition, $f'(0_g^+), v' = 0 \longrightarrow B(0_u^+)$, together with the shape of the simulated fluorescence decay, $I_{fl}^{conv}(t)$, the pulse profile, $P(t)$, and the residual, $I_{fl}^{resid}(t) = I_{fl}^{obs}(t) - I_{fl}^{conv}(t)$.

A first estimate of the lifetime was obtained by a simple fitting of the long exponential tail of the fluorescence signal beginnig at ~70 ns after the excitation pulse is over. Only a single exponential fit of the complete decay tail is required indicating a single dominant radiative channel of fluorescence to the B state. The presence of any significant non-radiative channels seems unlikely because the lower part of the f' state lies in a region of $V(R)$ and R space with few other states.

As can be seen from the $I_{fl}^{resid}(t)$ curve, the agreement between experiment and simulation is generally very good along the whole fluorescence decay tail. Some discrepancy arises at small t where the convolution of the pulse profile and the exponential decay is quite sensitive to the pulse arrival time, t_0, and the excitation profile. In an attempt to reduce $I_{fl}^{resid}(t)$ in this temporal region, simulations using different t_0 values were performed and showed that the final τ value was relatively insensitive to changes in t_0. In a further attempt to reduce $I_{fl}^{resid}(t)$ around t_0 the form of the excitation pulse was varied. A product of the experimental probe and pump pulse profiles was used in the simulation and produced little improvement in $I_{fl}^{resid}(t)$. Finally, a synthetic pulse profile in the form of a symmetric gaussian peak with a FWHM similar to the experimental pulse (~16 ns) was used in the convolution simulation and is shown in figure B. This produced a much reduced $I_{fl}^{resid}(t)$ and standard deviation and τ remained relatively unaffected.

In conclusion, by changing the profile of the excitation pulse to a more symmetric one an improvement in the convoluted fit is obtained without affecting τ significantly.

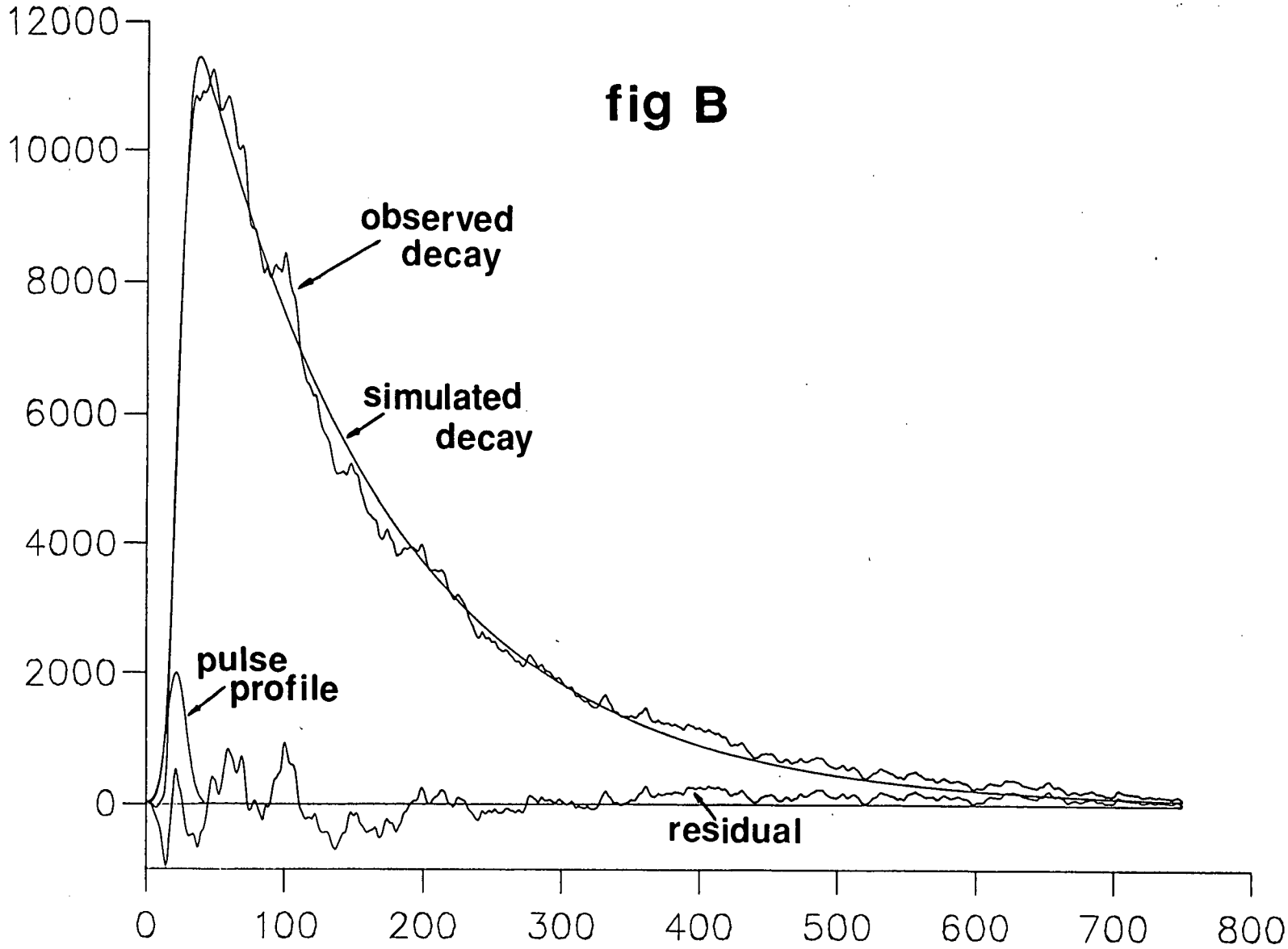
fig B
12000
10000
8000
6000
4000
2000
0
observed
decay
simulated
decay
pulse
profile
residual
0
100
200
300
400
500
600
700
800

University Regulations

Whilst pursuing postgraduate research at the Department of Chemistry here at Edinburgh I have attended the following courses:

(i) Theoretical Chemistry, Department of Chemistry.
(ii) Laser Physics, Department of Physics.
(iii) Reaction Dynamics, Department of Chemistry.
(iv) Atomic and Electron Physics, Department of Physics.

In addition I have attended the following conferences:

(i) 1^{st} Zero Kinetic Energy Photoelectron Spectroscopy Meeting, Kreuth, Germany, Oct. 1991.
(ii) 2^{nd} Northern and Scottish Universities Spectroscopy Group Meeting, University of Manchester, July 1991.
(iii) R.S.C Faraday Division, High Resolution Spectroscopy Group Meeting, Heriot-Watt University, Dec. 1991.
(iv) University of Edinburgh, Department of Chemistry Physical Discussion Evenings, 1990-1993.
(v) University of Edinburgh Laser and Molecular Beam Group Weekly Meetings, 1990-1993.

Publications

1. R. J. Donovan, T. Ridley, K. P. Lawley and P. J. Wilson, *Chem. Phys. Lett.* **196**(1992)173.

2. R. J. Donovan, T. Ridley, K. P. Lawley and P. J. Wilson, *Chem. Phys. Lett.* **205**(1993)129.

3. R. J. Donovan, T. Ridley, K. P. Lawley and P. J. Wilson, *Chem. Phys. Lett.* **207**(1993)129.

4. P. J. Wilson, T. Ridley, K. P. Lawley and R. J. Donovan, accepted by Chem. Phys.